INFORMATION TO USERS

This manuscript has been reproduced from the microfilm master. UMI films the text directly from the original or copy submitted. Thus, some thesis and dissertation copies are in typewriter face, while others may be from any type of computer printer.

The quality of this reproduction is dependent upon the quality of the copy submitted. Broken or indistinct print, colored or poor quality illustrations and photographs, print bleedthrough, substandard margins, and improper alignment can adversely affect reproduction.

In the unlikely event that the author did not send UMI a complete manuscript and there are missing pages, these will be noted. Also, if unauthorized copyright material had to be removed, a note will indicate the deletion.

Oversize materials (e.g., maps, drawings, charts) are reproduced by sectioning the original, beginning at the upper left-hand corner and continuing from left to right in equal sections with small overlaps. Each original is also photographed in one exposure and is included in reduced form at the back of the book.

Photographs included in the original manuscript have been reproduced xerographically in this copy. Higher quality 6" x 9" black and white photographic prints are available for any photographs or illustrations appearing in this copy for an additional charge. Contact UMI directly to order.

UMI

A Bell & Howell Information Company
300 North Zeeb Road, Ann Arbor MI 48106-1346 USA
313/761-4700 800/521-0600

Reconstruction Algorithms to Improve Nondestructive Evaluation of Reinforced Concrete

by

Craig M. Newtson

A dissertation submitted in partial fulfillment
of the requirements for the degree of

Doctor of Philosophy

University of Washington

1997

Approved by 
Chairperson of Supervisory Committee

Program Authorized
to Offer Degree Civil Engineering

Date 6/3/97

In presenting this dissertation in partial fulfillment of the requirements for the Doctoral degree at the University of Washington, I agree that the library shall make its copies freely available for inspection. I further agree that extensive copying of this dissertation is allowable only for scholarly purposes, consistent with "fair use" as prescribed in the U.S. Copyright law. Requests for copying or reproduction of this thesis may be referred to University Microfilms, 1490 Eisenhower Place, P.O. Box 975, Ann Arbor, MI 48106, to whom the author has granted "the right to reproduce and sell (a) copies of the manuscript in microform and/or (b) printed copies of the manuscript made from microform."

Signature 

Date 6/3/97

University of Washington

Abstract

Algorithms to Improve Nondestructive Evaluation of Reinforced Concrete

by Craig M. Newtson

Chairperson of the Supervisory Committee: Professor Marc O. Eberhard
Department of Civil Engineering

Two reconstruction algorithms have been developed to improve nondestructive evaluation of reinforced concrete structures. Both algorithms implement computationally demanding strategies to estimate the properties of potentially complex systems. These algorithms are: 1) a two-dimensional magnetic algorithm to identify the locations and sizes of reinforcing bars in concrete, and 2) an algorithm to estimate the material properties and geometry of a concrete member by comparing the experimental and simulated dynamic responses to a surface impact.

The magnetic algorithm uses magnetostatic relationships to relate measured distortions in the magnetic field outside a concrete member to the distribution of steel within the member. An optimal solution for the locations and sizes of the reinforcing bars is determined by minimizing the difference between measured and computed distortions in the magnetic field. In simulated problems, where the concrete was assigned the magnetic properties of air, the algorithm accurately identified the location and size of a single bar, even in the presence of induced random errors. The algorithm was also able to identify two bars simultaneously, even when they were closely spaced. When realistic magnetic properties were used for modeling the concrete, it was found that the concrete had a significant effect on the measured magnetic distortions. A convenient method was found to compensate for the magnetic distortion caused by the concrete.

The dynamic response algorithm consists of the following steps: 1) recording an impact and the dynamic response of a concrete member at multiple locations, 2)

comparing these responses with those obtained by simulating the experiment with a finite-difference model, and 3) varying the properties of the model until the difference between the measured and simulated responses is minimized. Applying the algorithm to experimental measurements of dynamic response demonstrated the algorithm's ability to identify the thickness and Young's modulus of a slab. When applied to simulated responses of a slab containing a partial depth, open, surface crack, the algorithm also demonstrated the potential to estimate crack depth and location.

TABLE OF CONTENTS

LIST OF FIGURES

LIST OF TABLES

ACKNOWLEDGMENTS

The author would like to express his sincere gratitude to Professor Marc Eberhard for his guidance throughout the course of this work and for his assistance in preparing this manuscript. Thanks also to Professors Donald Janssen, Paul Johnson, and George Turkiyyah for their invaluable contributions and suggestions.

The author is also grateful to the many people who contributed their time and effort to a multitude of tasks, including: Mr. Tom Alford, Dr. Stanley Boyle, Mr. Richard Breitenbach, Mr. William Davids, Ms. Geneviève Pla-Rucki, Mr. Thomas Price, Mr. Stanley Ryter, Ms. Bonnie Savage, and Ms. Darcy van Patten.

Finally, the research presented in this dissertation was funded by National Science Foundation grant MSS-9158152 and by the University of Washington Thomas and Marilyn Nielsen Endowed Fund in Engineering. Their financial support is greatly appreciated.

To Kathy and Cortney.

Chapter 1

INTRODUCTION

Actual properties of a reinforced concrete structure often differ from its nominal design properties. Irregularities at the batch plant, such as improper proportioning of a mixture, may result in placement of concrete with unacceptable performance. Improper placement of reinforcing steel can significantly change the structural strength of a member. Poor consolidation during placement can cause voids in a member, reducing its load carrying capacity and stiffness. Inadequate curing conditions after placement can also severely reduce the strength and stiffness of a structure. Finally, during the life of a structure the concrete may deteriorate due to environmental conditions, or the structure may be damaged by acts of man or nature.

It is important to evaluate suspect structures in a manner that does not cause further distress. Numerous nondestructive evaluation techniques have been developed to ensure the integrity of structures during testing. These techniques take advantage of a variety of physical phenomena and solve inverse problems to determine characteristics of the structure. Traditionally, inverse problems applied to nondestructive test methods have been based on simple physical or material models to reduce computational costs. However, emerging computational technologies now provide the ability to investigate the

feasibility of implementing inverse problems that are less simplified and more computationally intense. Two areas of nondestructive evaluation that could benefit from these types of inverse problems are detection of reinforcing steel in concrete and characterization of material properties and structural geometry using stress wave propagation methods.

Current practice to determine the geometry of the reinforcing steel is to use induction meters, which rely on the magnetic properties of the steel. Induction meters provide acceptable results when the reinforcement configuration is simple. However, nondestructive evaluation with induction meters is less reliable when the geometry of the reinforcement is complicated by the presence of closely spaced bars, stirrups, and ties (Lauer 1991).

Voids in concrete and stiffness of the concrete are usually evaluated with stress wave propagation methods, such as impact-echo (Sansalone and Carino 1991) or spectral-analysis-of-surface-waves (SASW). Impact-echo testing is an excellent method for detecting delaminations in situations where the thickness of the concrete member is known, but will not simultaneously determine Young's modulus of the concrete. SASW can provide a profile of concrete stiffness through the depth of the member (Kalinski et al 1994). However, SASW assumes a layered system wherein the layers have uniform thickness and extend to infinity. This assumption limits the applicability of SASW in identifying cracks and voids.

Voids may also be identified with thermography (Weil 1991). Thermographic measurements are useful when investigating a large area of a structure. However, thermography does not detect the flaw depth, and results require subjective interpretation by persons with extensive experience.

OBJECTIVES

The ability to evaluate civil engineering structures would significantly improve if nondestructive test methods were available to: 1) decipher complex reinforcement configurations, and 2) simultaneously determine the stiffnesses and configuration of constituents in a geometrically complex system. As a step toward this goal, this work presents algorithms for two nondestructive testing methods that will provide greater versatility than existing tests.

The first objective was to develop a two-dimensional, magnetostatic technique to determine the locations and sizes of reinforcing bars. To implement this technique, a magnetic field ($\mathbf{B_o}$) is applied to a reinforced concrete member, and the distortion of the field ($\mathbf{B''}$), caused by the steel within the member, is measured in several locations. A possible configuration is shown schematically in Figure 1.1. The algorithm computes the reinforcement configuration whose corresponding magnetic distortion most resembles the measured distortion. This method improves on existing methods by providing the ability to detect multiple bars and identification of the bar size at greater depths.

The second objective was to develop a dynamic response method to estimate the engineering properties for geometrically complex systems by comparing experimental and simulated responses to a surface impact. The experimental setup is similar to that used for SASW testing. The algorithm estimates the engineering properties of the system being evaluated by producing a simulation model with the most similar dynamic response. This method is an improvement from the existing SASW test because more complex geometries can be investigated. Because the constructed model can simulate a complex physical system, geometric irregularities such as slab edges, cracks, and voids can be investigated.

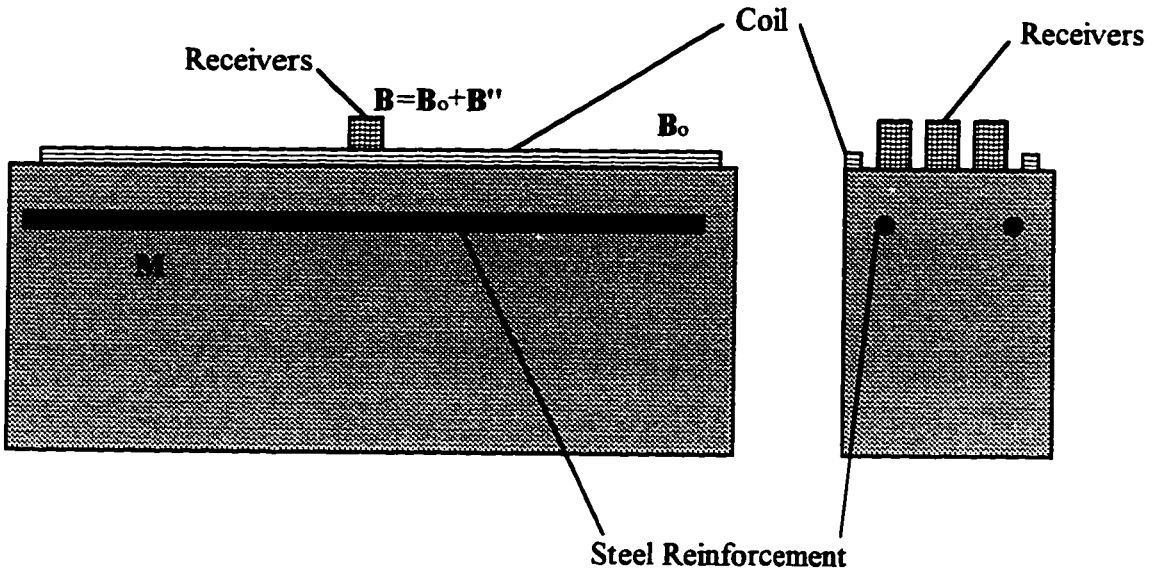

Figure 1.1. Magnetic detection technique.

ORGANIZATION

A review of previous work in the area of electromagnetic detection of reinforcing steel is provided in Chapter 2. Chapter 3 presents previous work on wave propagation methods, as well as a review of a method other investigators have used to model the propagation of stress waves in solids.

An overview of the proposed magnetic detection algorithm and derivations of the two-dimensional relationships that support the algorithm are presented in Chapter 4. In Chapter 5, the magnetic detection algorithm is applied to simulated problems containing up to two reinforcing bars. The simulated problems demonstrate the algorithm's ability to identify the location and size of single or multiple bars, and the algorithm's sensitivity to measurement errors. The influence of the magnetic properties of the concrete and a comparison of various compensation methods are discussed in Chapter 6.

Chapter 7 provides an overview of the dynamic response test method and the development of the finite-difference scheme used to model the dynamic response of a system. A parametric study of the material and geometric properties used in the dynamic response model is presented in Chapter 8. In Chapter 9, the algorithm is applied to experimental results for simple geometries and to simulated results for geometries containing surface cracks. The experimental problems demonstrate the algorithm's ability to identify the depth and Young's modulus of a concrete slab. The simulated problems demonstrate the algorithm's potential for deciphering complex geometries.

A summary of the completed work and recommendations for further research are presented in Chapter 10.

Chapter 2

REVIEW OF ELECTROMAGNETIC METHODS

This chapter reviews the work of other investigators in the area of electromagnetic detection of reinforcing steel. The state of the practice is described and recent research advances are reviewed.

CURRENT PRACTICE

Currently, the geometry of the reinforcement is most often determined with induction meters, which rely on the electromagnetic properties of the steel (Malhotra and Carino 1991). The induction meter is rotated and moved sideways until a maximum reading is achieved. It is then known that the bar is directly under the induction and lies in the direction of the meter. The magnitude of the maximum reading can then be used with correlation data to determine the cover depth of the bar (Popovics and Popovics 1991). No information regarding the size of the bar is obtained from a single reading.

Popovics and Popovics (1991) proposed that the bar size be identified from the variation of the induction field above the bar. They suggested taking readings with the induction meter at spacings of 12.7 mm ranging 76.6 mm on each side of the bar. This

suggestion was implemented experimentally, and the curves obtained showed that it was possible to distinguish between 12.7 mm diameter bars and 19.1 mm bars at the same depth. This method is a significant improvement over existing methods because it determines the bar size. However, many measurements must be recorded to determine the size of the bar, only a single bar may be identified from a series of tests, and the method is cumbersome to implement.

More recently, Hilti Corp. (1994) has developed an instrument that employs an induction meter with multiple sensors. This equipment investigates a 0.76 m square area. Results are provided in the form of a map of the reinforcing steel in the area under investigation. Bars are detected to a depth of 180 mm, but bar size is identified only for bars with depths less than 64 mm. A depth of 64 mm barely exceeds cover requirements in exposed conditions (Building 1995).

THREE-DIMENSIONAL MAGNETOSTATIC ALGORITHM

A more rigorous method of locating ferromagnetic materials, based on fundamental magnetostatic relationships, was proposed by Pla, Eberhard, and Eberhard (1994). The proposed method consisted of:

1) Magnetization of the region under investigation with a driving field, $\mathbf{B}_o$, as shown in Figure 2.1. A coil with known properties and known current is used to generate this field.

2) Measurement of the total magnetic field, $\mathbf{B}$, which is the sum of the driving field, $\mathbf{B}_o$, and the field due to the magnetization of the steel within the member, $\mathbf{B}''$. The method requires that all three vector components of $\mathbf{B}$ be measured.

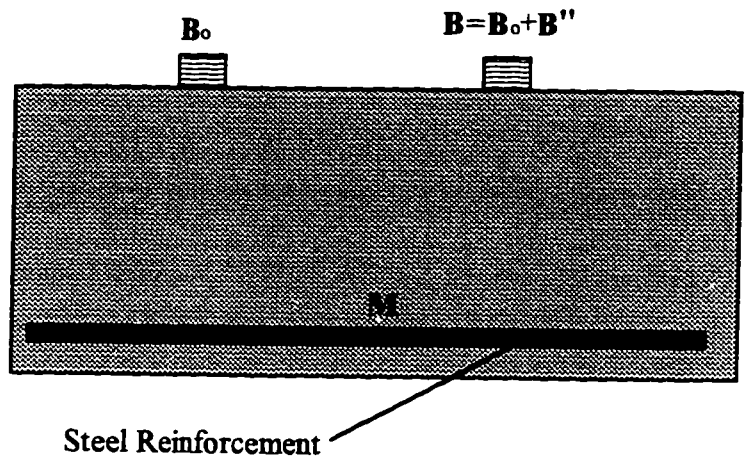

Figure 2.1. Magnetic detection principle (Pla, Eberhard, and Eberhard 1994).

3) Determining the distortion in the magnetic field caused by steel within the member, **B"**. This distortion is determined by subtracting the driving field, $\mathbf{B}_o$, from the total magnetic field, **B**.

4) Calculation of the magnetic dipole moment inside the member. The member under investigation is discretized into j cubes of volume dv_j. The magnetic distortion (**B"**), measured at i receivers, is used to calculate the magnetic dipole moment, **M**dv. The distortion at the receivers, caused by magnetization of a volume, is shown in Figure 2.2. This calculation is performed by inverting the magnetic dipole formula:

$$\mathbf{B}_i'' = \sum_j \frac{\mu_o}{4\pi R_{ji}^3}\left[3\left(\mathbf{M}_j dv_j \cdot \frac{\mathbf{R}_{ji}}{R_{ji}}\right)\frac{\mathbf{R}_{ji}}{R_{ji}} - \mathbf{M}_j dv_j\right] \qquad (2.1)$$

where μ_o is the magnetic permeability of free space, $4\pi 10^{-7}$ N/A^2, and $\mathbf{R}_{ji}$ is the vector from cube j to receiver i. To invert this system of equations, it is necessary to measure $\mathbf{B}_i''$ in at least as many locations as there are possible locations of steel.

5) Calculation of the ambient magnetic field inside the member. The ambient magnetic field, $\mathbf{B}_{ext}$, at cube j is the sum of the driving field ($\mathbf{B}_o$) at the center of the cube and the field due to the magnetization of the other i cubes, $\mathbf{B}_j''$:

$$\mathbf{B}_j'' = \sum_i \frac{\mu_o}{4\pi R_{ij}^3}\left[3\left(\mathbf{M}_i dv_i \cdot \frac{\mathbf{R}_{ij}}{R_{ij}}\right)\frac{\mathbf{R}_{ij}}{R_{ij}} - \mathbf{M}_i dv_i\right] \qquad (2.2)$$

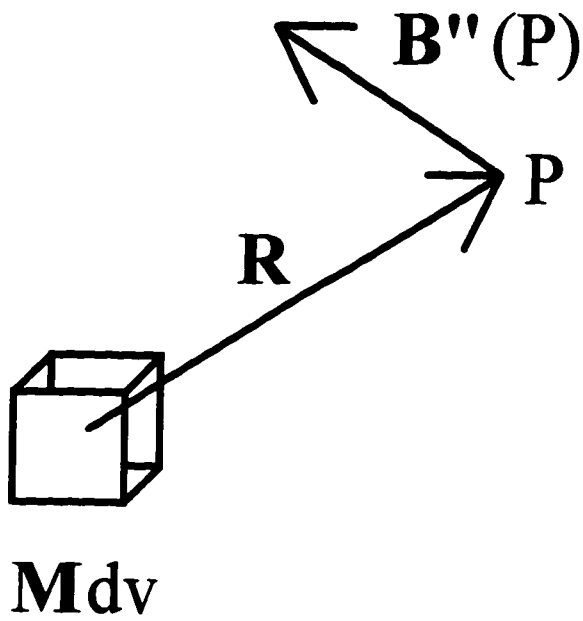

Figure 2.2. Magnetic distortion, **B''**, at a point, P, caused by magnetization of a volume, dv.

6) Calculation of the volume of steel in each cube. This calculation is accomplished with the following equation, which relates the magnetic dipole density, **M**, to the ambient magnetic field ($\mathbf{B}_{ext}$):

$$dv_{x\,steel} = \frac{\mu_o (1+.333\chi_m) M_x dv}{\chi_m B_{x,ext}} \tag{2.3}$$

where dv_x is the volume of steel in the cube and χ_m is the magnetic susceptibility of steel, approximately 2000. Similar equations may be written for the y- and z-vector components. Volumes of steel close to the volume of the cube indicate the presence of steel and volumes close to zero indicate the absence of steel.

This algorithm was implemented on simulated problems with simple geometries. Measurements of the driving field and magnetic distortion were simulated with finite element analyses. Pla, et al. (1994) found that the algorithm was able to identify the location of cubes filled with steel when the possible locations of the cubes were widely spaced. The algorithm was less successful when the possible locations of the cubes were adjacent to each other. Difficulties in solving the more complex problems was attributed to the inability to simulate the small distortions generated by small amounts of steel.

The algorithm proposed by Pla, et al. (1994) is attractive because the volume of steel in each volume element is determined by solving a set of linear equations. However, a disadvantage is that the distortion in the magnetic field must be measured in a number of locations at least equal to the number of volume elements. The number of measurements needed could become prohibitive when solving a problem with refined discretization.

SUMMARY

Current methods to identify reinforcing bars in concrete are unable to identify the size of a bar at depths significantly greater than required cover depths. An alternative to existing methods is to use fundamental magnetic relationships to determine the locations of bars and the quantity of steel present at each location. A drawback to the algorithm proposed by Pla et al (1994) is that the number of measurements needed to investigate an area with adequate refinement would be prohibitive. A new method that utilizes the fundamental magnetic relationships with a limited number of measurements would significantly improve the ability to identify reinforcing bars.

Chapter 3

REVIEW OF STRESS WAVE PROPAGATION METHODS

Impact-echo and spectral-analysis-of-surface-waves (SASW), two stress wave propagation methods used in practice, are reviewed in this chapter. Following the discussion of these methods, the chapter reviews finite-difference modeling of stress wave propagation.

SURFACE WAVE PROPAGATION METHODS

Surface waves were first identified by Lord Rayleigh in 1887. Since then, the terms surface wave and Rayleigh wave have been used interchangeably, although another type of surface wave, called a Love wave, was identified in 1911.

A theoretical treatment of Rayleigh waves was developed for a two-dimensional geometry by Lamb (1904). Building on the work conducted by Rayleigh and Lamb, numerous investigators have contributed to developing surface wave testing. By the 1960's, surface wave testing was routinely used to determine soil properties in situ.

Early applications of surface wave testing of concrete were performed on concrete pavement systems (Nazarian et al 1983, Nazarian 1984). The test method used in these

studies consisted of propagating a wave that contains a broad band of frequencies across two receivers. Propagation of the surface wave was initiated by generating an impact at the pavement surface with a hammer or with a transducer, depending on the test geometry. Geophones were used as receivers. An example of the test geometry is shown in Figure 3.1. Tests were conducted with receiver spacings (L) of 0.15 m, 0.3 m, 0.6 m, 1.2 m, and 2.4 m to investigate the full depth of the pavement system.

Analysis of the data required that the time histories be converted to the frequency domain using the Fourier transform:

$$S_1(f) = \int_{-\infty}^{\infty} x(t)\exp(-i2\pi nt)\,dt \tag{3.1}$$

where $S_1(f)$ is the frequency domain representation of x(t), which is the response history of receiver 1. The cross-power spectrum was then calculated with the following equation:

$$G_{12}(f) = S_2(f) \cdot S_1^*(f) \tag{3.2}$$

where $S_1^*(f)$ is the complex conjugate of $S_1(f)$ and $S_2(f)$ is the frequency representation of the response history from receiver 2. The real and imaginary components of the cross-power spectrum were then used to determine the phase representation of the cross-power spectrum:

$$\phi(f) = \tan^{-1}\left(\frac{G_{imag}(f)}{G_{real}(f)}\right) \tag{3.3}$$

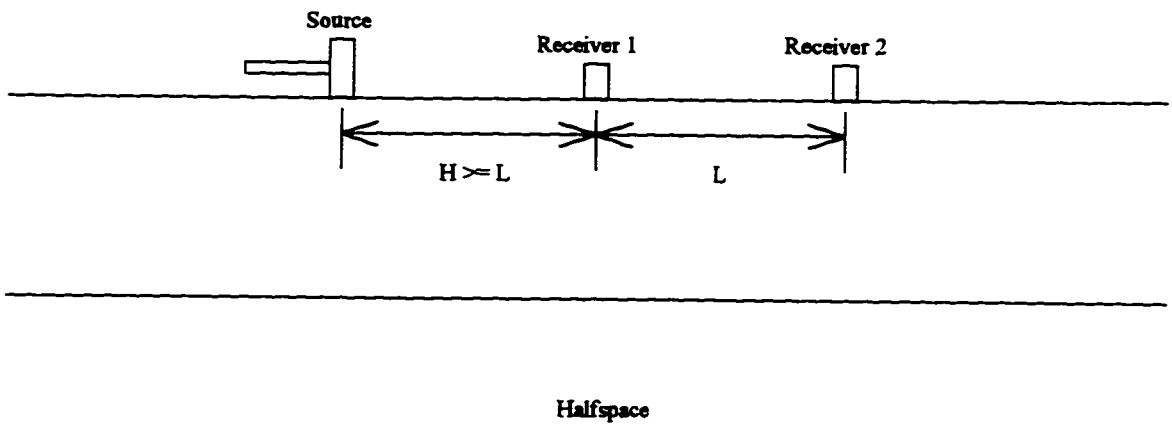

Figure 3.1. SASW test configuration.

This phase is the relative shift of each frequency contained in the wave between the two receivers. Unwrapping the phase representation of the cross-power spectrum so that the values are not bounded by $-\pi$ and π results in phase values that represent the phase shift between the two receivers. The "unwrapped" phase values include shifts that exceed the wavelength associated with a given frequency.

Velocity values, v_{ph}, for each frequency component of the surface wave were then calculated with the following relationship:

$$v(f) = \frac{360Lf}{\phi(f)} \tag{3.4}$$

where L was the distance between the receivers. The wavelength associated with each of the frequencies was calculated with the following equation:

$$\lambda = \frac{v(f)}{f} \tag{3.5}$$

Nazarian (1984) presented the data in two forms. For a simplified analysis, a dispersion curve was obtained by plotting the calculated velocities against the wavelengths. Wavelengths can be converted to approximate depth by multiplying them by a constant. A more complex analysis provides a plot of Young's modulus versus depth. Young's modulus values were obtained by comparing the dispersion curve to a theoretical dispersion curve calculated for an assumed geometry. The method used to calculate this theoretical dispersion curve is a matrix method derived by Thomson (1950) and Haskell (1953). The reader is referred to Nazarian (1984) for a detailed discussion of the method.

However, it is important to discuss the underlying assumptions used by Haskell and Thomson.

Theoretical dispersion curves obtained by the Haskell-Thomson method are calculated assuming that the tested geometry can be represented with continuous elastic layers of uniform thickness overlying an elastic halfspace. It is also assumed that displacements are continuous at the interface between layers. These assumptions limit the areas that can be tested to areas near the middle of a concrete slab where the assumption that the layers extend to infinity is reasonable. The assumptions also indicate that the method is insensitive to nonuniform layer thicknesses. Consequently, if a system has layers with nonuniform thicknesses, the resulting Young's modulus values will be representative of a system with layer thicknesses approximately equal to the average thicknesses of the layers in the physical system. The assumption that the layers are continuous further restricts the geometries that can be investigated. Geometries that contain voids or other discontinuities cannot be modeled accurately with the Haskell-Thomson method.

Nazarian (1984), found that the SASW method was able to accurately determine the stiffness of the pavement slab and the stiffnesses of the deeper layers. However the method was unable to determine the stiffness of the region immediately below the slab.

Kalinski et al (1994) used the SASW method to detect damaged regions of a reinforced concrete bridge girder. The SASW results identified regions of the girder that had been damaged by vehicular impact while the girder was in service. Damaged regions of the girder were identified qualitatively by comparing dispersion curves from damaged and undamaged sections of the girder. Geometric features of the cracks in the damaged regions and material properties of the damaged and undamaged concrete were not quantified by Kalinski et al (1994).

Previous researchers have attempted to identify voids in soil profiles by comparing surface wave propagation in the time domain. Nogueira (1986) used finite element models to establish that internal cavities have no appreciable effect on the time of first arrival of surface waves. However, he also found that the response changed dramatically when a void was included in the model. Imran et al (1995), attempted to model experimental responses to an impact recorded during testing of a soil specimen with a surface crack. The study found that the experimental time histories were difficult to simulate. However, it was concluded that the potential to use the recorded response to detect and size the crack did exist.

When used in conjunction with the Haskell-Thomson method, the SASW method accurately determines the stiffnesses and thicknesses of the layers in the system. When used without the Haskell-Thomson method, SASW yields only qualitative results since exact depths and stiffnesses are not provided. A distinct disadvantage to the SASW method is that it is limited to investigation of simple physical geometries. It is not appropriate for testing near the edges of slabs where microstructural deterioration due to freezing and thawing is expected to occur. Other investigators have not had success using the time domain response to impact to determine the locations and geometries of cracks and voids in solids. However, time domain analysis of surface waves has been identified as having the potential to identify the locations and geometries of cracks and voids.

IMPACT-ECHO TEST METHOD

The impact-echo technique is based on the propagation of compression waves. An impact is applied to the surface of the test specimen. Then, the opposite face of the specimen or flaws within the specimen reflect body waves back to a transducer near the

impact source (Sansalone and Carino 1991). The principle for impact-echo testing is illustrated in Figure 3.2.

The response history recorded at the transducer is converted to the frequency domain with the fast Fourier transform technique. A peak in the amplitude spectrum corresponds to the frequency at which the wavefront of the compression wave travels back and forth between the two reflective surfaces. The depth of the unseen reflecting surface, T, is determined with the following equation (Sansalone and Carino 1991):

$$T = \frac{v_p}{2f} \tag{3.6}$$

where v_p is the velocity of the compression wave (Equation 3.13) and f is the frequency at which the wavefront travels back and forth between the reflective surfaces.

The velocity of the compression wave can be determined before the test by one of the following methods:

1) Measurement on a laboratory specimen (Sansalone and Carino 1989).

2) Direct measurement at a location on the test specimen where the thickness is known (Sansalone and Carino 1989a).

3) Measuring the velocity of the surface wave with two receivers and calculating v_p. The relationships required to perform this calculation are available in the documentation provided with the commercially available impact-echo testing equipment.

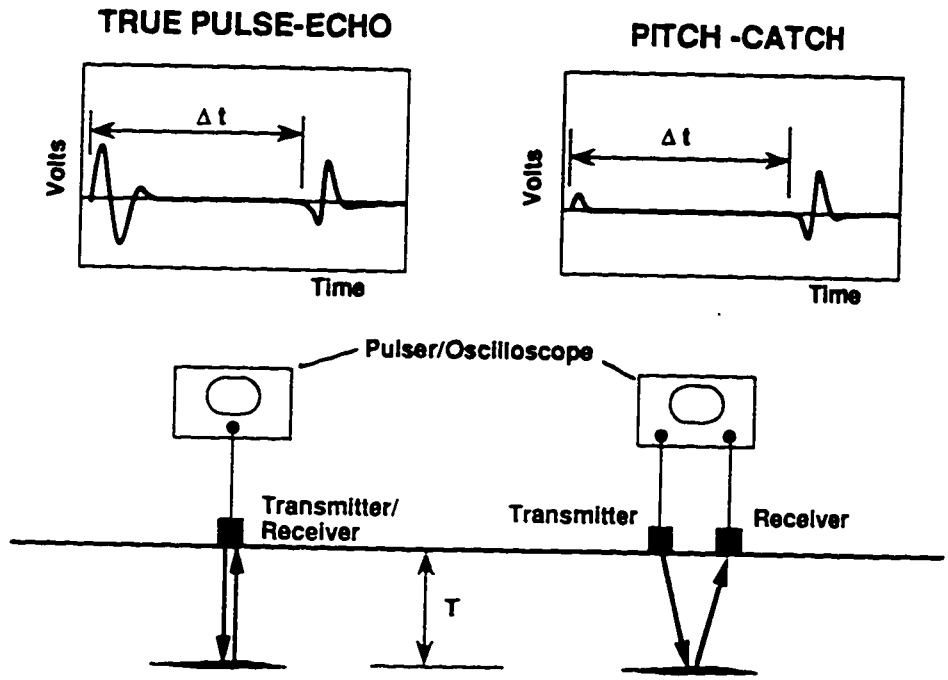

Figure 3.2. Principle of the impact-echo test method (Sansalone and Carino 1991).

4) Measurement of the compression wave speed at the surface with two receivers. The velocity of the compression wave in the body of the specimen is calculated as follows (Lin and Sansalone 1995):

$$v_p = 0.96 v_{p,surface} \tag{3.7}$$

The impact-echo technique was first developed in the early 1970's (Sansalone and Carino 1991). Initially, the technique was used to evaluate concrete piles. More recently, impact-echo has been used successfully to detect voids (Carino et al 1986, and Sansalone and Carino 1989), delaminations (Sansalone and Carino 1989), and honeycombing (Sansalone and Carino 1988). Efforts have also been made to generalize the method so that a greater variety of specimen shapes can be investigated (Sansalone and Carino 1987, Lin and Sansalone 1992, Lin and Sansalone 1992a, and Lin and Sansalone 1993).

Impact-echo testing has demonstrated an excellent ability to detect abrupt changes in stiffness, such as flaws or edges of concrete members. However, the method has several drawbacks. The greatest of these drawbacks is that information is only obtained for a point on the surface of member being investigated. Large areas must be investigated by conducting multiple tests. Depending on the number of tests conducted, an investigation may become labor intensive. Another drawback is that no information is obtained regarding material beyond the first major void or the opposite face of the member.

FINITE-DIFFERENCE MODELING OF STRESS WAVE PROPAGATION

Alterman and Karal (1968), developed a two-dimensional finite-difference scheme to model the propagation of stress waves in geophysical applications. The finite-

difference model they developed was based on discretization of the equations of motion for a homogeneous, isotropic, elastic medium:

$$(\lambda+2G)\nabla(\nabla\cdot\mathbf{u})-G(\nabla\times\nabla\times\mathbf{u})=\rho\frac{\partial^2\mathbf{u}}{\partial t^2} \tag{3.8}$$

where λ and G are the Lame constants, **u** is the vector displacement, ρ is density, and t is time.

Expanding these equations in cylindrical coordinates, one obtains:

$$\left[\frac{\partial^2 u}{\partial r^2}+\frac{1}{r}\frac{\partial u}{\partial r}-\frac{1}{r^2}u+\frac{\partial^2 v}{\partial r\partial z}\right]+\left(\frac{v_s}{v_p}\right)^2\left[\frac{\partial^2 u}{\partial z^2}-\frac{\partial^2 v}{\partial r\partial z}\right]=\frac{1}{v_p}\frac{\partial^2 u}{\partial t^2} \tag{3.9}$$

and

$$\left[\frac{\partial^2 v}{\partial z^2}+\frac{1}{r}\frac{\partial u}{\partial z}+\frac{\partial^2 u}{\partial r\partial z}\right]+\left(\frac{v_s}{v_p}\right)^2\left[\frac{\partial^2 v}{\partial r^2}-\frac{\partial^2 u}{\partial r\partial z}-\frac{1}{r}\frac{\partial u}{\partial z}+\frac{1}{r}\frac{\partial v}{\partial r}\right]=\frac{1}{v_p}\frac{\partial^2 v}{\partial t^2} \tag{3.10}$$

where u and v are the components of the displacement vector **u**.

Discretization of Equations 3.9 and 3.10 yields the following equations, which can be used to solve for displacements, u and v at location ($m\Delta r$, $n\Delta z$) and time step $l+1$:

$$
\begin{aligned}
&u(m,n,l+1) = 2u(m,n,l) - u(m,n,l-1) \\
&+\left(\frac{v_p \Delta t}{\Delta r}\right)^2 \left[u(m+1,n,l) - 2u(m,n,l) + u(m-1,n,l)\right] \\
&+\frac{1}{2}\left(\frac{v_p \Delta t}{\Delta r}\right)^2 \frac{1}{m}\left[u(m+1,n,l) - u(m-1,n,l)\right] - \left(\frac{v_p \Delta t}{m \Delta r}\right)^2 u(m,n,l) \\
&+\frac{1}{4}\left(\frac{v_p \Delta t}{\Delta r}\right)^2 \left(\frac{\Delta r}{\Delta z}\right)\left[1 - \left(\frac{v_s}{v_p}\right)^2\right]\left[v(m+1,n+1,l) - v(m+1,n-1,l)\right] \\
&+\frac{1}{4}\left(\frac{v_p \Delta t}{\Delta r}\right)^2 \left(\frac{\Delta r}{\Delta z}\right)\left[1 - \left(\frac{v_s}{v_p}\right)^2\right]\left[v(m-1,n-1,l) - v(m-1,n+1,l)\right] \\
&+\left(\frac{v_s \Delta t}{\Delta z}\right)^2 \left[u(m,n+1,l) - 2u(m,n,l) + u(m,n-1,l)\right]
\end{aligned}
\tag{3.11}
$$

and

$$
\begin{aligned}
&v(m,n,l+1) = 2v(m,n,l) - v(m,n,l-1) \\
&+\left(\frac{v_p \Delta t}{\Delta z}\right)^2 \left[v(m,n+1,l) - 2v(m,n,l) + v(m,n-1,l)\right] \\
&+\frac{1}{2}\left(\frac{v_p \Delta t}{\Delta r}\right)^2 \left(\frac{\Delta r}{\Delta z}\right)\left[1 - \left(\frac{v_s}{v_p}\right)^2\right]\frac{1}{m}\left[u(m,n+1,l) - u(m,n-1,l)\right] \\
&+\frac{1}{4}\left(\frac{v_p \Delta t}{\Delta r}\right)^2 \left(\frac{\Delta r}{\Delta z}\right)\left[1 - \left(\frac{v_s}{v_p}\right)^2\right]\left[u(m+1,n+1,l) - u(m+1,n-1,l)\right] \\
&+\frac{1}{4}\left(\frac{v_p \Delta t}{\Delta r}\right)^2 \left(\frac{\Delta r}{\Delta z}\right)\left[1 - \left(\frac{v_s}{v_p}\right)^2\right]\left[u(m-1,n-1,l) - u(m-1,n+1,l)\right] \\
&+\frac{1}{2}\left(\frac{v_s \Delta t}{\Delta r}\right)^2 \frac{1}{m}\left[v(m+1,n,l) - v(m-1,n,l)\right]
\end{aligned}
\tag{3.12}
$$

This calculation is performed with known displacements from previous time steps at the grid point being evaluated and the eight adjacent grid points. A stencil representation of this calculation is shown in Figure 3.3. The velocity terms, v_p and v_s, represent the velocities of the pressure and shear waves, respectively. The velocity of the pressure wave may be calculated as follows:

$$v_p = \sqrt{\frac{\lambda + 2G}{\rho}} \tag{3.13}$$

and the shear wave velocity may be calculated as follows:

$$v_s = \sqrt{\frac{G}{\rho}} \tag{3.14}$$

For the algorithm to be numerically stable, the time increment, Δt, must be small enough to capture the effects of the propagating waves. Alterman and Lowenthal (1970) showed that the finite-difference formulation is stable if the following relationship is satisfied:

$$\Delta t \leq \frac{h}{\sqrt{v_p^2 + v_s^2}} \tag{3.15}$$

where h is the grid spacing.

The geometry of the problems solved by Alterman and Karal (1968) is shown in Figure 3.4. From the symmetry conditions, it was known that the horizontal displacement

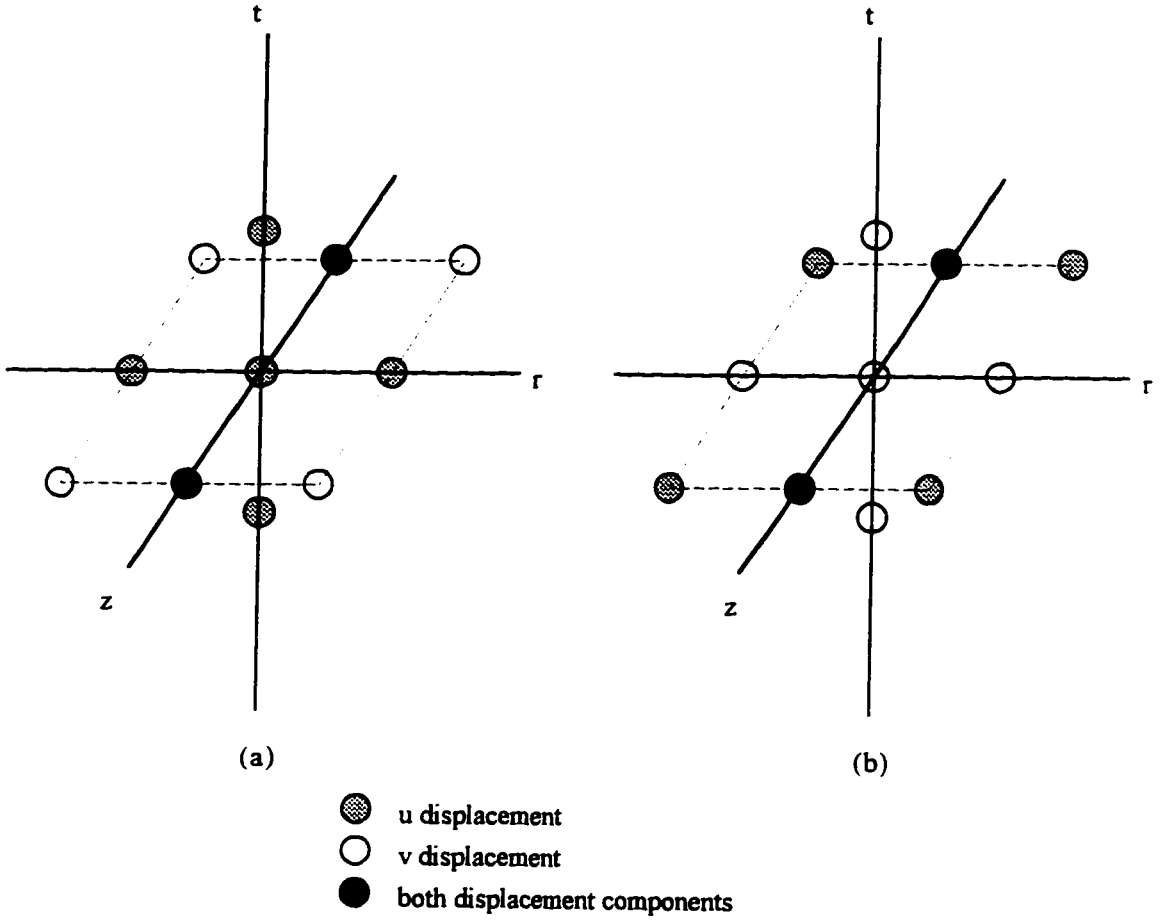

Figure 3.3. Calculation stencils for the displacement components. Diagram (a) shows the grid points used in calculating u, and diagram (b) shows the grid points used in calculating v.

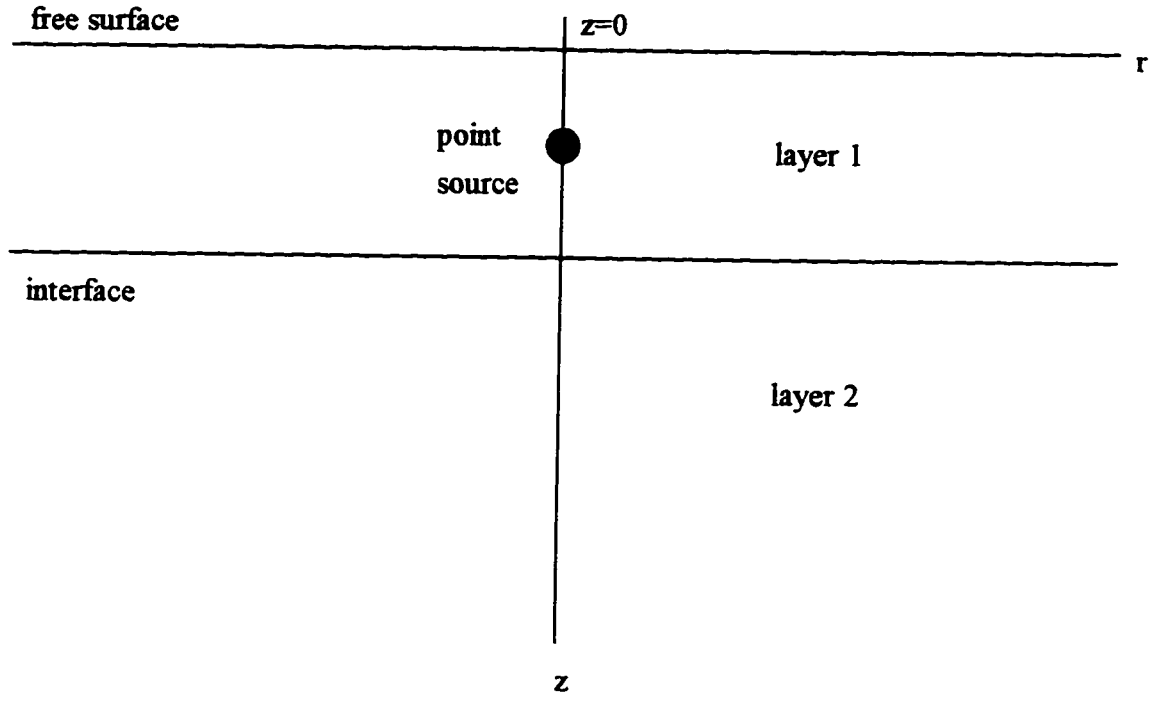

Figure 3.4. Problem geometry for finite difference simulations by Alterman and Karal (1968).

at all points on the centerline was zero. Symmetry conditions were also used to reduce the number of terms in Equation 3.12.

Boundary conditions were imposed at the free surface and at the interface between layers. At the free surface, σ_z and τ_{rz} are equal to zero. These conditions were enforced by adding a row of imaginary grid points outside the body, as shown in Figure 3.5. Displacements at these points were calculated by expressing the constitutive law with displacements. Along the interface, displacements at the surface of layer 2 are equal to the displacements at the bottom of layer 1. The displacements along the imaginary line were determined by imposing the condition that σ_z and τ_{rz} are continuous at the interface.

Alterman and Karal (1968) concluded that the algorithm yielded accurate and reliable results when an interior compressional point source was used for excitation. Kelly et al (1976) produced a similar model based on discretization of the equations of motion in two-dimensional rectangular coordinates. They also obtained accurate and reliable results.

SUMMARY

This chapter reviewed the SASW and impact-echo test methods. SASW is an excellent method for obtaining stiffness profiles when it is applied to simple geometries. However, it provides only a qualitative measure in applications where cracks or voids are being investigated. Impact-echo testing is good for detecting flaws in concrete but provides no information about material beyond the first flaw or surface. Utilizing all the information in response histories recorded at the surface would provide more information about the test area than is obtainable with either SASW or impact-echo. The information used by both existing methods could be used simultaneously in an improved method.

A finite-difference method that other investigators have used to model stress wave propagation was also reviewed. According to those investigators, the finite-difference

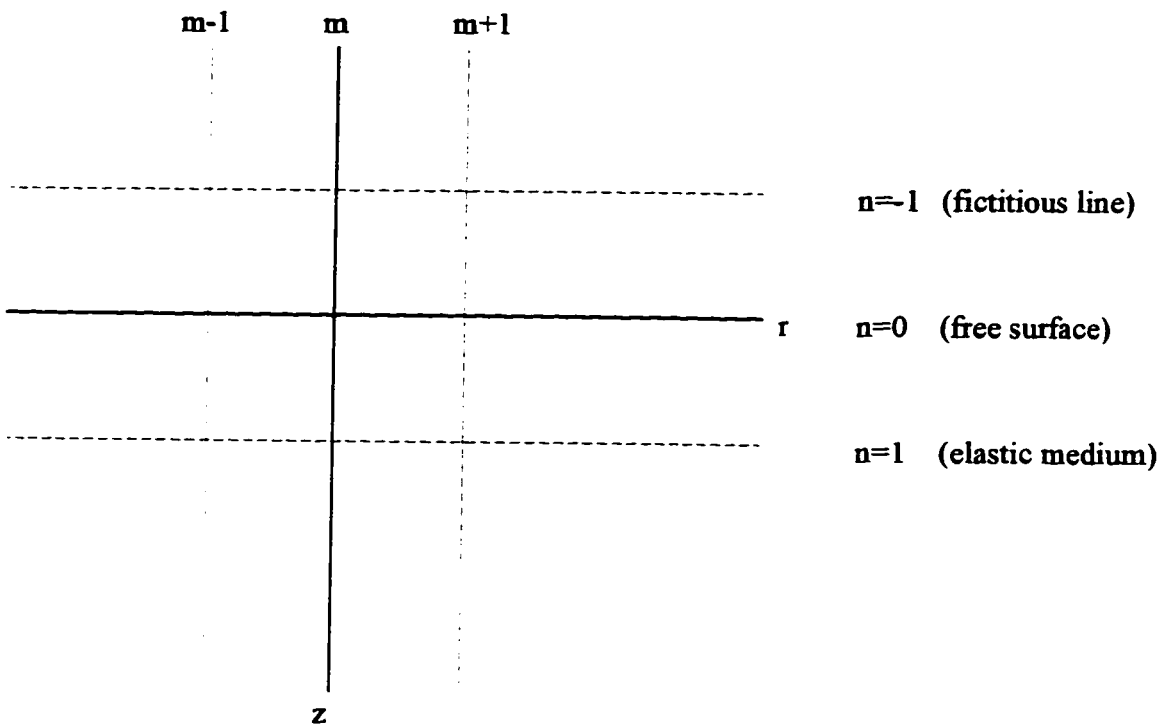

Figure 3.5. Grid geometry at the surface showing the imaginary line of grid points and the free boundary.

scheme provided accurate and reliable results when implemented in cylindrical and rectangular coordinate systems. This method appears to be an adequate simulation tool for modeling the dynamic response of concrete systems.

Chapter 4

TWO-DIMENSIONAL MAGNETIC ALGORITHM TO DETECT REINFORCING STEEL

This section presents a new two-dimensional algorithm to determine locations and sizes of steel reinforcing bars in concrete. Detection of reinforcing steel in concrete was identified in Chapter 1 as an area that may benefit from a less simplified or more computationally intense nondestructive evaluation method. The test procedure is presented first, followed by derivation of the two-dimensional relationships on which the method relies.

OVERVIEW OF ALGORITHM

The underlying physical phenomenon for this algorithm is the same as that exploited by the three-dimensional algorithm presented by Pla, Eberhard, and Eberhard (1994). The two-dimensional reconstruction procedure consists of the following steps:

1) A long coil, generating a magnetic field $\mathbf{B}_o$, is used to magnetize the steel within a concrete member. This magnetization induces an additional field, $\mathbf{B}''$, at all points in space (Figure 1.1).

2) The two vector components of the total magnetic field, $\mathbf{B}$, normal to the length of the bars are measured outside the member. This field is the sum of $\mathbf{B}_o$ and $\mathbf{B}''$.

3) The measured distortion in the magnetic field, $\mathbf{B}''_{meas}$, caused by the steel inside the member, is determined by subtracting the magnetic field generated by the coil from the total magnetic field (i.e., $\mathbf{B}''_{meas} = \mathbf{B} - \mathbf{B}_o$).

4) For a trial configuration of reinforcing bars (trial x-coordinates, y-coordinates, and area values for an assumed number of bars), $\mathbf{B}_o$ at the center of each bar is computed.

5) The magnetic dipole density, $\mathbf{M}$, for each trial bar is determined by simultaneously solving two sets of equations. The first equation relates $\mathbf{M}$ to the magnetic field to which the bar is subjected. This field is the sum of the imposed magnetic field, $\mathbf{B}_o$, and the magnetic field caused by magnetization of the other bars, $\mathbf{B}''$.

$$\mathbf{M} = \frac{\chi_m}{\mu_o\left(1+0.5\chi_m\right)}\left(\mathbf{B}_o+\mathbf{B}''\right) \qquad (4.1)$$

where χ_m is the magnetic susceptibility of the steel and μ_o is the permeability constant in vacuum ($4\pi 10^{-7} N/A^2$). The second equation relates magnetic

distortion at the location of one bar, $\mathbf{B}''$, to the magnetic dipole density, $\mathbf{M}$, at another bar:

$$\begin{Bmatrix} B''_x \\ B''_y \end{Bmatrix} = \frac{\mu_o A_{steel}}{2\pi(x^2+y^2)^2} \begin{bmatrix} x^2-y^2 & 2xy \\ 2xy & y^2-x^2 \end{bmatrix} \begin{Bmatrix} M_x \\ M_y \end{Bmatrix} \tag{4.2}$$

where x and y represent the distances along the x and y axes, respectively, from the bar having the influence to the bar being investigated. Both Equations 4.1 and 4.2 are derived in the next section.

6) Equation 4.2 is used to calculate the distortion in the magnetic field at the receivers, $\mathbf{B}''_{calc}$. In this step, $\mathbf{M}$ is the magnetic dipole density at a bar, and x and y are the distances from the bar to the receiver.

7) The sum of squared differences (SSD) is computed for all of the receivers:

$$SSD = \left(\mathbf{B}''_{meas} - \mathbf{B}''_{calc}\right)^T \left(\mathbf{B}''_{meas} - \mathbf{B}''_{calc}\right) \tag{4.3}$$

8) New configurations are selected, and Steps 4 to 7 are repeated, until SSD is minimized. This minimization results in the identification of the locations and sizes of reinforcing bars that would cause magnetic distortions most similar to those measured.

TWO-DIMENSIONAL RELATIONSHIPS

The proposed algorithm relies heavily on Equations 4.1 and 4.2, which are derived in this section. In deriving these equations, the steel is assumed to be square in cross-section and infinitely long. It is also assumed that the magnetic field is constant along the length of the bar and over the bar's cross-section.

Magnetization Induced by Ambient Magnetic Field

A relationship between magnetic dipole density (**M**) and ambient magnetic field ($\mathbf{B}_0+\mathbf{B}''$) can be developed for the geometry shown in Figure 4.1. The reinforcing bar is square in cross-section (xy-plane), and extends to infinity in the z direction. If **M** is assumed constant within the reinforcing bar, the magnetization can be modeled with a current distribution on the surface of the steel (Nayfeh and Brussel 1985). For this geometry, the current distribution consists of differential current loops. The magnitudes of the currents are $M_x dx$ and $M_y dy$ for loops about the x-axis and y-axis, respectively (Figure 4.1).

Magnetization of the steel causes a magnetic field, **B'**, within the bar. This field can be determined from the current distribution. If the bar extends to infinity, only currents along the length (z-direction) of the bar contribute to **B'**. Therefore, the x- and y-components of the magnetic field caused by a single loop can be computed as the sum of the contributions from two, infinitely-long, wires. Starting with Biot-Savart's law (Nayfeh and Brussel 1985), it can be shown that the magnetic field generated by a single wire with current, I, is the following:

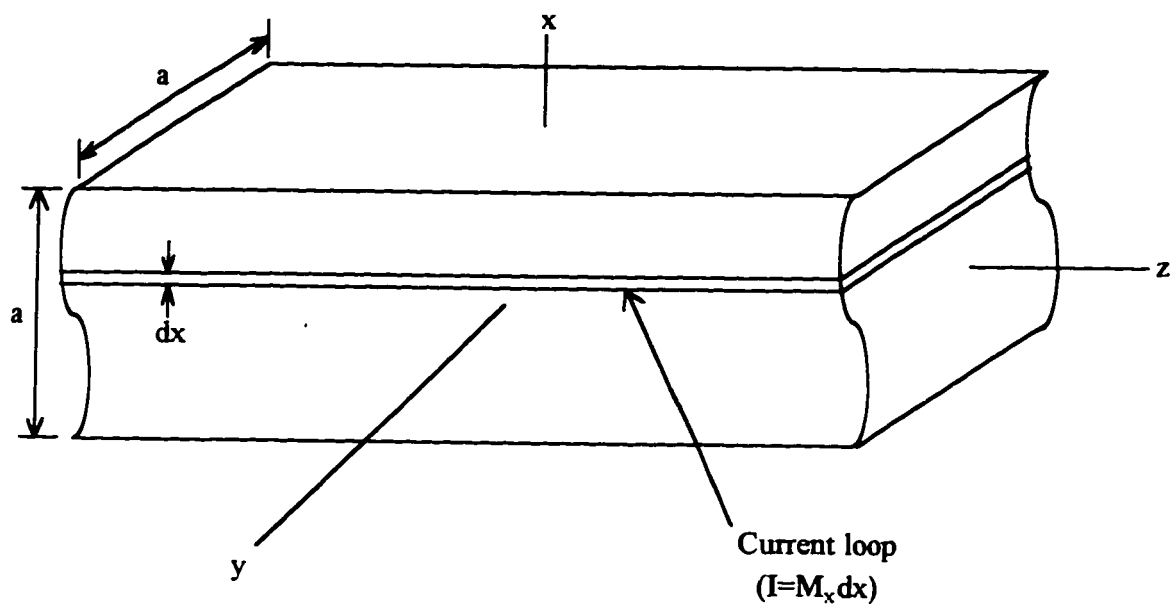

Figure 4.1. Differential current loop on the surface of a rectangular bar.

$$\mathbf{B} = \frac{\mu_o I}{2\pi r} \left(\mathbf{k} \times \frac{\mathbf{r}}{r}\right) \tag{4.4}$$

where **r** is the two-dimensional vector from the wire centroid to the point being considered (the center of the bar), r is the magnitude of vector **r**, and **k** is a unit vector parallel to the direction of current.

The resulting magnetic field, **B'**, is the sum of the contributions of all the differential current loops. For the x-component, the following is obtained:

$$B_x' = \int_{-a/2}^{a/2} \frac{\mu_o M_x}{\pi \sqrt{\left(\frac{a}{2}\right)^2 + x^2}} dx \tag{4.5}$$

Performing this integration for both the x- and y-components results in the following:

$$\mathbf{B}' = \frac{\mu_o}{2} \mathbf{M} \tag{4.6}$$

For low values of magnetic intensity, magnetization varies linearly with the magnetic field (Bleaney 1965). Therefore, we can write the following relationship:

$$\mathbf{M} = \frac{\chi_m \left(\mathbf{B}_o + \mathbf{B}'' + \mathbf{B}'\right)}{\mu_o \left(1 + \chi_m\right)} \tag{4.7}$$

Substituting Equation 4.6 into Equation 4.7 allows the magnetic dipole density to be expressed as a function of the ambient magnetic field at a reinforcing bar. This relationship was previously defined as Equation 4.1:

$$\mathbf{M} = \frac{\chi_m}{\mu_o\left(1+0.5\chi_m\right)}\left(\mathbf{B}_o+\mathbf{B}''\right) \tag{4.1}$$

Two-Dimensional Magnetic Dipole Formula

The two-dimensional magnetic dipole formula, Equation 4.2, relates distortion in the magnetic field, **B''**, at one point to the magnetic dipole moment at another point. This relationship may be derived from the three-dimensional magnetic dipole formula (Nayfeh and Brussel 1985):

$$\mathbf{B}'' = \frac{\mu_o}{4\pi R^3}\left[3\left(\mathbf{m}\cdot\frac{\mathbf{R}}{R}\right)\frac{\mathbf{R}}{R}-\mathbf{m}\right] \tag{4.8}$$

where **R** is the vector from the magnetized material to the point where the magnetic field is being investigated, and **m** is the magnetic dipole moment.

In the two-dimensional case, the reinforcing bars are assumed to be infinitely long and uniformly magnetized by a long coil. Therefore, the distortion in the magnetic field at a point is the sum of the distortions caused by an infinite number of differential volumes, as shown in Figure 4.2.

The x-component of **B''** caused by a single differential element, dB''_x, can be obtained by expanding Equation 4.8 and substituting $\mathbf{M}A_{steel}dz$ for **m**:

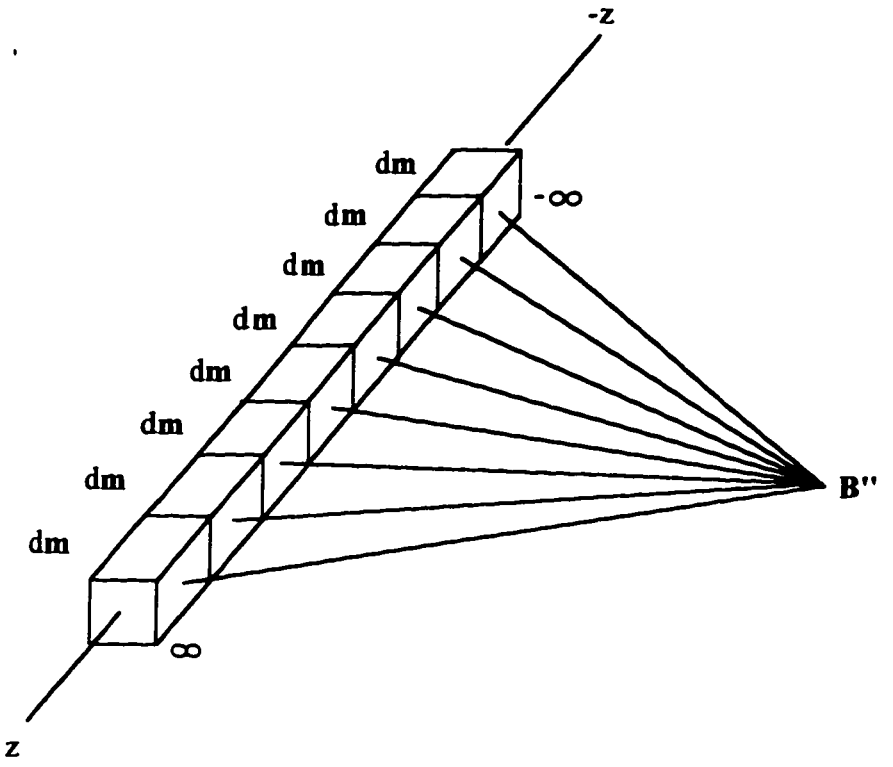

Figure 4.2. Differential magnetic dipole moments causing distortion in the magnetic field.

$$dB_x'' = \frac{\mu_o A_{steel}\, dz}{4\pi\left(x^2+y^2+z^2\right)^{5/2}}\left[3\left(M_x x + M_y y + M_z z\right)x - M_x\left(x^2+y^2+z^2\right)\right] \qquad (4.9)$$

where the dimensions x, y, and z are measured from the center of the magnetized element to the point at which the distortion in the magnetic field is being evaluated. Similar expressions may be obtained for dB_y'' and dB_z''. Integrating these expressions from negative infinity to positive infinity in the z-direction, Equation 4.2 is obtained:

$$\begin{Bmatrix} B_x'' \\ B_y'' \end{Bmatrix} = \frac{\mu_o A_{steel}}{2\pi\left(x^2+y^2\right)^2}\begin{bmatrix} x^2-y^2 & 2xy \\ 2xy & y^2-x^2 \end{bmatrix}\begin{Bmatrix} M_x \\ M_y \end{Bmatrix} \qquad (4.2)$$

There is no need to measure the z-component of the magnetic field because, theoretically, B_z'' is zero.

SUMMARY

An algorithm is proposed to detect reinforcing steel in concrete. The algorithm uses an optimization technique to determine the most probable locations and sizes of reinforcing bars in a concrete member. Optimizing the measurements of the magnetic field greatly diminishes the number of measurements needed to investigate a concrete member. Many more measurements would be required if the member were discretized in a manner similar to Pla, Eberhard, and Eberhard's (1994) algorithm.

Derivations of the two-dimensional relationships that support the algorithm were also presented. Two-dimensional modeling of steel bars in concrete exploits the geometry of the problem to reduce the number of measurements at each receiver. Only two vector components of the magnetic field need to be measured at each receiver location.

Chapter 5

APPLICATION OF THE MAGNETIC ALGORITHM

This chapter discusses implementation and application of the two-dimensional magnetic algorithm developed in Chapter 4. The algorithm is applied to simulated problems containing one and two reinforcing bars. A sensitivity analysis of the algorithm is also presented.

IMPLEMENTATION OF ALGORITHM

The reconstruction algorithm (Steps 4-8) has been implemented with the software package MATLAB (Sigmon 1992). The user provides the magnetic field generated by the coil ($\mathbf{B}_o$), the measured total magnetic field ($\mathbf{B}$), and initial trial values of the bar coordinates and areas. Then, the program computes the distortion in the magnetic field at the receivers, and the difference between the computed and measured distortions. The output of the program is the bar configuration that minimizes the sum of squared differences (SSD), which is defined in Equation 4.3.

Two optimization commands are used to minimize SSD. SSD is minimized using a simplex solution method described by Nelder and Mead (1964) with the fmins()

command (Grace 1990). SSD is also minimized using the leastsq() command, using a search algorithm based on Levenberg's (1944) and Marquardt's (1963) work. The algorithm used by leastsq(), which is intended for least squares problems, is described by More (1977).

One-Bar Problems

If it is assumed that only one steel bar is present, three variables need to be determined. These variables are the bar's horizontal location (x-coordinate), depth (y-coordinate), and area (A_{steel}). The initial trial values were x = 0, y = 10 mm, and A_{steel} = 100 mm^2. Assuming that only one bar is present makes it possible to simplify the algorithm, because there is no distortion in the magnetic field at the bar due to magnetization of another bar. Therefore, **B**'' in Equation 4.1 is zero, and Equation 4.2 may be ignored in Step 5 of the algorithm.

The algorithm used to determine the location and size of one bar minimized SSD with both optimization commands. In almost all cases, both commands yielded the same result. In those few cases where the results differed, the result with the lowest SSD was selected as the algorithm's solution to the problem.

Two-Bar Problems

If two bars may be present, the number of variables doubles and the complexity of the governing equations increases. The number of unknown variables increases to six: two x-coordinate values, two y-coordinate values, and two area values. In addition, interaction between reinforcing bars must be considered because the magnetized steel in one bar will distort the magnetic field at the other bar (Equation 4.2).

The procedure used to identify as many as two bars involved solving the problem as if one bar were present (Figure 5.1a) and then solving the problem as if two bars were present (Figure 5.1b). Initial trial values for the two-bar problems were x = -10 mm, y = 10 mm, and A_{steel} = 100 mm^2 for one bar and x = 10 mm, y = 10 mm, and A_{steel} = 100 mm^2 for the second bar. During preliminary investigations, it was found that the minimization commands often converged to a local minimum when two bars were close together. In particular, the computed configuration consisted of one large bar at an intermediate position (Figure 5.1b) and a second bar with an unrealistic location or an area that was either negative or excessively large.

To obtain the global minimum for SSD, four additional trial configurations were provided (Figure 5.1c-f). The four additional configurations were based on the results of the first two-bar minimization (Figure 5.1b). In particular, trial configurations for other two-bar solutions were selected that represented diagonal corners of one of the two bars identified by the initial two-bar solution. Both bars in the new trial configuration were assigned areas equal to one half that of the bar being split. The splitting process was repeated so that both bars identified by the initial two-bar solution were split twice, once along each diagonal. The series of initial trial locations is described in Figure 5.1. This process was performed with both optimization commands. The lowest SSD from the 12 solutions was selected as the best solution.

SIMULATIONS

Finite-element analyses were conducted on configurations containing rectangular steel bars to provide input data with which to test the reconstruction algorithm. All of the analyses were conducted with the same finite-element mesh. The model was prepared and analyzed with ANSOFT's Maxwell 2-D Field Simulator (Maxwell 1991), which uses a

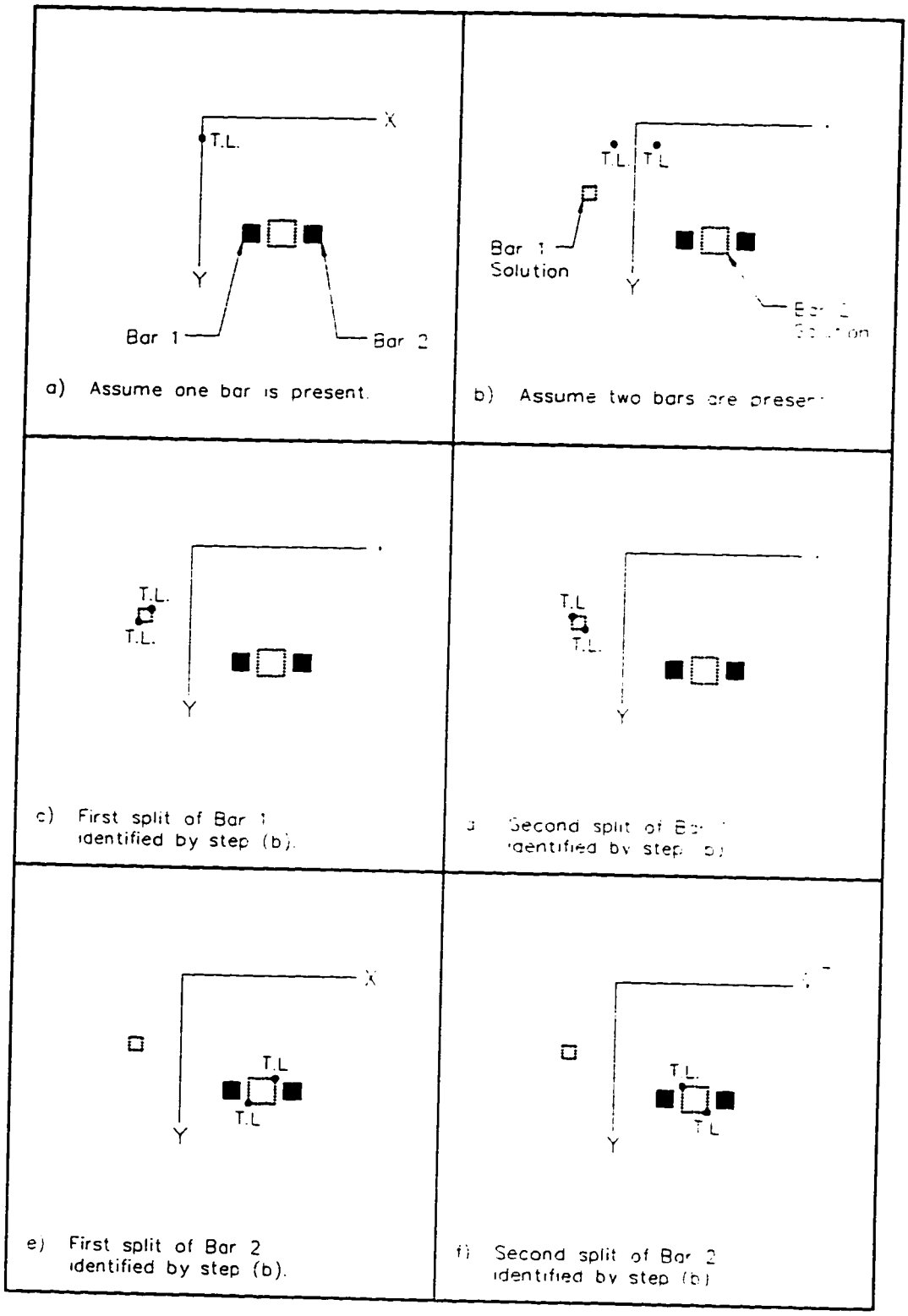

Fig. 5.1. Sequence of initial trial locations (T.L.) for two-bar search algorithm.

conjugate gradient method to solve magnetostatic problems. This finite element model used 30,881 triangular elements to describe the geometry shown in Figure 5.2. The outer boundary of the problem was located at a value of 200 mm in each coordinate direction. The conjugate gradient solver was allowed to perform 575 iterations on every problem simulated.

Two 2x2 mm wires with 1000A currents flowing in opposite directions were used to model the long coil. These wires were placed 120 mm apart center-to-center, symmetrically about the y-axis, and resting in the xz-plane. Five receiver locations were included in the model. They are denoted by R1 through R5 in Figure 5.2.

Eight possible locations for steel reinforcing bars were also provided. They are labeled as V1 through V8 in Figure 5.2. Potential locations of reinforcing bars were square in cross-section with dimension 12 mm, which corresponds to one-tenth of the coil's wire spacing. The cross-sectional area of 144 mm^2 was close to the nominal area of a #4 reinforcing bar, 127 mm^2. In locations where steel was present, the relative permeability was specified to be 2000 (CRC 1992). In all other locations, the relative permeability was specified to be 1.0 (the value associated with free space).

To describe the bar geometries with nondimensional quantities, two parameters were defined. The ratio of bar depth to the distance between the coil wires was defined as the depth factor alpha, and the ratio of the x-coordinate to the distance between wires was defined as the horizontal location factor beta.

One-Bar Problems

Configurations containing one bar were analyzed with the bar located at x-coordinate equal to zero and increasing depths (y-coordinates) of 30, 45, 60, and 90 mm. These depths correspond to alpha equal to 0.25, 0.375, 0.5, and 0.75. Configurations were also analyzed for a depth equal to one half the coil wire spacing and x-coordinates of

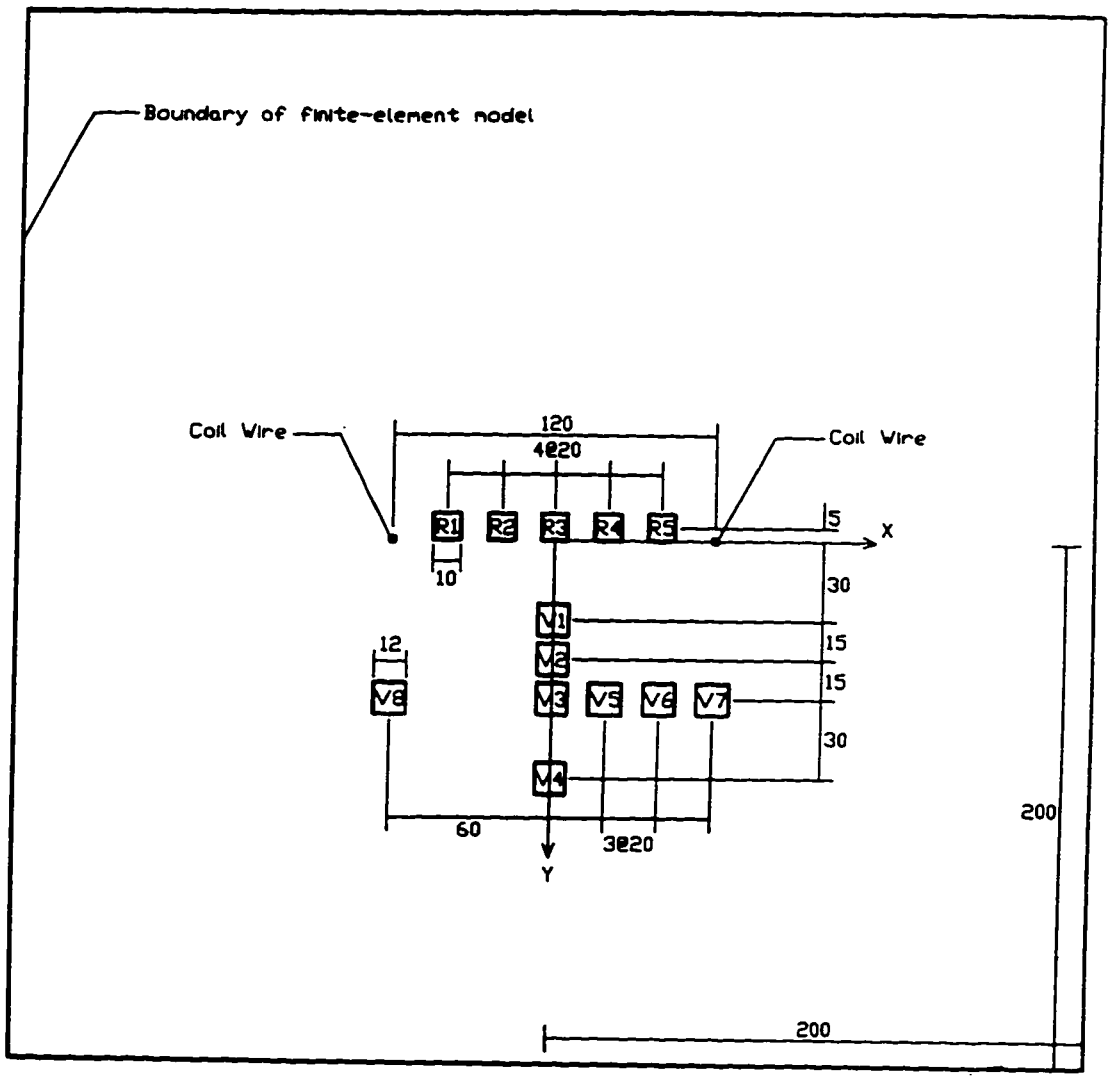

Fig. 5.2. Geometry of finite-element model (all units in millimeters).

0, 20, 40, and 60 mm. These x-coordinates correspond to beta values of 0, 0.167, 0.333, and 0.5. Errors in the reconstructed coordinates were normalized with respect to the exact depth of the bar, and errors in reconstructed area were normalized with respect to the exact area.

Results for the one-bar problems are presented in Table 5.1. Normalized errors in the x- and y-coordinates were all less than 1.5 percent. They did not increase or decrease consistently with increasing coordinate values. The results also show that the error in bar area decreased as the x-coordinate or the y-coordinate of the bar increased. However, this decrease, less than 2.5 percent error over the range of alpha and beta, was small compared to the total error in the bar areas (approximately 8 to 10 percent).

Two-Bar Problems

Configurations containing two bars were analyzed with the same finite-element mesh used to analyze the one-bar problems. Reconstructions were performed with the bars at various horizontal spacings and with the bars at various vertical spacings. In particular, effects of horizontal spacing were investigated by analyzing configurations 7-8, 3-7, 3-6, and 3-5, where the two numbers in each configuration name refer to the volume elements filled with steel (Figure 5.2). The center-to-center bar spacing in each configuration was 120, 60, 40, and 20 mm, respectively. In all of these configurations, the bar depths were 60 mm.

The results of implementing the two-bar search algorithm are reported in Table 5.2 and Figure 5.3. Normalized errors from the exact values associated with these results are plotted against the ratio of bar depth to bar spacing for horizontally spaced bars in Figure 5.3. Again, errors in the coordinates were normalized with respect to the exact depth of the bar, and errors in area were normalized with respect to the exact area.

TABLE 5.1. Locations and sizes determined for one-bar problems.

alpha	beta	Exact Values	Minimization Results	Normalized Error
y_o/w^*	x_o/w^*	x_o (mm) y_o (mm) A_o (mm^2)	x (mm) y (mm) A (mm^2)	(%)
Varying Horizontal Location				
0.5	0	0 60 144	0 60.0 156.0	0.0 0.0 8.3
0.5	0.167	20 60 144	19.5 59.9 155.5	0.8 0.2 8.0
0.5	0.333	40 60 144	39.1 59.7 154.9	1.5 0.5 7.6
0.5	0.5	60 60 144	59.5 59.4 154.0	0.8 1.0 6.9
Varying Vertical Location				
0.25	0	0 30 144	0 30.3 158.5	0.0 1.0 10.1
0.375	0	0 45 144	0 45.1 156.8	0.0 0.2 8.9
0.5	0	0 60 144	0 60.0 156.0	0.0 0.0 8.3
0.75	0	0 90 144	0 89.9 155.1	0.0 0.1 7.7

* w is the width of the coil (120 mm).

TABLE 5.2. Locations and sizes determined for two-bar problems.

Bar Configuration	Bar 1 Exact Values x (mm) y (mm) A_{steel} (mm^2)	Bar 1 Results x (mm) y (mm) A_{steel} (mm^2)	Bar 2 Exact Values x (mm) y (mm) A_{steel} (mm^2)	Bar 2 Results x (mm) y (mm) A_{steel} (mm^2)
Horizontally-Spaced Bars				
7-8	-60 60 144	-59.4 59.2 152.5	60 60 144	59.4 59.0 151.1
3-7	0 60 144	-0.9 59.0 141.9	60 60 144	57.3 61.4 174.4
3-6	0 60 144	-2.2 58.2 122.5	40 60 144	36.2 61.6 192.6
3-5	0 60 144	-1.6 59.1 133.8	20 60 144	19.3 60.2 168.6
Vertically-Spaced Bars				
1-4	0 30 144	0 30.9 169.3	0 90 144	1.4 129.5 302.7
2-4	0 45 144	0 45.6 165.2	0 90 144	0.1 92.7 144.1
3-4	0 60 144	0 59.5 135.0	0 90 144	0 83.7 154.3
2-3	0 45 144	0 46.2 155.6	0 60 144	0 58.6 117.1

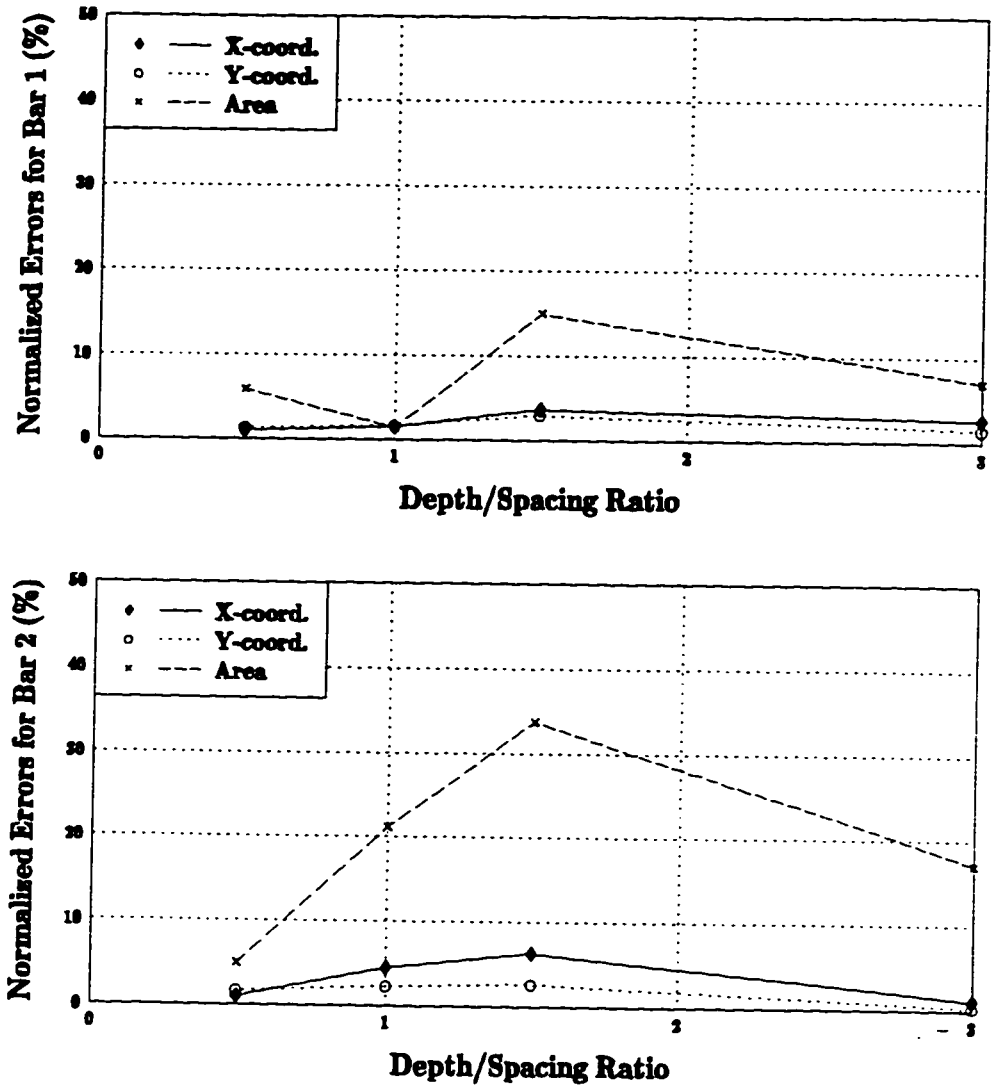

Fig. 5.3. Effects of horizontal spacing.

Figure 5.3 shows that the algorithm effectively identified two horizontally spaced bars. The identification was successful even when the clear distance between the bars was less than the dimension of the bars (Depth/Spacing ratio > 2.5).

Effects of vertical spacing were investigated by analyzing configurations 1-4, 2-4, 3-4, and 2-3. Normalized errors from the algorithm's solutions for vertically-spaced bars are plotted against the ratio of the depth of Bar 2 (deepest bar) to the depth of Bar 1 (shallowest bar) in Figure 5.4. These plots show that the algorithm identified both bars with less than 20 percent error when the ratio of bar depths was 2 or less. The algorithm was unable to identify the bar farthest from the receivers when the ratio of bar depths was equal to 3. The closer bar masked the influence of the farther bar, because the closer bar caused much greater distortion in the magnetic field. As the farthest bar's contribution to the distortion decreased in proportion to the contribution of the shallow bar, the problem became similar to a problem that contained only one bar.

SENSITIVITY TO MEASUREMENT ERROR

The error sensitivity of the proposed algorithm is an important consideration for future development, because distortions in the magnetic field must be measured in the presence of a magnetic field of much greater intensity. For example, the ratios of $\mathbf{B}''$ to $\mathbf{B}_0$ ranged from about 0.0011 to 26 across the receivers when the bar was located at alpha equal to 0.25 (depth = 30 mm) and beta equal to zero. When alpha was increased to 0.75 (depth = 90 mm), the ratios ranged from 0.0006 to 0.9660. To quantify the algorithm's sensitivity to measurement errors, sensitivity analyses were performed for all of the one-bar configurations and for one of the two-bar configurations (configuration 7-8).

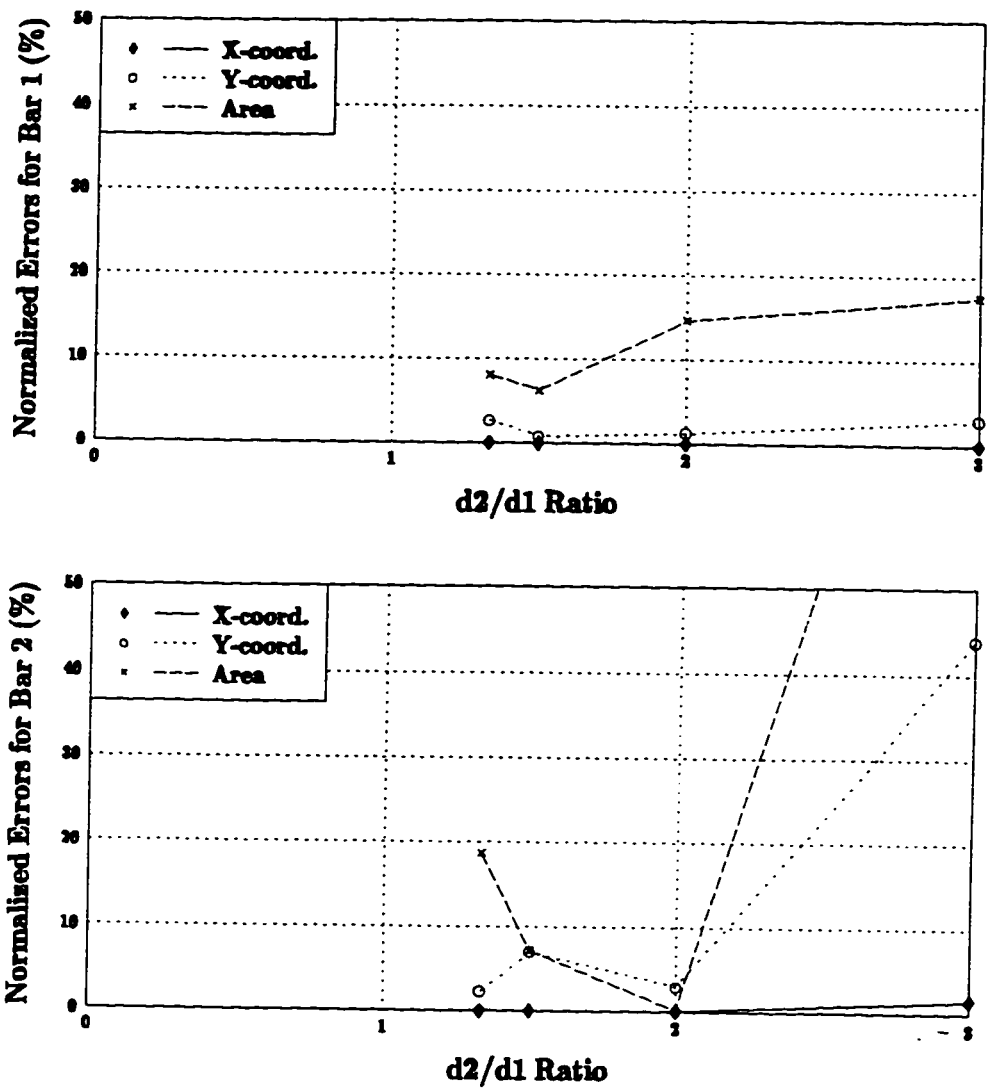

Fig. 5.4. Effects of vertical spacing.

One-Bar Problems

For configurations containing one bar, each of the measured distortions was modified by the addition of induced random errors. The induced errors had a mean of zero and standard deviation, σ, calculated as follows:

$$\sigma = \xi \sqrt{\frac{\{\mathbf{B''}\}^T \{\mathbf{B''}\}}{n}} \tag{5.1}$$

where ξ ranged from 1 to 20 percent and n was the number of components in $\mathbf{B''}$ (twice the number of receivers). At each percentage level of induced error, the reconstruction was performed 50 times, each time with new random errors. The minimization routine used to solve problems containing one bar was then used to determine the location and size of each bar for each set of erroneous simulated measurements.

The mean absolute normalized errors from the algorithm solutions were plotted against the percentage of induced error. These plots are shown for a bar with varying depth in Figure 5.5 and for a bar with varying x-coordinate in Figure 5.6. These plots show that error sensitivity increased with increasing bar depth or x-coordinate value. Nevertheless, even when as much as 20 percent error was induced in the measured distortions, errors in resulting bar locations were less than 15 percent. Errors in determined bar areas were all less than 50 percent, which would result in an error of no more than one bar size for a #4 reinforcing bar.

Two-Bar Problems

A similar error analysis was conducted on bar configuration 7-8 (Figure 5.2). In this error analysis, the induced errors ranged from 1 to 10 percent. Solution errors in coordinates and areas, normalized as before, are plotted against the induced error in

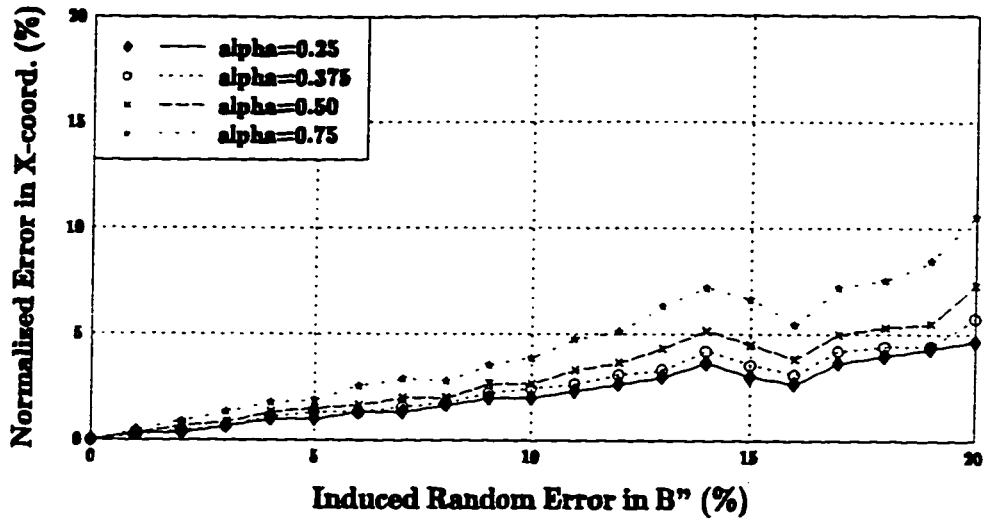

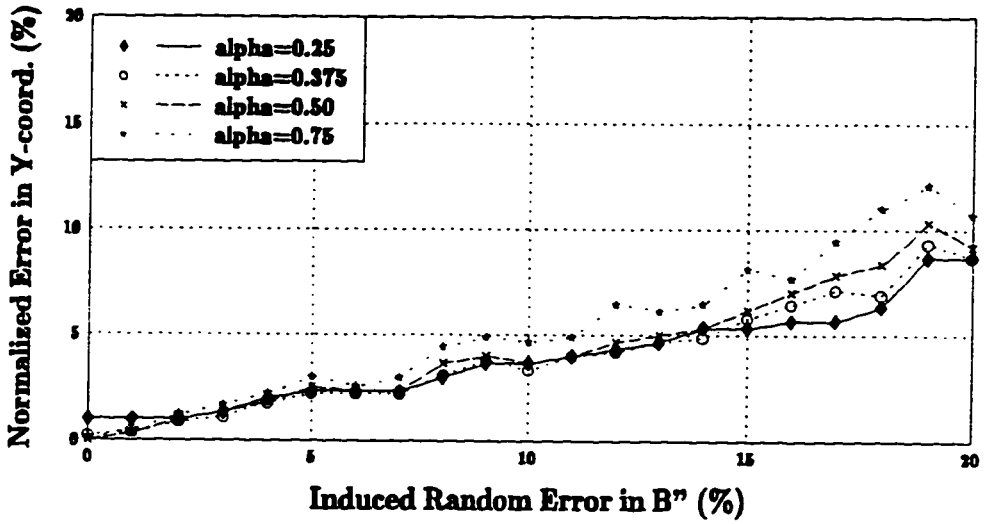

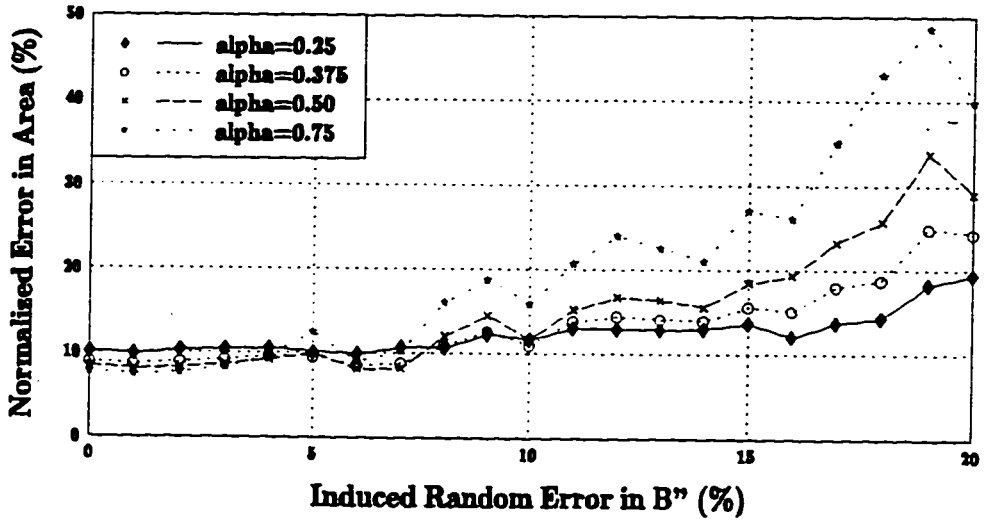

Fig. 5.5. Single bar with increasing depth.

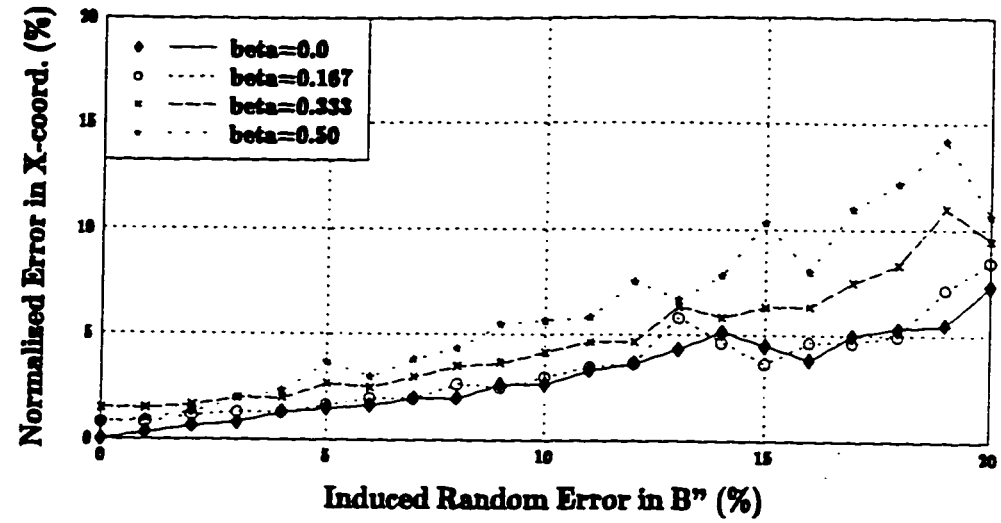

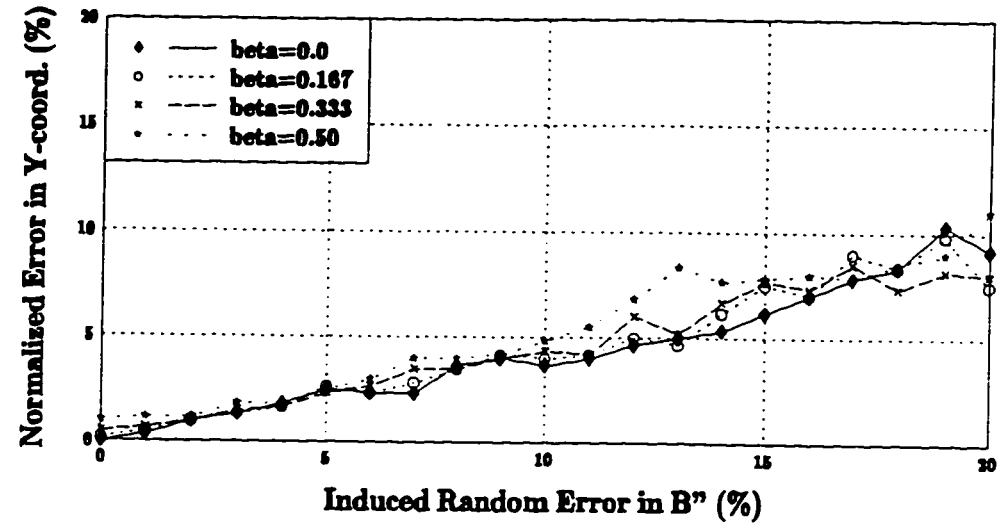

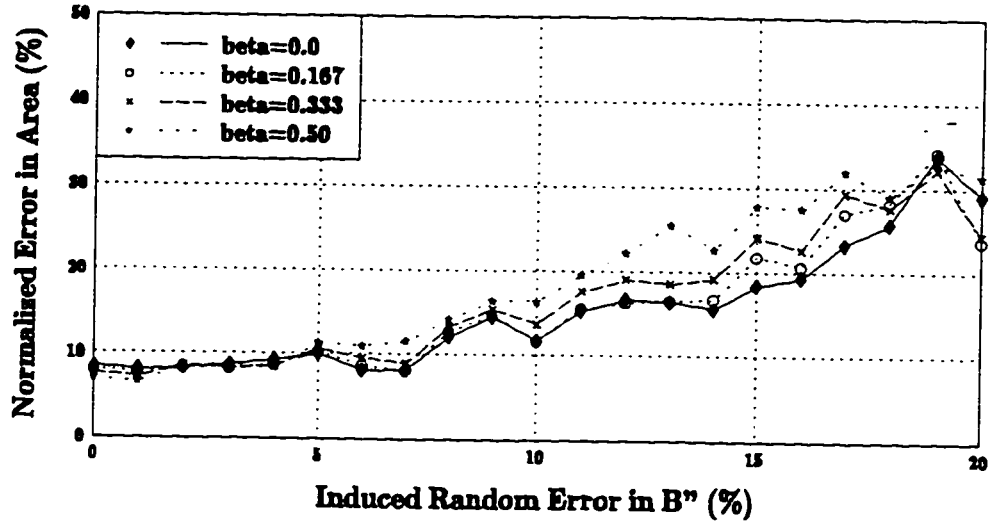

Fig. 5.6. Single bar with increasing x-coordinate.

Figure 5.7. These plots show that when the induced error in **B"** exceeded 3 percent, the area values determined by the search algorithm differed greatly from the exact values.

The sensitivity analysis was repeated with A_{steel} for both bars held at 144 mm^2, representing a scenario in which the bar sizes are known and the locations need to be determined. Hence, there were only four unknown variables in the problem (x- and y-coordinates for two bars). Plots of normalized errors in the x- and y-coordinates against induced error are provided in Figure 5.8. The algorithm's sensitivity to errors decreased when the bar areas were known in advance. In fact, the largest normalized error was approximately 15 percent when 10 percent error was induced in the magnetic measurements. This error corresponds to 9 mm, which is less than the bar dimension.

These observations demonstrate that the algorithm needed accurate measurements to determine the area of more than one bar. However, if the areas of the bars were already known, the algorithm identified the locations of the bars even in the presence of errors. Design and selection of measurement equipment should be based on the information provided by these sensitivity analyses.

SUMMARY

In applications requiring the detection of a single reinforcing bar, the magnetic detection algorithm accurately determined the bar's location and size. The algorithm's ability to identify a single bar did not appear to be sensitive to the errors induced in the measurements of magnetic distortion.

The algorithm was also able to identify the locations of two bars if the bar depths were approximately the same. If one of the two bars was much closer to the receivers, only the closest bar was accurately identified by the algorithm. For problems involving two bars with unknown areas, the algorithm was unable to identify either bar accurately

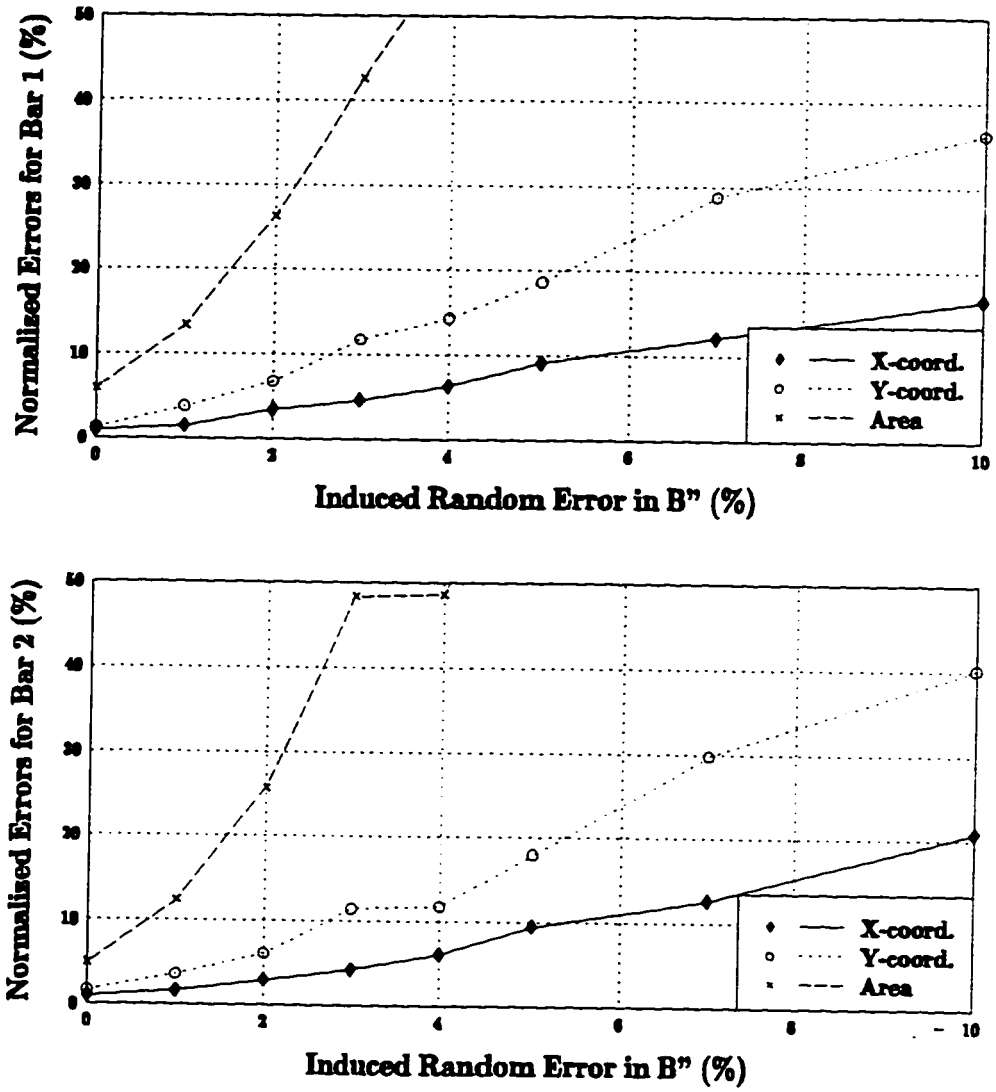

Fig. 5.7. Sensitivity analysis for configuration 7-8.

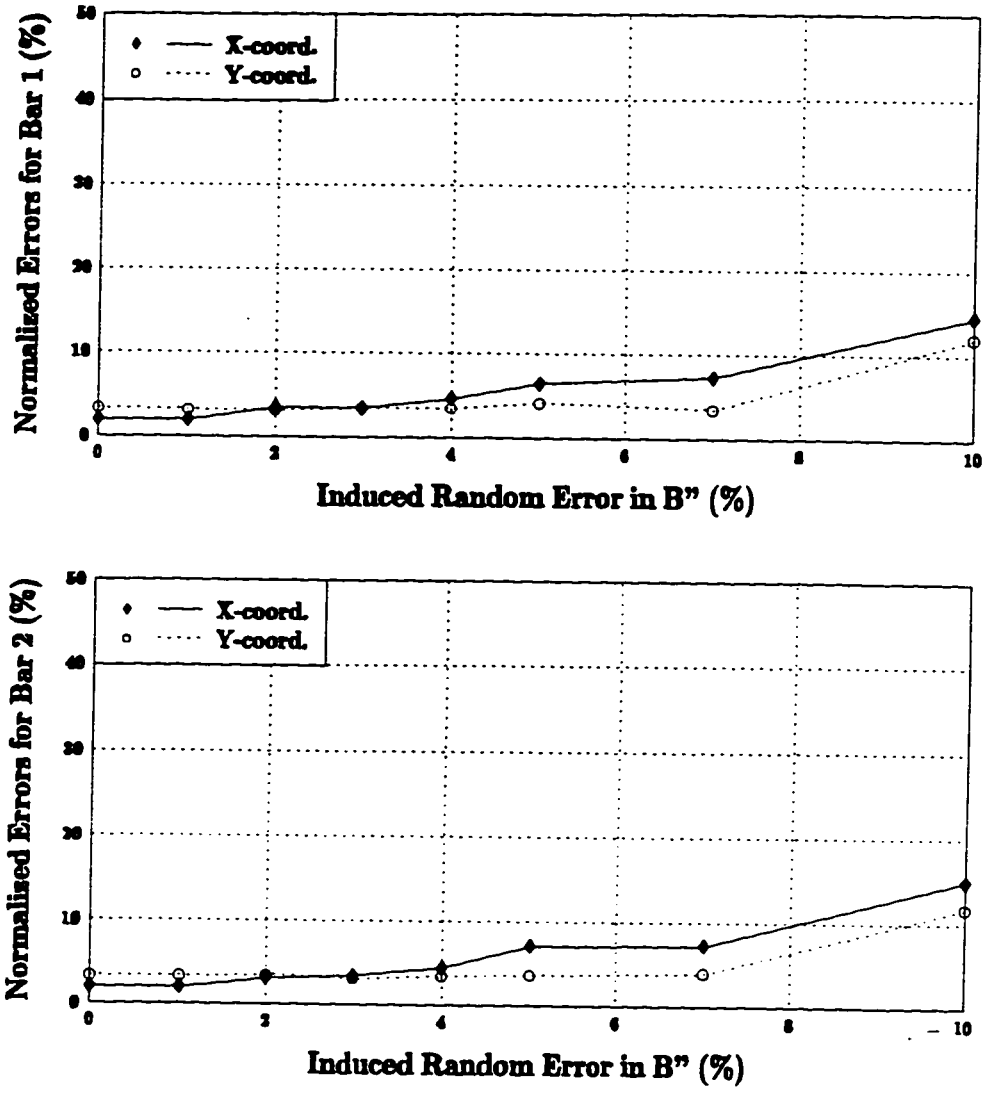

Fig. 5.8. Sensitivity analysis with A_{steel} set equal to 144 mm^2 for both bars.

when small errors were induced in the measured distortions. If the areas of both bars were known, the algorithm was able to accurately locate both bars, even in the presence of 10 percent induced error.

Chapter 6

INFLUENCE OF THE MAGNETIC PROPERTIES OF CONCRETE

In the analyses described in Chapter 5, the concrete was assigned the magnetic susceptibility of free space. This modeling assumption was made to verify that the magnetic distortion caused by the steel could be used to identify the steel configuration when the concrete's magnetic susceptibility is negligible. In actuality, the concrete in the member and the air surrounding the concrete will contribute to the magnetic distortion. To investigate the influence of the concrete's magnetic properties on the measured magnetic distortion, the magnetic susceptibility of various concrete mixtures were measured, and simulations were performed assuming a broad range of magnetic susceptibility values for the concrete.

CONCRETE MATERIALS AND MIXTURES

Six concrete mixtures were prepared. Coarse aggregate type, coarse aggregate content, and flyash content content were varied in the mixtures to obtain a range of magnetic susceptibility values. Saturated surface-dry mixture quantities for all the mixtures are presented in Table 6.1. Type I-II cement and a water-cementitious ratio of

Table 6.1. Composition of concrete mixtures.

Mixture Ref.	Coarse Aggregate Type	Coarse Aggregate Content	Fly Ash	Coarse Aggregate	Fine Aggregate	Cement	Fly Ash	Water
A	Limestone	Low	No	967	740	449	0	202
B	Limestone	Low	Yes	967	719	337	112	202
C	Basalt	Low	No	971	788	449	0	202
D	Basalt	Low	Yes	971	767	337	112	202
E	Basalt	High	No	1187	731	376	0	169
F	Basalt	High	Yes	1187	713	282	93.9	169

All quantities are kg/m^3.
All quantities are for saturated surface dry conditions.

0.45 were used in all six mixtures. The mixtures were also similar in that they all contained fine aggregates from the same source and the maximum coarse aggregate size was 25 mm.

Two types of coarse aggregates were used: a crushed limestone and a crushed basalt. The limestone was selected because it was expected to have a low magnetic susceptibility (low ferrous-oxide content), and the basalt was chosen because it was expected to have a high magnetic susceptibility. Flyash was included in three of the mixtures. The flyash was 27.8 percent Fe_2O_3 by mass. This is a high ferrous-oxide content for flyash. It was selected to produce a concrete with a high magnetic susceptibility.

Two of the concrete mixtures (A and B) were produced using limestone coarse aggregates. One of these mixtures contained no flyash (A). In the second mixture (B), 25 percent of the cement (by mass) was replaced with flyash. The Portland Cement Association's (Design 1990) recommended coarse aggregate contents were reduced by 10 percent for these mixtures.

Four mixtures were prepared with basalt coarse aggregates. Two of these mixtures (C and D) were proportioned with the same coarse aggregate contents (by volume) used for the mixtures containing limestone aggregates. The other two mixtures (E and F) were proportioned with coarse aggregate contents 10 percent higher than recommended by the Portland Cement Association (Design 1990). For both the low coarse aggregate content mixtures and the high coarse aggregate content mixtures, one mixture was produced without flyash (C and E) and one mixture was produced with 25 percent replacement of the cement with flyash (D and F).

Each batch of concrete was used to prepare two 75x106x406 mm prisms. Prisms were compacted in two lifts on a vibrating table. Specimens were covered in plastic to

cure for 24 hours and then moved to a fog room to cure until they reached an age of seven days.

MAGNETIC SUSCEPTIBILITY TESTING

When the concrete specimens were seven days old, one prism from each mixture was removed from the fog room and cored. Five 25 by 75 mm cores were cut from each prism. To remove the high paste regions that had been cast at the tops and bottoms of the prisms, cores were sawed to a length of 51 mm by removing 12 mm from each end of the core. The cores were then cut in half to obtain two 25 by 25 mm magnetic susceptibility test specimens. This process produced ten test specimens from each mixture. Magnetic susceptibility was measured with an Exploranium KT-5 magnetic susceptibility meter. The KT-5 has a sensitivity of 10^{-5} SI units and operates at a frequency of 10 kHz. The tests were conducted in the Department of Oceanography at the University of Washington. Each end of each specimen was tested three times for a total of 60 tests for each mixture.

A summary of the results for the magnetic susceptibility tests is provided in Table 6.2. The mixture containing limestone coarse aggregates and no flyash (A) yielded the lowest magnetic susceptibility value. This result was expected because the mixture did not contain materials with high magnetic susceptibilities. Mixtures containing basalt coarse aggregates consistently yielded magnetic susceptibilities higher than similar limestone mixtures. For example, mixture C had a magnetic susceptibility greater than mixture A by approximately a factor of two. This was also expected because the limestone has little or no ferrous-oxide in its composition. Surprisingly, coarse aggregate content of the mixtures containing basalt coarse aggregates did not significantly effect magnetic susceptibility. The most obvious trend is that mixtures with flyash consistently

Table 6.2. Measured magnetic susceptibility values (SI Units).

Mixture Reference	Coarse Aggregate Type	Coarse Aggregate Content	Fly Ash	Mean	Standard Deviation	Variation (%)
A	Limestone	Low	No	0.00171	0.00040	23
B	Limestone	Low	Yes	0.00950	0.00146	15
C	Basalt	Low	No	0.00331	0.00055	16
D	Basalt	Low	Yes	0.01006	0.00104	10
E	Basalt	High	No	0.00333	0.00028	8
F	Basalt	High	Yes	0.01007	0.00096	9

had greater magnetic susceptibilities than the corresponding mixtures without flyash. This was caused by the high ferrous-oxide content in the flyash.

FINITE-ELEMENT SIMULATIONS

Finite-element analyses were conducted to simulate the presence of concrete in a one-bar problem. The problem geometry, shown in Figure 6.1, was the same as the geometry considered in the Chapter 5 analyses with the following modifications: 1) the lower halfspace was assigned a magnetic susceptibility representative of concrete, 2) the upper halfspace was modeled as air, and 3) the coil wires were raised to the elevation of the centroids of the receivers to accommodate the addition of the concrete to the model.

Analyses were performed with concrete magnetic susceptibility values (χ_m) of 0.00001, 0.001, 0.01, 0.05, and 0.1. Measurements of **B** were simulated by performing an analysis with location V3 (Figure 6.1) assigned the properties of steel. Measurements of $\mathbf{B}_o$ were simulated by solving the problem with the bar and concrete assigned the magnetic properties of air ($\chi_m=3.7\text{x}10^{-7}$).

The magnetic distortions, **B"**, calculated from the simulated **B** and $\mathbf{B}_o$ values, are plotted across the receivers in Figure 6.2. For concrete magnetic susceptibility values less than 0.001, approximately the value obtained for the concrete mixture containing limestone coarse aggregates and no flyash, the concrete had little effect on the magnetic distortion. However, for concrete magnetic susceptibility values that exceeded 0.001, distortions caused by the concrete were equal to or greater than the distortions caused by just the bar. Consequently, magnetic distortions measured in this manner may contain systematic errors greater than 100 percent.

The reconstruction algorithm was able to accurately identify the location and size of the reinforcing bar when the magnetic susceptibility of the concrete was 0.00001.

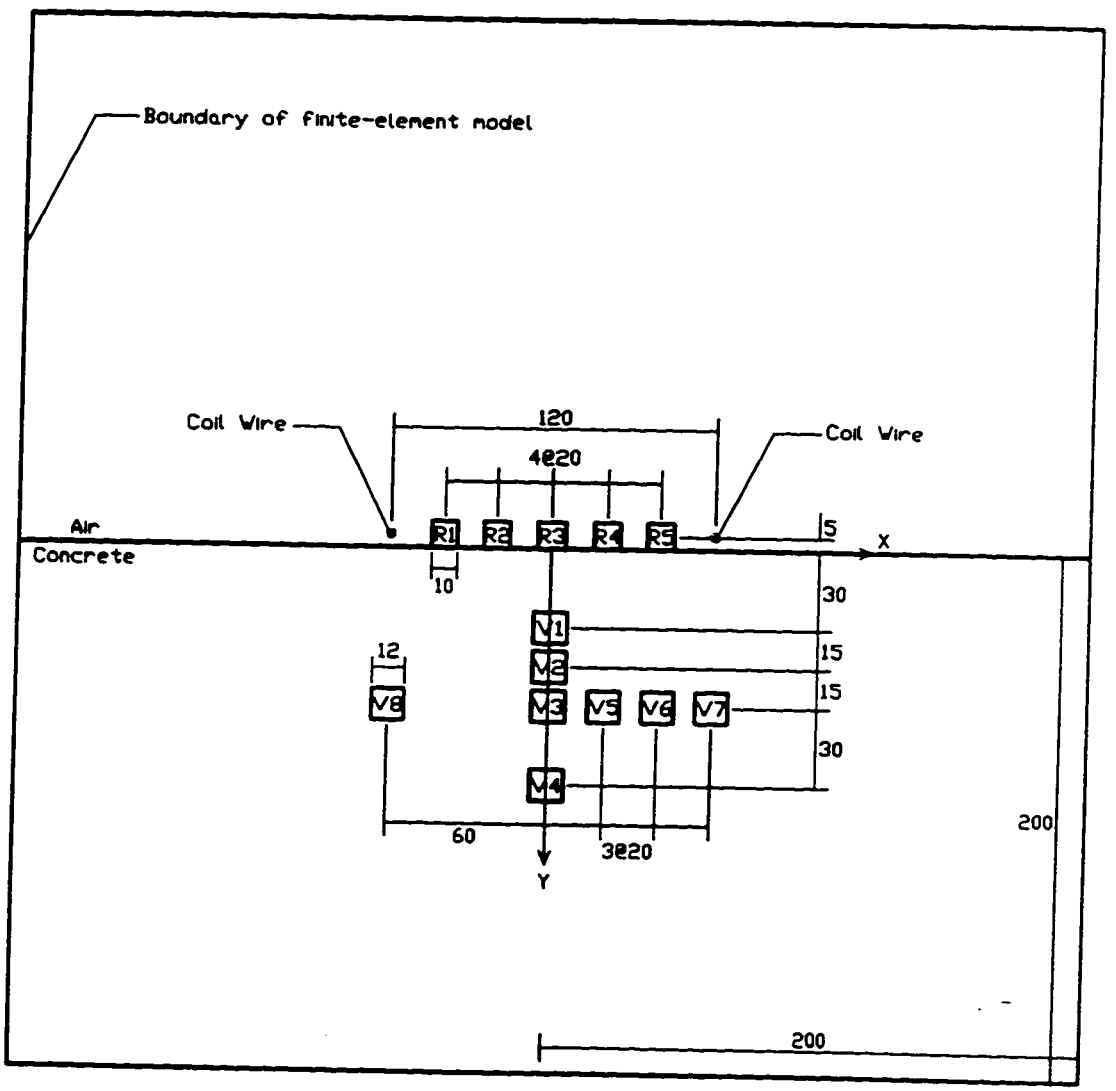

Fig. 6.1. Geometry of finite-element model with concrete (all units in millimeters).

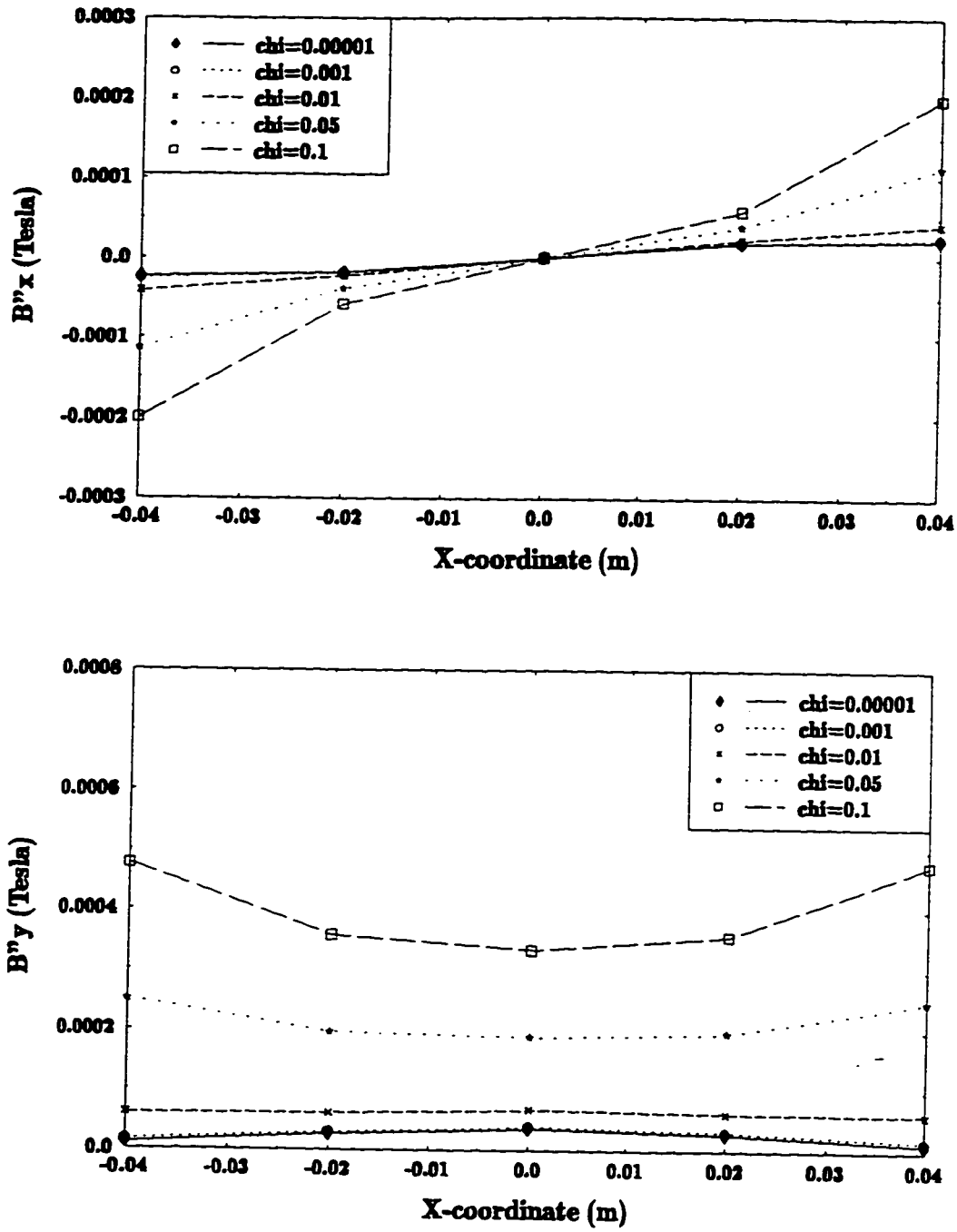

Fig. 6.2. Magnetic distortion across receivers ($\mathbf{B}_0$ measured in air).

However, for the lowest magnetic susceptibility obtained experimentally (0.001), the algorithm erred by 14 percent in the identification of the bar's location and 70 percent in the identification of the bar's area. Errors in the reconstructed geometry continued to increase with increasing magnetic susceptibility of the concrete. Since only the distortion caused by the steel provides information about the reinforcement configuration, it is necessary to compensate for the distortion caused by the concrete.

COMPENSATION METHODS

Four methods to compensate for the magnetic distortion caused by the concrete were identified. The reconstruction algorithm used in Chapter 5 was used to reconstruct the location and size of the bar from the distortions obtained from each method. Errors in bar depth and area from these reconstructions are plotted in Figure 6.3.

Method 1: One method to isolate the magnetic distortions caused by the steel is to measure $\mathbf{B}_o$ in the presence of a specimen made from the same concrete as the member. This procedure was simulated to obtain the magnetic distortions presented in Figure 6.4. These data demonstrate that the distortions caused by the concrete are effectively removed from the measured distortions by measuring $\mathbf{B}_o$ in the presence of concrete. This method may be practical for newly constructed facilities. However, it would be less feasible for investigations of aging structures.

When this method was implemented in the reconstruction algorithm, the location and size of the bar were identified accurately. The data in Figure 6.3 show that the location of the bar was identified within one percent and the area of the bar was identified within 10 percent for all values of magnetic susceptibility. These errors are comparable to the errors obtained when the concrete was modeled as free space (Chapter 5).

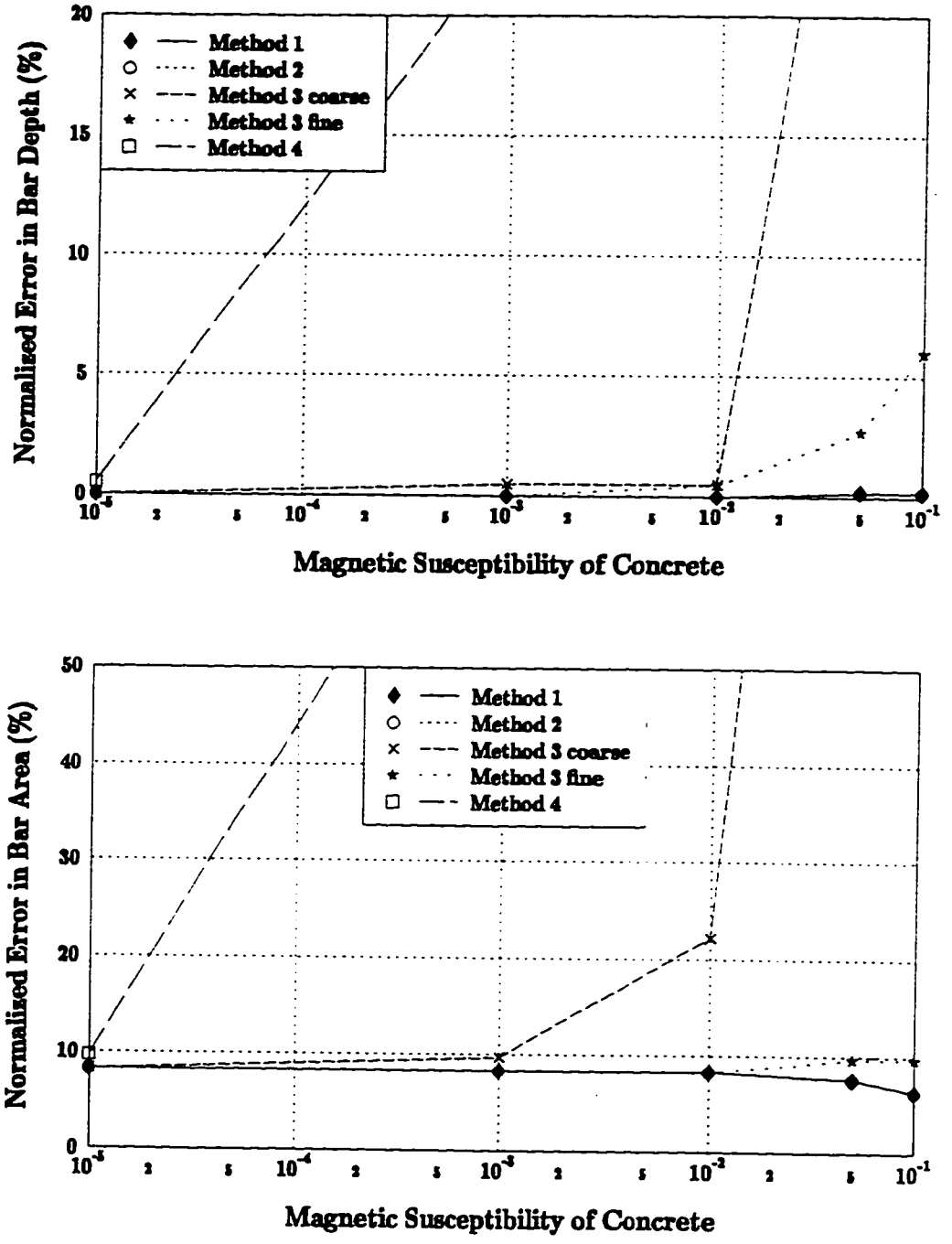

Figure 6.3. Errors in reconstruction results.

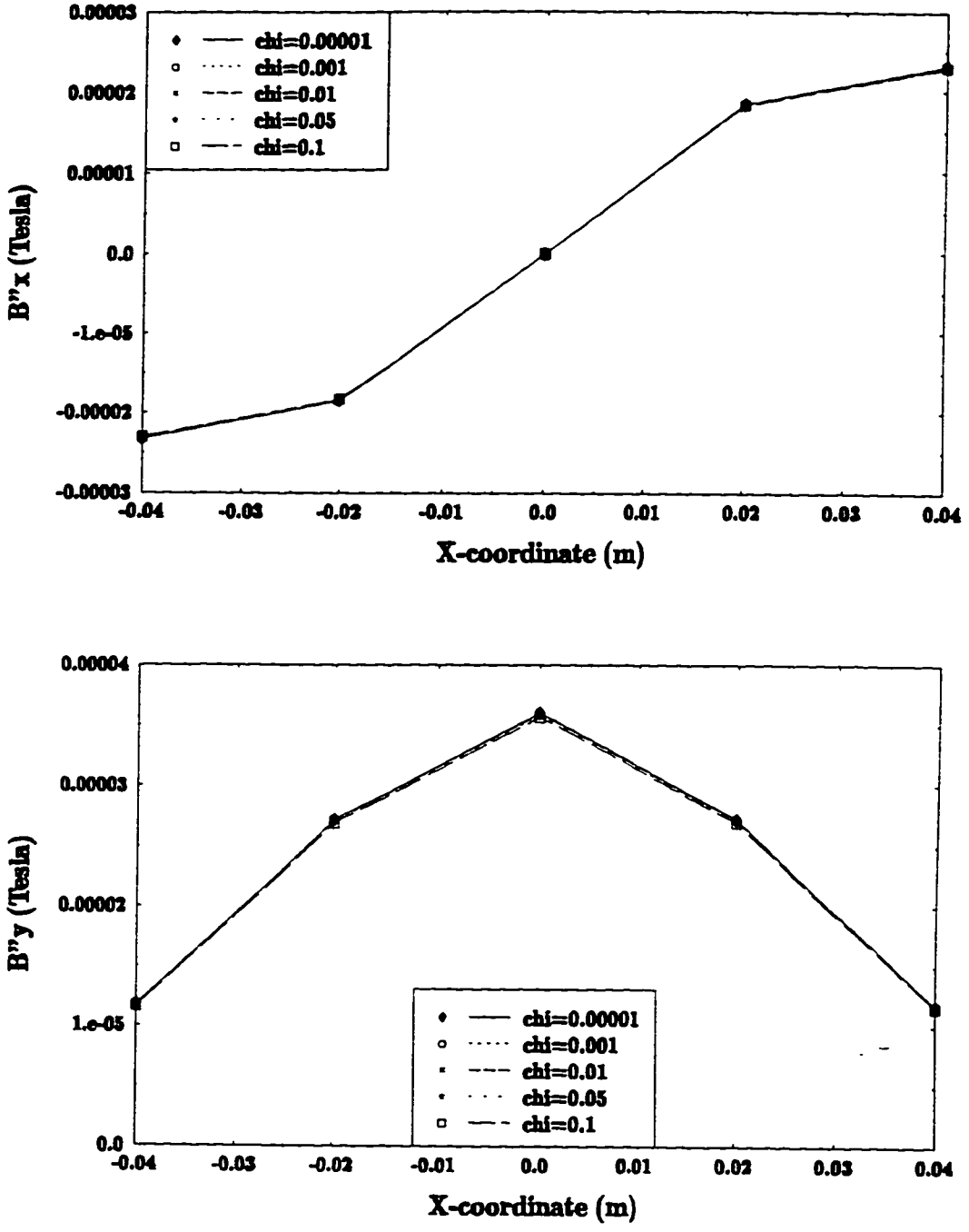

Figure 6.4. Magnetic distortion across receivers ($\mathbf{B}_o$ with concrete effects).

Method 2: The second compensation method is to measure the magnetic susceptibility of the concrete and compute the distortion caused by the concrete with a finite-element analysis. This is the method used to obtain the magnetic distortions shown in Figure 6.4. This method would be applicable to an investigation of any structure. The time required to perform the analysis with enough refinement to model the influence of the concrete may be a drawback to this method. Reconstruction results for this method are the same as the results from Method 1.

Method 3: Another compensation method is to measure the magnetic susceptibility of the concrete and use Equations 4.1 and 4.2 to calculate the magnetic distortion caused by the concrete. In this method, it is assumed that magnetization at one location in the concrete does not influence the magnetic field at another location in the concrete. This assumption allows $\mathbf{B}''$ in Equation 4.1 to be assigned a value of zero. Then, the magnetic dipole formula (Equation 4.2) can be used to relate the magnetic field generated by the coil ($\mathbf{B}_o$) at discretized volume elements in the concrete to the magnetic distortion at the receivers. Summing the distortions caused by each volume element provides an estimate of the magnetic distortion caused by the concrete. The magnetic distortion caused by the steel, $\mathbf{B}''_{steel}$, can then be calculated with the following equation:

$$\mathbf{B}''_{steel} = \mathbf{B} - \mathbf{B}_o - \Sigma \mathbf{B}''_{VE} \tag{6.1}$$

where $\mathbf{B}''_{VE}$ is the magnetic distortion caused by a single volume element of concrete.

This method is generally applicable and not computationally intensive. The method was implemented with two levels of refinement. A coarse discretization of the concrete member used square volume elements with 100 mm^2 areas and a fine discretization used square volume elements with areas of 25 mm^2. Figure 6.3 shows that the results from the coarse discretization were accurate for magnetic susceptibilities of

0.01 and less. This range of magnetic susceptibility values is representative of the range of values measured experimentally. The fine discretization yielded accurate results for all five values of magnetic susceptibility.

Method 4: The fourth compensation method is similar to Method 3. In this method it is assumed that magnetization at one volume element in the concrete distorts the magnetic field at a second volume element, and vice-versa. These distortions are computed by substituting the magnetic dipole formula, applied between the volume elements of concrete, into **B"** in Equation 4.1. This substitution results in a system of equations that can be solved simultaneously to compute the magnetic dipole density, **M**, at all of the volume elements. The magnetic distortion at the receivers, caused by the concrete, is calculated by applying the magnetic dipole formula between the volume elements of concrete and the receivers. The magnetic distortion caused by the steel is then calculated with Equation 6.1.

Applicability of this method is limited, because it is computationally intensive. The system of equations needed to apply the magnetic dipole equation between volume elements has two unknowns for every volume element. Storing the matrices used in solving this system of equations is impractical for refined discretization of the concrete member. Square volume elements with areas of 100 mm^2 was the finest discretization studied. This is equivalent to the coarse discretization for Method 3. The data plotted in Figure 6.3 show that when a coarse level of refinement was used this method did not adequately estimate the magnetic distortions caused by the concrete.

There are two possible explanations for this method's ineffectiveness. The volume elements may have been to large to satisfy the assumption that the magnetic field is uniform over the cross-section of the volume element. This assumption was used in the derivation of Equation 4.1. Another possibility is that adjacent volume elements violate

the assumption that the volume elements are far apart. This assumption was used to derive Equation 4.2, the magnetic dipole formula (Bleaney and Bleaney 1965).

SUMMARY

Magnetic susceptibility measurements were conducted on a variety of concrete mixtures. Based on the measurements, finite-element analyses were performed to simulate the magnetic distortions caused by both the concrete and by a steel reinforcing bar. It was found that some concretes could produce magnetic distortions comparable to those caused by the steel. Four methods of compensating for the magnetic distortion caused by the concrete were investigated analytically. One compensation method (Method 3) was identified as being computationally inexpensive, effective, and practical. This method used magnetostatic relationships between magnetization of volume elements in the concrete and magnetic distortion at the receivers to estimate the distortion caused by the concrete. The method neglects interaction of magnetization and magnetic field among the concrete volume elements.

Chapter 7

DYNAMIC RESPONSE ALGORITHM TO IDENTIFY PROPERTIES OF CONCRETE MEMBERS

Another area of nondestructive evaluation that could benefit from a less restrictive, more computationally intense solution strategy is the use of stress wave propagation to identify material properties and structural geometry. This chapter presents an algorithm to determine the properties of a concrete member by comparing experimentally measured dynamic response histories with simulated dynamic response histories. An overview of the algorithm is presented first. Then, a finite-difference scheme to model the dynamic response of a pavement system is developed and verified.

OVERVIEW OF ALGORITHM

The proposed algorithm identifies the properties of a concrete member by minimizing the sum of squared differences between measured and simulated acceleration time histories recorded during the dynamic response of the system. The reconstruction procedure consists of the following steps:

1) An impact of known magnitude and duration is applied to the surface of a concrete member. The resulting dynamic response of the system is recorded with two or more receivers (accelerometers) as shown in Figure 3.1.

2) For trial material properties and system geometry, acceleration histories at the locations of the receivers are computed by simulating the dynamic response with a finite-difference model.

3) The sum of squared differences (SSD) is computed for all of the receivers:

$$SSD = (\mathbf{A}_{meas} - \mathbf{A}_{calc})^T (\mathbf{A}_{meas} - \mathbf{A}_{calc}) \qquad (7.1)$$

where $\mathbf{A}_{meas}$ is a vector containing the measured acceleration response histories for all the receivers, and $\mathbf{A}_{calc}$ is a vector containing the calculated acceleration response histories.

4) New material properties and geometric attributes are selected, and Steps 2 and 3 are repeated until SSD is minimized. This minimization results in identification of the material properties and geometry of a system that has a dynamic response most similar to the physical system.

FINITE-DIFFERENCE SIMULATION MODEL

The finite-difference model developed for this research was similar to the models used by Alterman and Karal (1968), and Kelly et al. (1976). The model simulates stress

wave propagation in solids by discretizing the equations of motion and applying appropriate boundary conditions.

Axisymmetric Equations of Motion

The finite-difference model was based on discretization of the equations of motion for axisymmetric conditions:

$$\frac{\partial \sigma_{rr}}{\partial r} + \frac{\partial \tau_{rz}}{\partial z} + \frac{\sigma_{rr} - \sigma_{\theta\theta}}{r} = \rho \frac{\partial^2 u}{\partial t^2} \tag{7.2}$$

and

$$\frac{\partial \tau_{rz}}{\partial r} + \frac{\partial \sigma_{zz}}{\partial z} + \frac{\tau_{rz}}{r} = \rho \frac{\partial^2 w}{\partial t^2} \tag{7.3}$$

where r and z are the axes of the cylindrical coordinate system, σ_{rr}, $\sigma_{\theta\theta}$, σ_{zz}, and τ_{rz} are the components of the stress tensor, ρ is density, t is time, and u and w are the r- and z-components of displacement.

The stress tensor, σ, at any point in a body may be expressed as the sum of the mean stress, σ_m, and the deviator stress, σ', as follows (Boresi and Chong 1987):

$$\sigma = \sigma' + \sigma_m \tag{7.4}$$

Viscous damping was included in the deviator stress to model the material damping of the concrete. The viscoelastic model applied to the deviator stress is shown

schematically in Figure 7.1. Damping was not included in the mean stress, because most materials behave independently of the mean stress (Malvern 1969).

The viscoelastic model is described by the following constitutive relationships:

$$\sigma_m = (3\lambda + 2G)\varepsilon_m \tag{7.5}$$

and

$$\sigma' = 2G\varepsilon' + 2\eta \frac{\partial}{\partial t}(\varepsilon') \tag{7.6}$$

where λ and G are the Lame' parameters, ε_m is the mean strain, η is the viscous damping parameter, and ε' is the deviator strain.

Substituting Equations 7.5 and 7.6 into Equation 7.4 and expanding yields the constitutive relationships between components of the stress and strain tensors:

$$\sigma_{rr} = \lambda(\varepsilon_{rr} + \varepsilon_{\theta\theta} + \varepsilon_{zz}) + 2G\varepsilon_{rr} + \frac{2}{3}\eta\frac{\partial}{\partial t}(2\varepsilon_{rr} - \varepsilon_{\theta\theta} - \varepsilon_{zz}) \tag{7.7}$$

$$\sigma_{\theta\theta} = \lambda(\varepsilon_{rr} + \varepsilon_{\theta\theta} + \varepsilon_{zz}) + 2G\varepsilon_{\theta\theta} + \frac{2}{3}\eta\frac{\partial}{\partial t}(2\varepsilon_{\theta\theta} - \varepsilon_{rr} - \varepsilon_{zz}) \tag{7.8}$$

$$\sigma_{zz} = \lambda(\varepsilon_{rr} + \varepsilon_{\theta\theta} + \varepsilon_{zz}) + 2G\varepsilon_{zz} + \frac{2}{3}\eta\frac{\partial}{\partial t}(2\varepsilon_{zz} - \varepsilon_{rr} - \varepsilon_{\theta\theta}) \tag{7.9}$$

$$\tau_{rz} = 2G\varepsilon_{rz} + 2\eta\frac{\partial}{\partial t}(\varepsilon_{rz}) \tag{7.10}$$

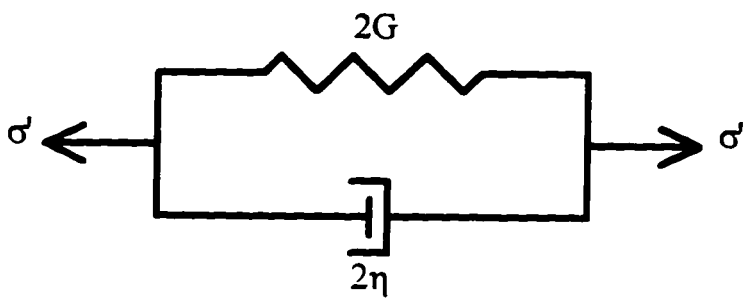

Figure 7.1. Viscoelastic model applied to deviator stress.

Only small strains are expected to occur during the dynamic response. Therefore, the components of the strain tensor may be expressed as follows:

$$\varepsilon_{rr} = \frac{\partial u}{\partial r} \tag{7.11}$$

$$\varepsilon_{\theta\theta} = \frac{u}{r} \tag{7.12}$$

$$\varepsilon_{zz} = \frac{\partial w}{\partial z} \tag{7.13}$$

$$\varepsilon_{rz} = \frac{1}{2}\left(\frac{\partial u}{\partial z} + \frac{\partial w}{\partial r}\right) \tag{7.14}$$

Substituting Equations 7.11-7.14 into Equations 7.7-7.10 and substituting the results into Equations 7.2 and 7.3 allows the equations of motion to be written as follows:

$$\begin{aligned}\rho\frac{\partial^2 u}{\partial t^2} &= (\lambda+2G)\frac{\partial^2 u}{\partial r^2} + \frac{(\lambda+2G)}{r}\frac{\partial u}{\partial r} + (\lambda+G)\frac{\partial^2 w}{\partial r\partial z} + G\frac{\partial^2 u}{\partial z^2} - \frac{2Gu}{r^2} \\ &+\eta\frac{\partial}{\partial t}\left(\frac{4}{3}\frac{\partial^2 u}{\partial r^2} + \frac{4}{3r}\frac{\partial u}{\partial r} + \frac{1}{3}\frac{\partial^2 w}{\partial r\partial z} + \frac{\partial^2 u}{\partial z^2} - \frac{2u}{r}\right)\end{aligned} \tag{7.15}$$

$$\begin{aligned}\rho\frac{\partial^2 w}{\partial t^2} &= (\lambda+2G)\frac{\partial^2 w}{\partial z^2} + \frac{(\lambda+G)}{r}\frac{\partial u}{\partial z} + (\lambda+G)\frac{\partial^2 u}{\partial r\partial z} + G\frac{\partial^2 w}{\partial r^2} + \frac{G}{r}\frac{\partial w}{\partial r} \\ &+\eta\frac{\partial}{\partial t}\left(\frac{4}{3}\frac{\partial^2 w}{\partial z^2} + \frac{1}{3r}\frac{\partial u}{\partial z} + \frac{1}{3}\frac{\partial^2 u}{\partial r\partial z} + \frac{\partial^2 w}{\partial r^2} + \frac{1}{r}\frac{\partial w}{\partial r}\right)\end{aligned} \tag{7.16}$$

Equations 7.15 and 7.16 reduce to Equations 3.9 and 3.10 when η is equal to zero.

Results of discretizing the equations of motion and solving for displacements are presented in Appendix A. In the equations presented in Appendix A, u and w are calculated for the l+1 time step, at a grid point located at $m\Delta r$ in the horizontal direction and $n\Delta z$ in the vertical direction. These calculations are performed with known displacements from previous time steps at the grid point being evaluated and the eight adjacent grid points. This is shown in the form of a stencil in Figure 7.2. One-sided differences were used for time derivatives since displacements at time step l+1 were unknown at five of the relevant grid points.

Boundary Conditions

The geometry of the pavement system modeled with finite differences is shown in Figure 7.3; Figure 7.4 shows a representation of the mesh used in the model. Along the symmetry line, the horizontal displacements are zero. Therefore, no calculations were required to obtain the horizontal displacements for grid points on the symmetry line. Another condition of symmetry is that symmetric points adjacent to the symmetry line will have equal and opposite horizontal displacements and identical vertical displacements. These conditions were used to simplify the equations in Appendix A when solving for vertical displacements on the symmetry line.

Using the equations in Appendix A to calculate the displacements at grid points on the surface of the body requires a row of imaginary grid points outside the body (Figure 7.4). Displacements at these imaginary grid points are determined by applying the appropriate boundary conditions to the model.

At the top free surface, σ_{zz} and τ_{rz} must be zero, except at the point where the load is applied. To enforce these conditions, displacements at the imaginary grid points were calculated using Equations 7.9 and 7.10 (expressed with displacements) with the

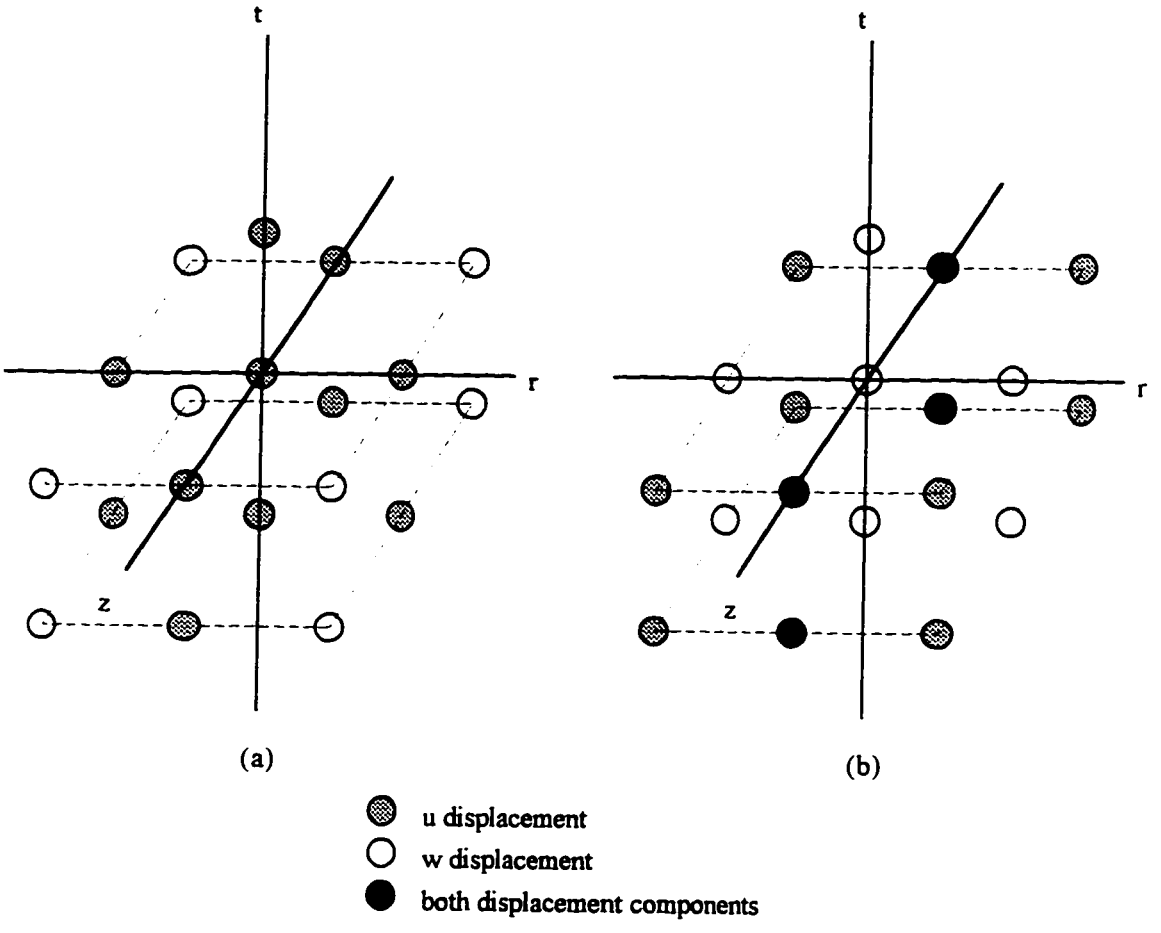

Figure 7.2. Calculation stencils for the displacement components in the viscoelastic model: (a) grid points used in calculating u and (b) grid points used in calculating w.

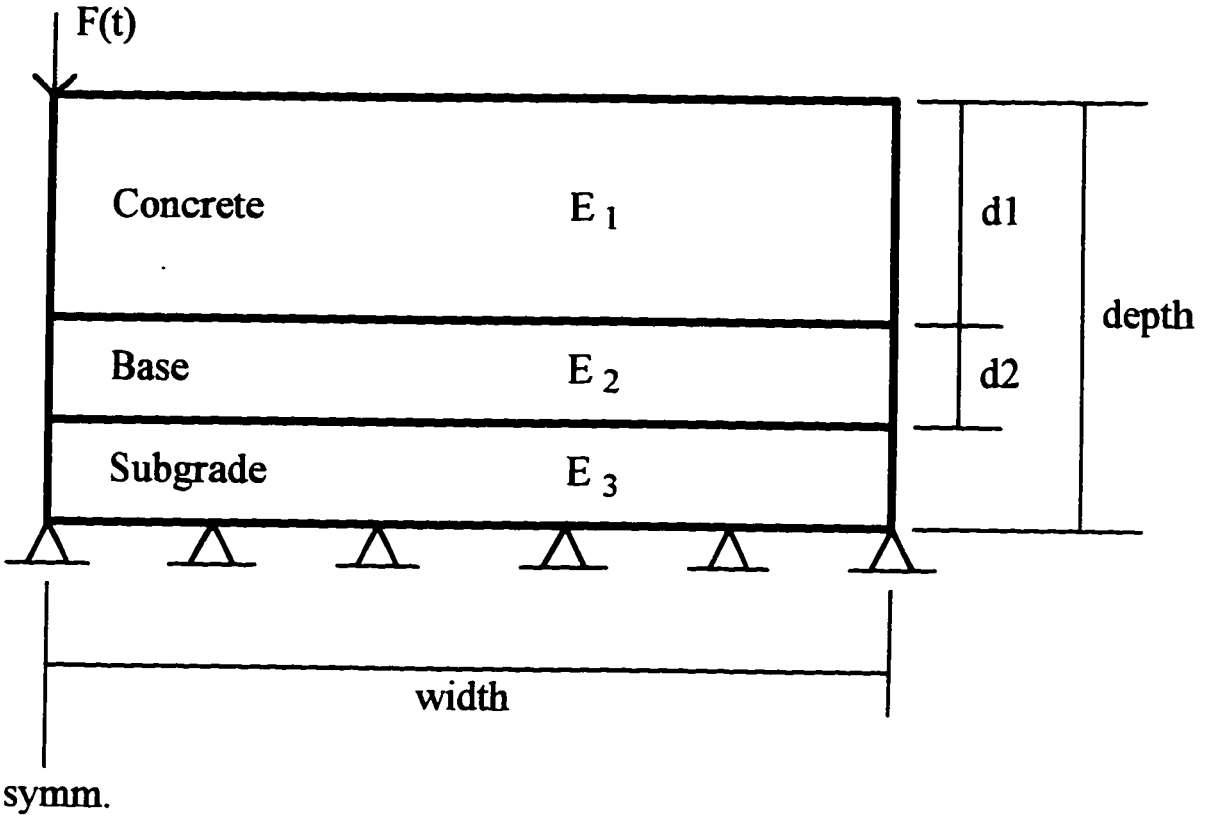

Figure 7.3. Geometry of finite-difference model.

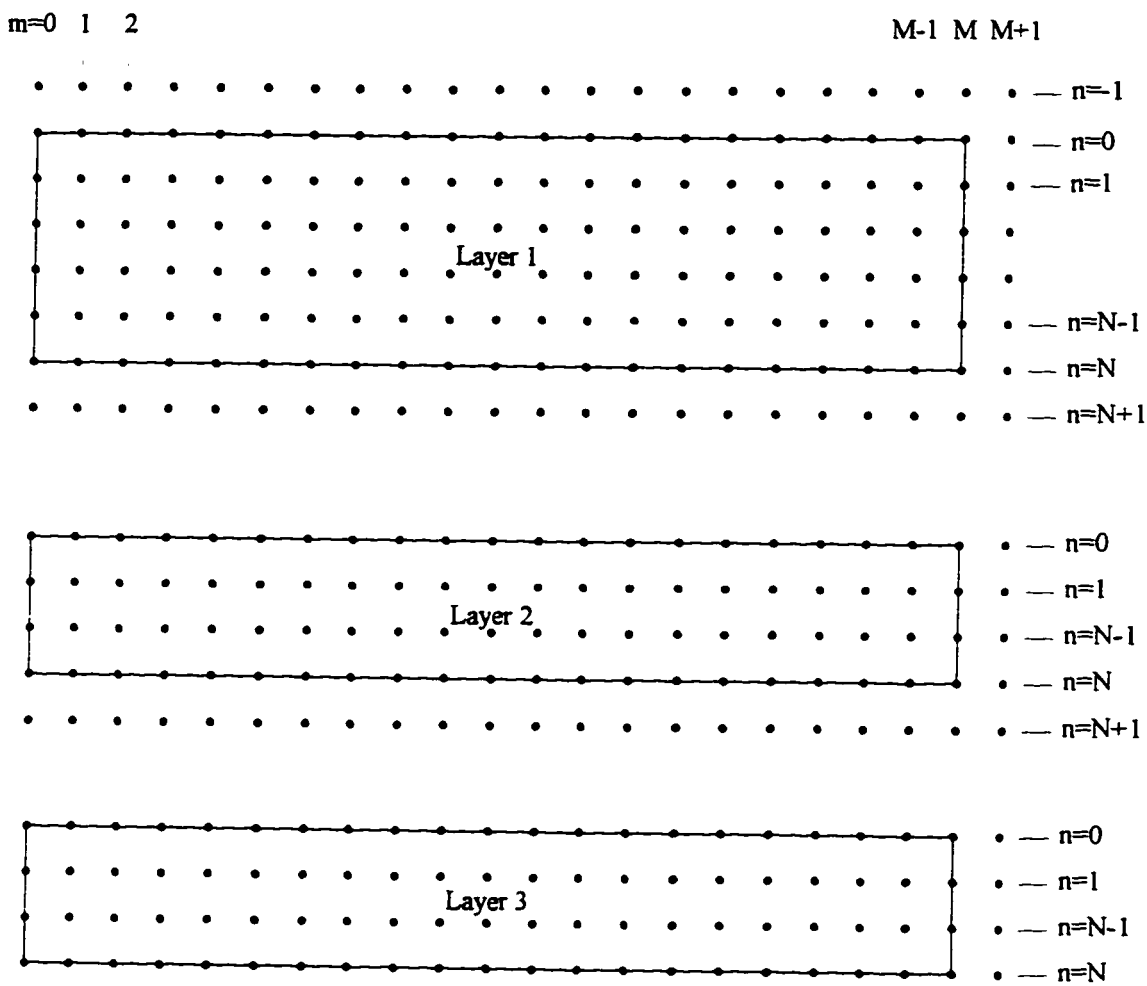

Figure 7.4. Finite-difference mesh.

stresses set equal to zero. The applied stress was used for σ_{zz} at the point of load application. Similarly, along the right-hand side of the model, σ_{rr} and τ_{rz} must be zero.

All grid points along the bottom of the model were assigned displacements of zero, effectively fixing the bottom surface. It will be shown in the parametric study (Chapter 8) that fixing the bottom surface had little influence on the results during the portion of the response that is of interest.

Two conditions must be satisfied at the interface between two layers, continuity of displacements and equilibrium. Continuity of displacements was achieved by assigning the displacements at the lower surface of the upper layer (n=N) to the top surface of the lower layer (n=0). This assignment provides the displacements at the boundary of the lower layer, so a row of imaginary grid points above the interface was not needed. However, knowledge of the displacements for the grid points at the bottom surface of the upper layer did require an imaginary row of grid points below the interface. Displacements at these imaginary grid points are calculated by setting σ_{zz} and τ_{rz} (Equations 7.9 and 7.10) at the bottom of the upper layer (n=N) equal to the stresses at the top of the lower layer (n=0). This stress equality satisfies equilibrium at the interface between layers. In the lower layer, derivatives in the z-direction were calculated using one-sided differences.

Displacements at grid points on intersecting lines of imaginary grid points were determined by extending the boundary conditions to one of the imaginary rows. For the upper right corner of the top layer, the conditions $\sigma_{zz}=0$ and $\tau_{rz}=0$ were extended to an imaginary row of grid points outside the right boundary of the model. Here, one-sided differences were used to calculate derivatives in the r-direction. For the lower right corners of the top two layers, the free surface was extended to the imaginary row of grid points and one-sided differences were used to calculate derivatives in the z-direction.

A stability condition, similar to that identified by Alterman and Lowenthal (Equation 3.15) was also applicable to the model developed here. The stability condition for the present model is approximately:

$$(\Delta t)^2(\lambda+2G)+4\eta\Delta t \le \rho h^2 \qquad (7.17)$$

where h is the lesser of Δr and Δz.

VERIFICATION OF FINITE-DIFFERENCE MODEL

Accuracy of the finite-difference model was verified by solving a sample problem and comparing the results with results obtained by ANSYS, a commercially available finite-element program (ANSYS 1992). The geometry of the sample problem is shown in Figure 7.5. A load was applied in a manner intended to simulate an impact. The force-time relationship was a half-sine with a peak of 800 N and a duration of 50 μs. Because the two solution methods apply damping in different manners, no damping was induced in the models used for comparison.

The finite-difference model used 142,128 grid points to represent the pavement system geometry (Figure 7.5). Grid points were spaced 1 mm apart horizontally and vertically. A time increment of 0.01 μs was used, and the load was updated at each time step.

In the finite-element model, 2500 eight-noded elements and 7701 nodes were used to describe the geometry of the problem. This mesh is presented in Figure 7.6. A time increment of 0.125 μs was used for calculating the displacements. However, the load was updated at 5 μs intervals. Updating the load at 5 μs intervals approximated the force-time curve with 10 linear segments.

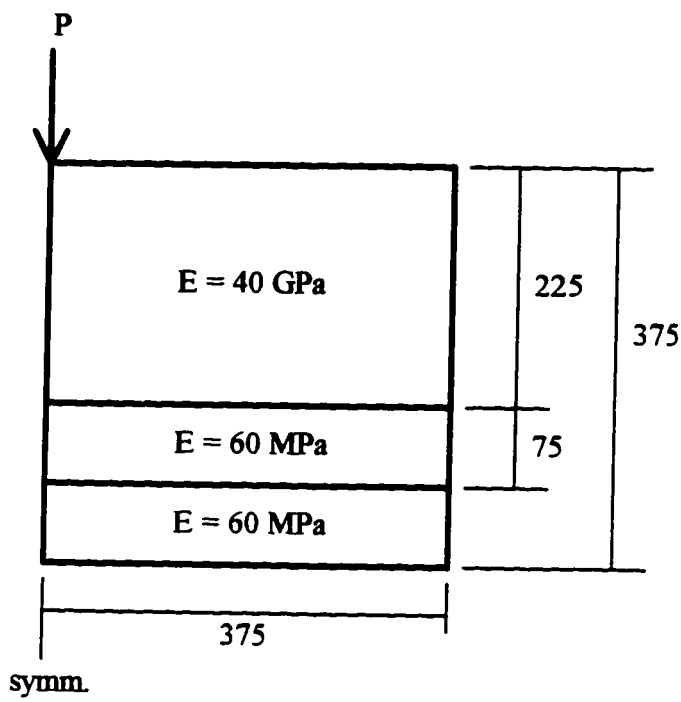

Figure 7.5. Sample problem geometry.

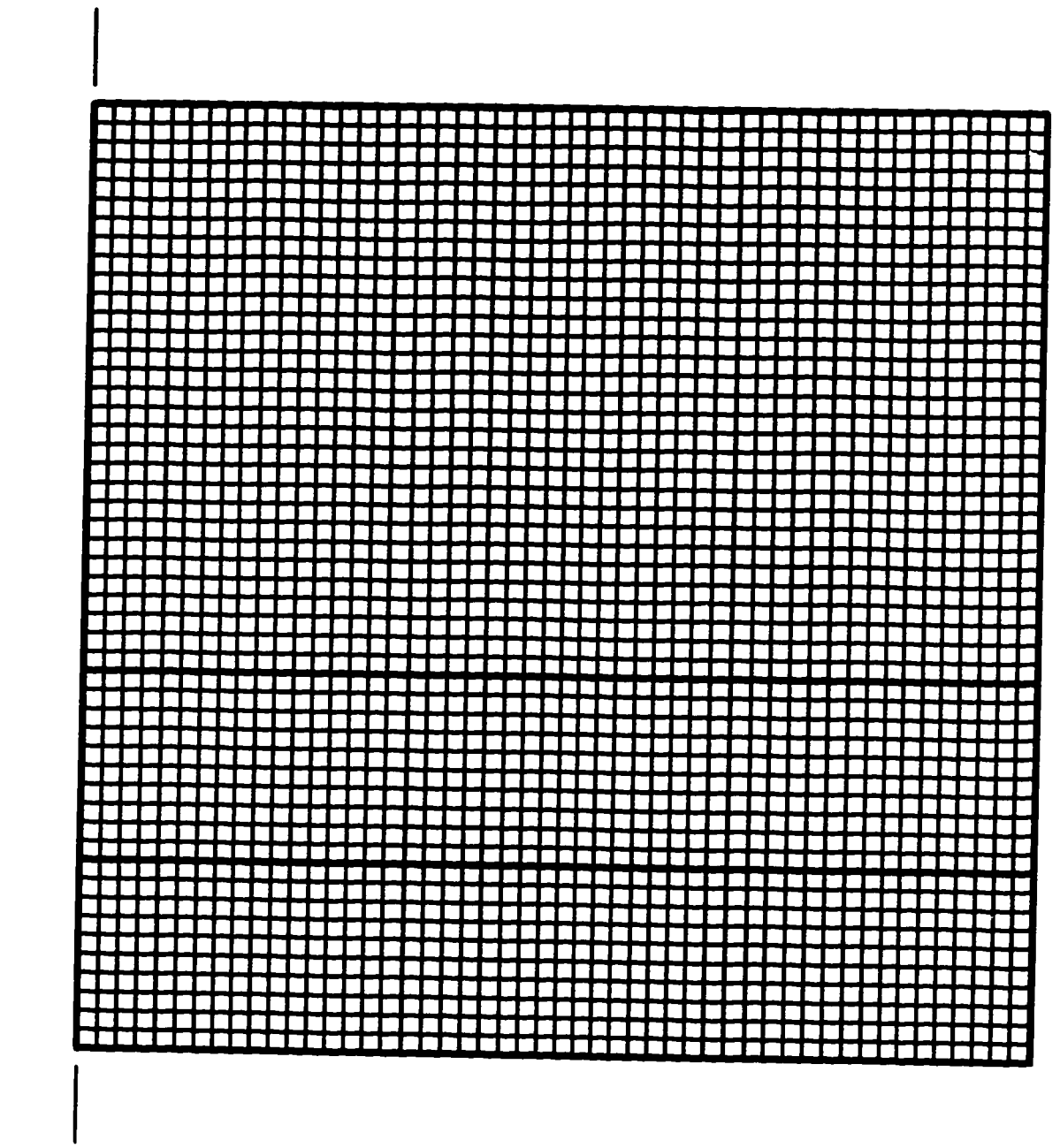

Figure 7.6. Finite-element mesh.

Displacement histories were recorded at a point on the surface, 150 mm from the load, for both models. The vertical displacement histories are shown in Figure 7.7. These results show that the finite-difference solution agrees well with the finite-element solution. Some minor differences occur at the peaks. However, the magnitudes and occurrence times of the displacements are essentially the same for both solutions.

Figure 7.7 also shows that both solutions have frequent occurrences of sharp curvature in the time histories. These sharp curvatures occur because no damping was included in the models. Including damping in either model would reduce the number of these sharp curvatures.

SUMMARY

An algorithm to determine the properties of a concrete member was presented. The algorithm compares measured and simulated dynamic responses of the system. This algorithm uses more information than is used by the impact-echo and SASW methods.

A finite-difference formulation, used to model the dynamic response of a pavement system, was developed and verified for a problem without damping. The finite-difference model appears to yield accurate and reliable results.

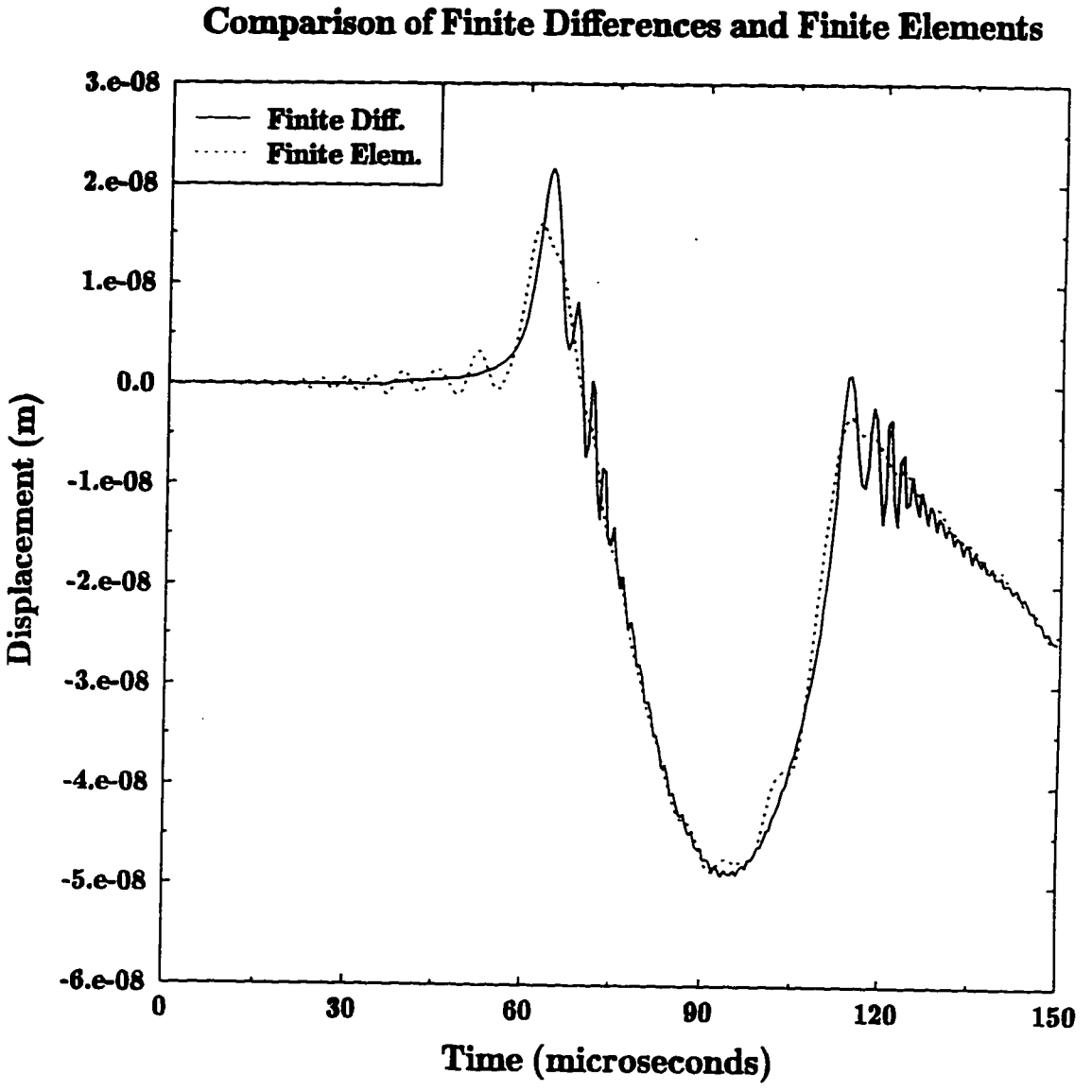

Fig. 7.7. Comparison of finite-difference solution and finite-element solution.

Chapter 8

PARAMETRIC STUDY OF VARIABLES INFLUENCING STRESS WAVE PROPAGATION

A parametric study was conducted to determine the influences of input variables used in the finite-difference simulations. These variables included the geometry and material properties of a layered system.

LAYERED SYSTEM WITHOUT CRACKS

A finite-difference program was developed to simulate the dynamic response of the three-layer system shown in Figure 8.1. Several parameters used to describe the model were varied in the parametric study. The variables studied were: Young's modulus of the top layer (E_1), thickness of the top layer (d_1), density of the top layer (ρ_1), Poisson's ratio of the top layer (ν_1), Young's modulus of the second layer (E_2), Young's modulus of the bottom layer (E_3), and the damping to shear modulus ratio (η/G) used for the system.

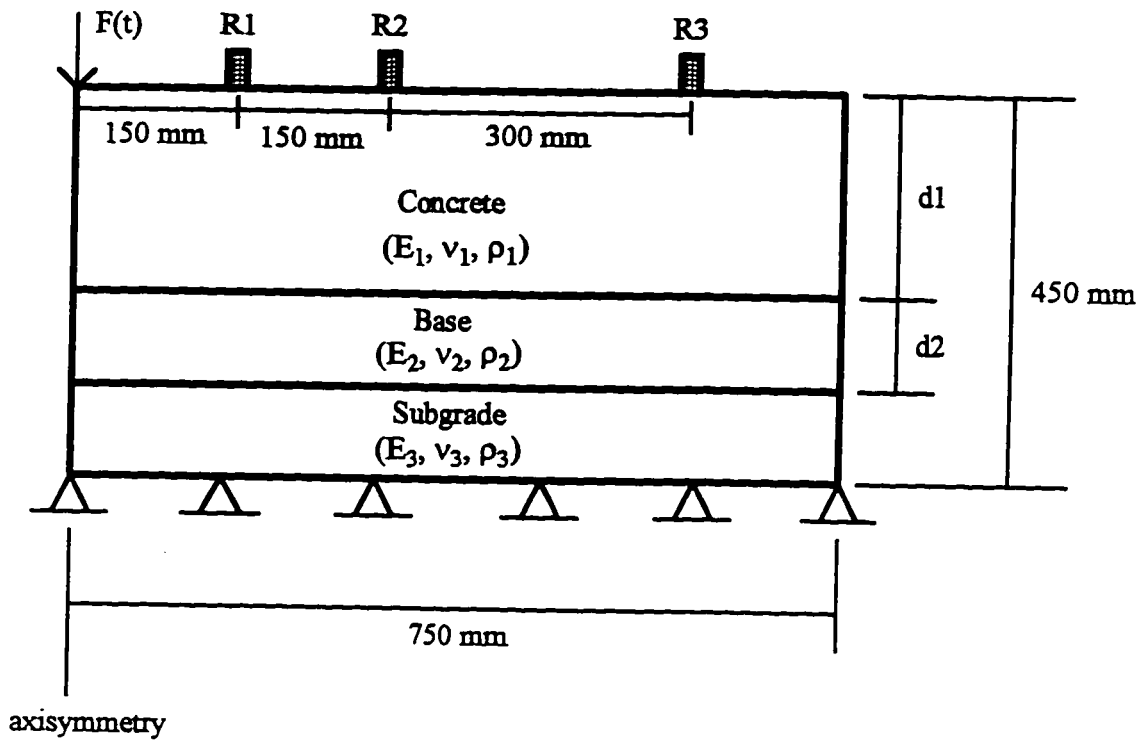

Figure 8.1. Geometry used for parametric study.

Acceleration response histories were calculated at locations representing three receivers. The first receiver (R1) was located on the top surface of the model, 150 mm from the applied load. The second receiver (R2) was located 300 mm from the applied load, and the third receiver (R3) was located 600 mm from the applied load. A measured impact (F(t)), plotted in Figure 8.2, was used as the applied load. The data in Figure 8.2 were recorded experimentally at a sampling rate of 2.0 μs, and the time step used in the finite-difference model was 0.2 μs. Therefore, values for the applied load at intermediate time steps were obtained by linear interpolation.

Reference Model

A reference model was assigned the intermediate values of each parameter being investigated. The influence of each variable was investigated by assigning that variable a higher and a lower value than the value used in the reference model, while keeping the other input parameters constant.

The top layer of the model was intended to represent a concrete slab. The properties of this layer in the reference model were: a Young's modulus of 40 GPa, a density of 2320 kg/m^3, a thickness of 200 mm, a Poisson's ratio of 0.20, and a damping to shear modulus ratio of 2.5×10^{-6} s. This value of the damping to shear modulus ratio was identified as a value that provided reasonably smooth response curves with minimal reduction of the magnitudes of the peaks in the responses.

The second layer represented a base course in a pavement system. Properties of the second layer were: a Young's modulus of 60 MPa, a density of 1900 kg/m^3, a thickness of 100 mm, a Poisson's ratio of 0.25, and a damping to shear modulus ratio of 2.5×10^{-6} s.

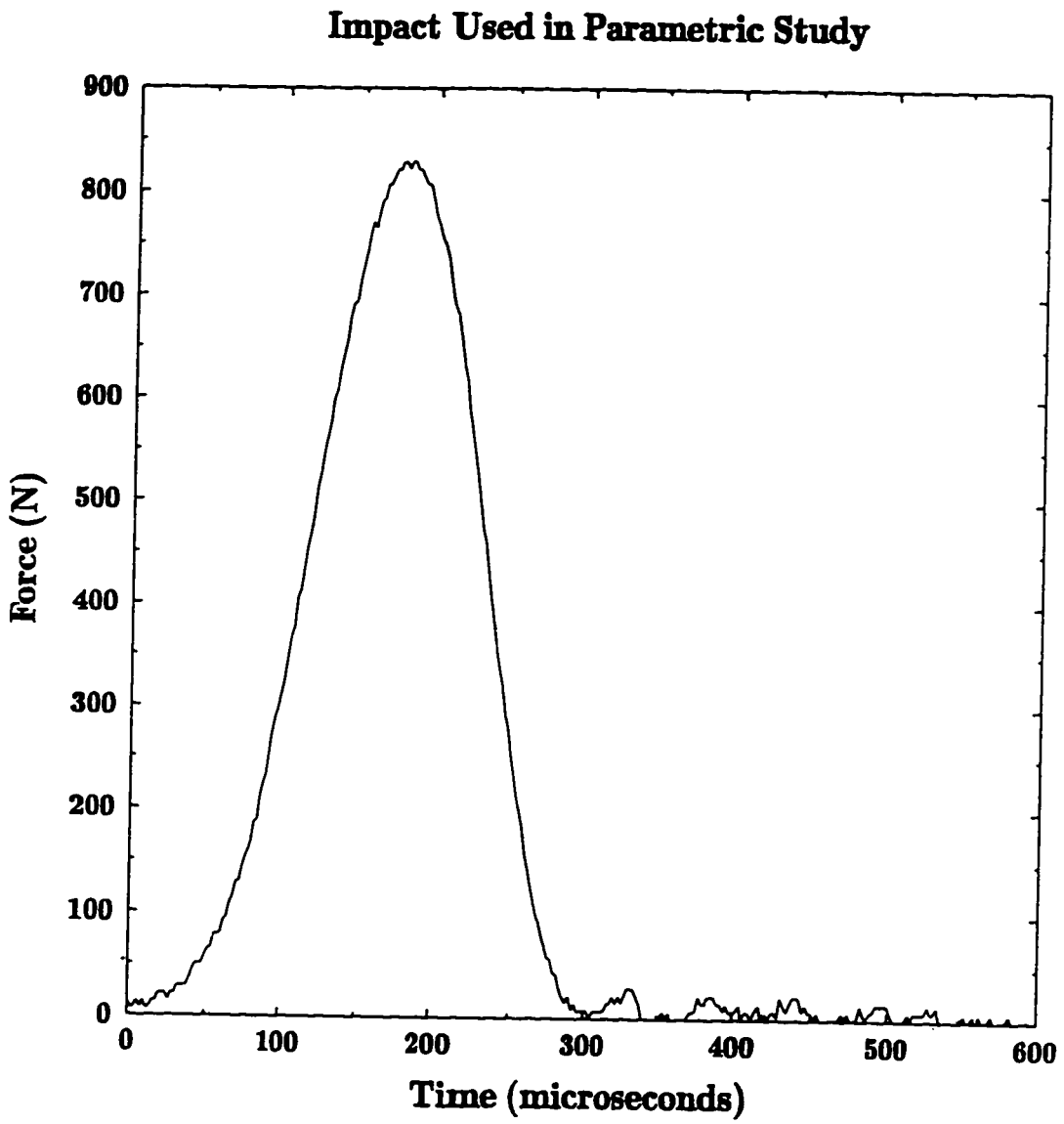

Figure 8.2. Experimental impact used as applied load in parametric study.

The third layer represented the subgrade in a pavement system. Density and Young's modulus of the third layer were the same as those of the second layer, but Poisson's ratio was increased to 0.30, and the thickness was 150 mm.

Properties of Top Layer

To investigate the influence of Young's modulus of the top layer, E_1, the layer was assigned values of 30 GPa, 40 GPa, and 50 GPa. These represent low, medium, and high Young's modulus values for concrete.

Response histories calculated at the three receivers are presented in Figure 8.3. These response histories show that variations in E_1 changed the response as soon as significant accelerations were observed at the receivers. Increasing E_1 decreased the peak values of the acceleration response histories and caused the major peaks to occur earlier in the responses. For the Poisson's ratio values used to describe the layers in the model, the surface wave velocity would be approximately 90 percent of the shear wave velocity expressed in Equation 3.14 (Nazarian 1984). Based on this relationship, it was expected that increasing E_1 would cause the peaks to occur earlier in the responses. Decreasing magnitudes of the peaks with increasing E_1 were also expected since the static response of a stiffer system would have smaller displacements. In a dynamic response, the reduced magnitudes of the displacements would cause reduced slopes (velocities) and curvatures (accelerations). These influences of E_1 on the dynamic response of the system are substantial and should allow the dynamic response algorithm to identify Young's modulus of the top layer.

The influence of the thickness of the top layer, d_1, was investigated by assigning the top layer thicknesses of 150 mm, 200 mm, and 250 mm. To keep the size of the

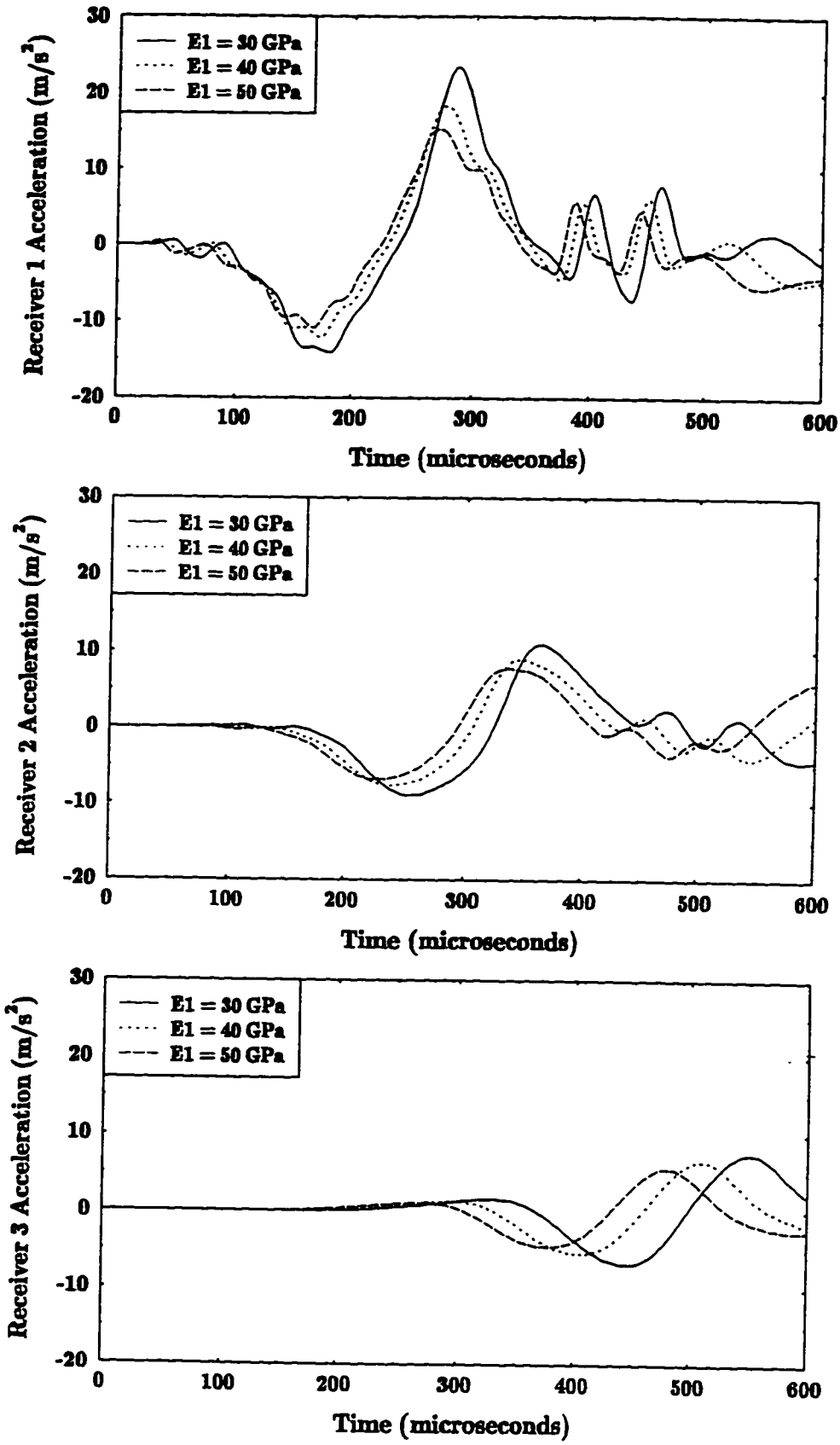

Figure 8.3. Effects of varying Young's modulus in the top layer.

model constant, the thicknesses of the subgrade layer were 200 mm, 150 mm, and 100 mm, respectively, in the three models.

Acceleration response histories for these three analyses are shown in Figure 8.4. Varying the thickness of the top layer produced changes in the response almost as early as changes caused by varying E_1. As with increases in E_1, increasing d_1 decreased the peak values of the acceleration response histories and caused the major peaks to occur earlier in the responses. Earlier occurrences of peaks in the responses was expected because a thicker slab provides more of the material in which waves propagate at higher velocities. High frequency (short wavelength) components of the surface wave propagate in the material near the surface, and lower frequency (long wavelength) components propagate in increasingly deep material (Nazarian 1984). Therefore, frequencies slowed by the base material under a thin slab would propagate at greater velocity because of the influence of the thick slab. Increases in peak magnitudes with decreasing slab thickness were also expected because of the reduced flexural and shear stiffnesses of the slab. The changes in the magnitudes of the peaks and magnitudes of the phase shifts caused by varying d_1 are greater than the changes produced by varying E_1. Consequently, the dynamic response algorithm should also be able to identify the thickness of the top layer.

Effects of density of the top layer, ρ_1, were investigated by analyzing models with top layer densities of 2240 kg/m^3, 2320 kg/m^3, and 2400 kg/m^3. These values represent low, medium, and high densities that would be expected in normal weight concrete.

Results from these analyses are plotted in Figure 8.5. Varying ρ_1 caused small changes in the responses at all receivers from the time that significant accelerations began to occur. Increasing ρ_1 caused the major peaks to occur slightly later in the responses, with little change in the magnitudes of the peak accelerations. This observation was

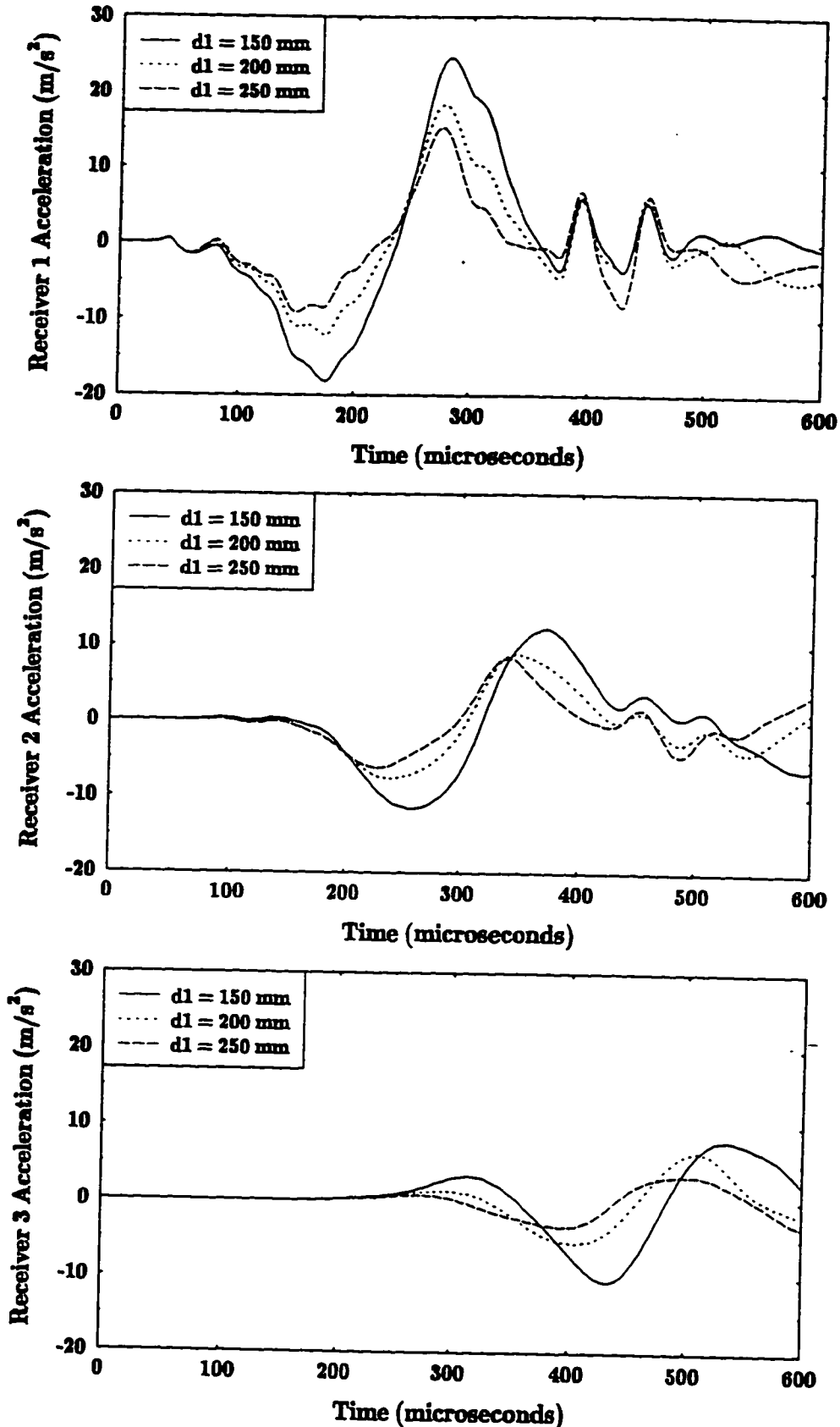

Figure 8.4. Effects of varying the thickness of the top layer.

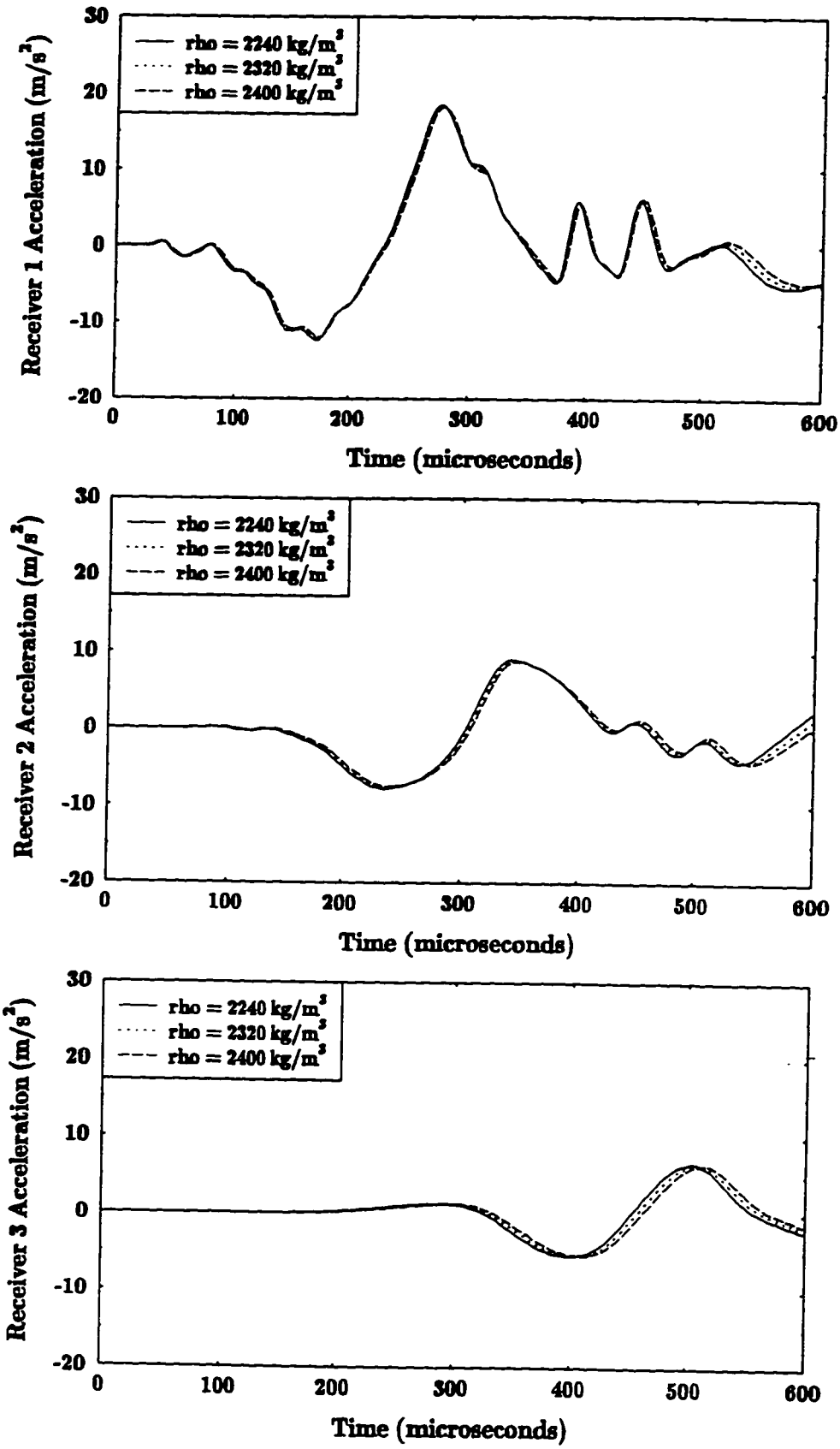

Figure 8.5. Effects of varying density in the top layer.

expected because of the proportionality of the surface wave velocity and the shear wave velocity (Equation 3.14).

An investigation of the influence of Poisson's ratio of the top layer, ν_1, was conducted by assigning the top layer Poisson's ratio values of 0.15, 0.20, and 0.25. This range of values is representative of the range that would be exhibited by concrete.

Plots of the response histories obtained from these three analyses are provided in Figure 8.6. The influence of Poisson's ratio was most apparent at peaks in the response histories and near the end of the response history of the first receiver. Slight differences were observed throughout the responses at the receivers. However, the trends in the differences were not consistent as was observed for the other slab properties. Changes caused by varying ν_1 were no more substantial than the differences caused by varying density, ρ_1.

Properties of Lower Layers

Effects of varying the Young's modulus of the second layer, E_2, were investigated for values of 6 MPa, 60 MPa, and 600 MPa. Results are shown in Figure 8.7. Increasing Young's modulus of the second layer reduced the magnitudes of first negative peak at each receiver and at various other portions of the response histories. Varying E_2 did not appear to cause any significant phase shifts in the response histories. The magnitudes of the changes caused by E_2 are comparable to the changes caused by varying ρ_1 and ν_1. Since order of magnitude changes in E_2 were needed to cause these effects, it will be difficult for the dynamic response algorithm to identify the stiffness of the second layer accurately.

The influence of the stiffness of the bottom layer, E_3, was investigated in a similar manner. Again, Young's modulus values of 6 MPa, 60 MPa, and 600 MPa were used.

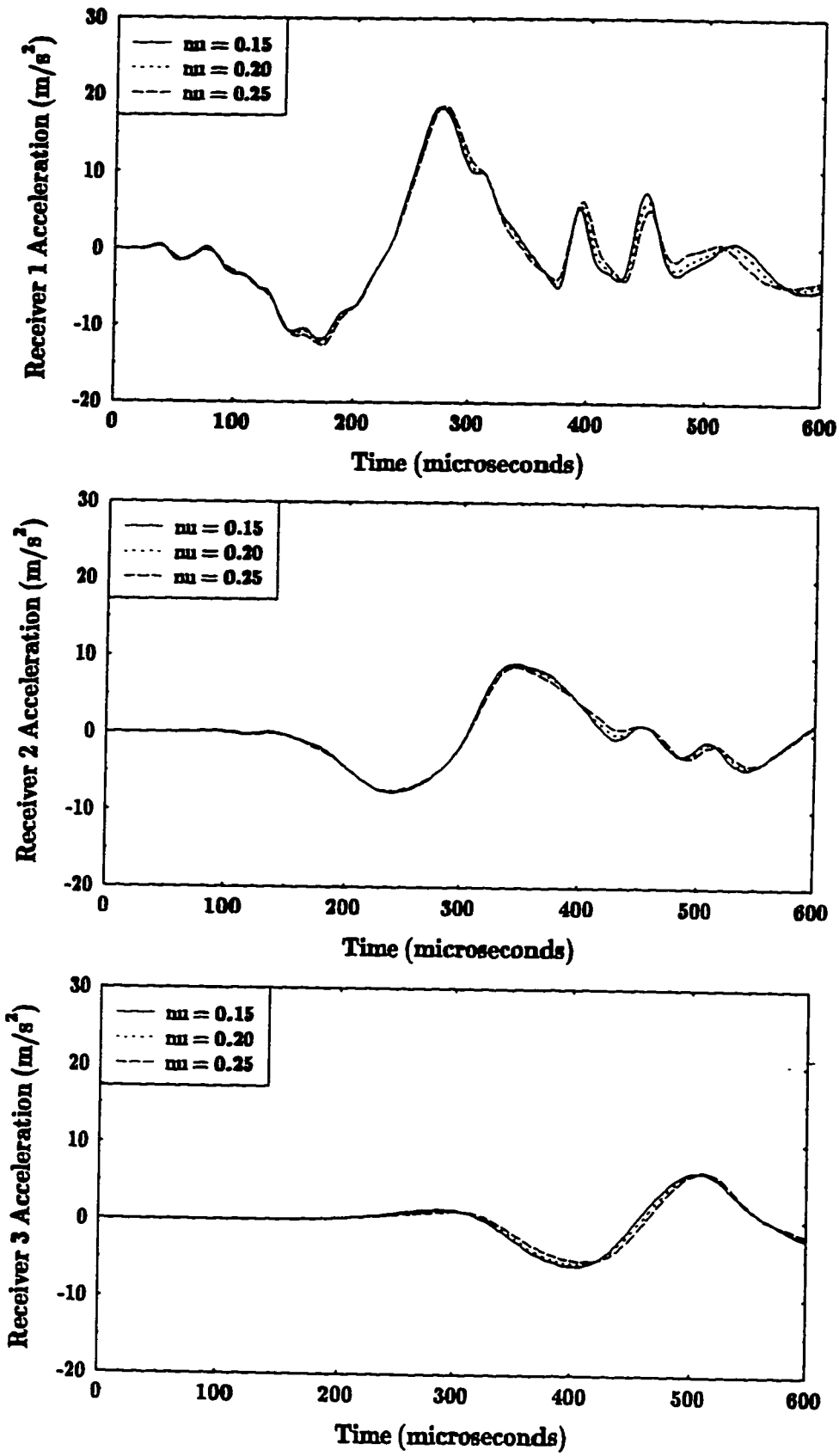

Figure 8.6. Effects of varying Poisson's ratio in the top layer.

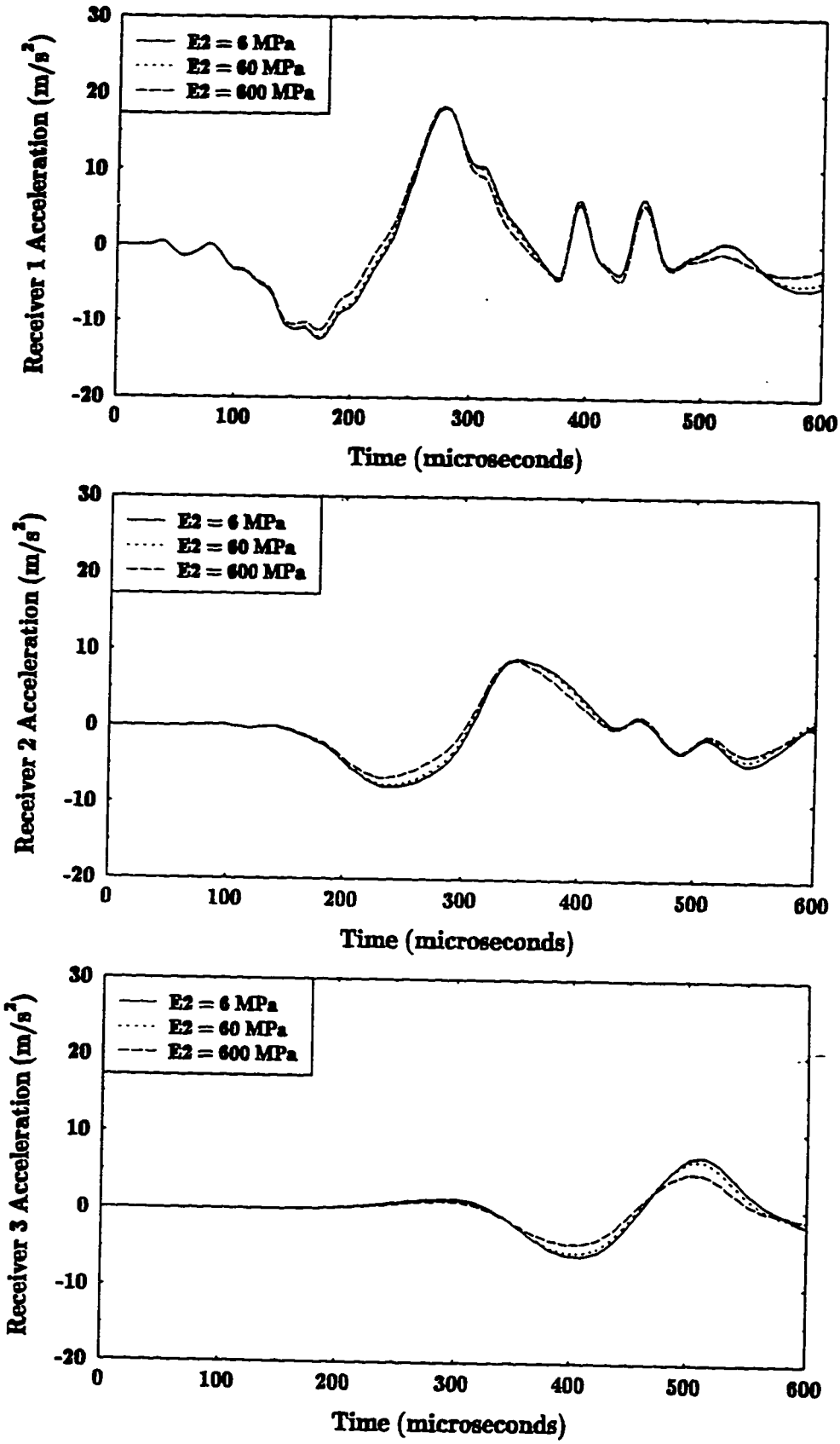

Figure 8.7. Effects of varying Young's modulus in the second layer.

Calculated time histories are provided in Figure 8.8. These results show that the stiffness of the third layer had essentially no effect on the computed accelerations. This indicates that boundary conditions applied to the third layer do not significantly affect the time histories.

Damping

Viscous damping was included in the models to simulate the material damping of the materials in a pavement system. The effects of this damping were studied by analyzing three models with damping to shear modulus ratios, η/G, of 1.0×10^{-6} s, 2.5×10^{-6} s, and 4.0×10^{-6} s. This range of values demonstrates the effect of damping on smoothing the response curves and its ability to influence the magnitudes of peaks in the responses. The same values of damping to shear modulus ratio were assigned to all three layers in the system.

Acceleration time histories from these analyses are plotted in Figure 8.9. These response histories show that increased damping slightly reduced the magnitudes of the peak accelerations and smoothed regions of sharp curvature. When adequate damping was provided, damping did not appear to influence the phase of the responses at any of the receivers.

Overview

Table 8.1 summarizes the results of the parametric study for the layered system shown in Figure 8.1. Increasing the stiffness and thickness of the top layer significantly decreased the magnitude of the maximum positive acceleration at each receiver. Increasing Young's modulus of the top layer also caused the maximum positive acceleration at each receiver to occur earlier. While increasing the thickness of the top

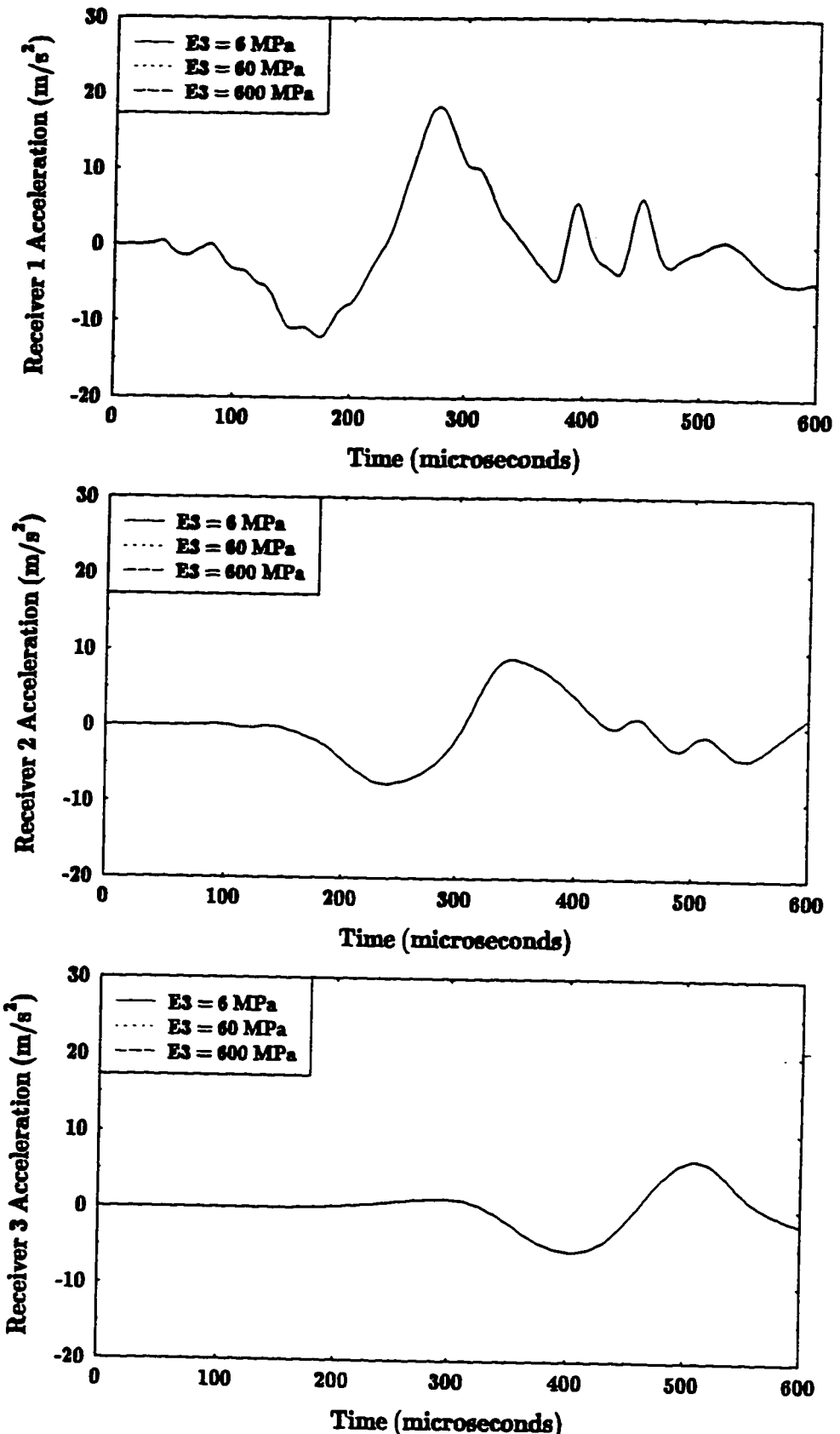

Figure 8.8. Effects of varying Young's modulus in the bottom layer.

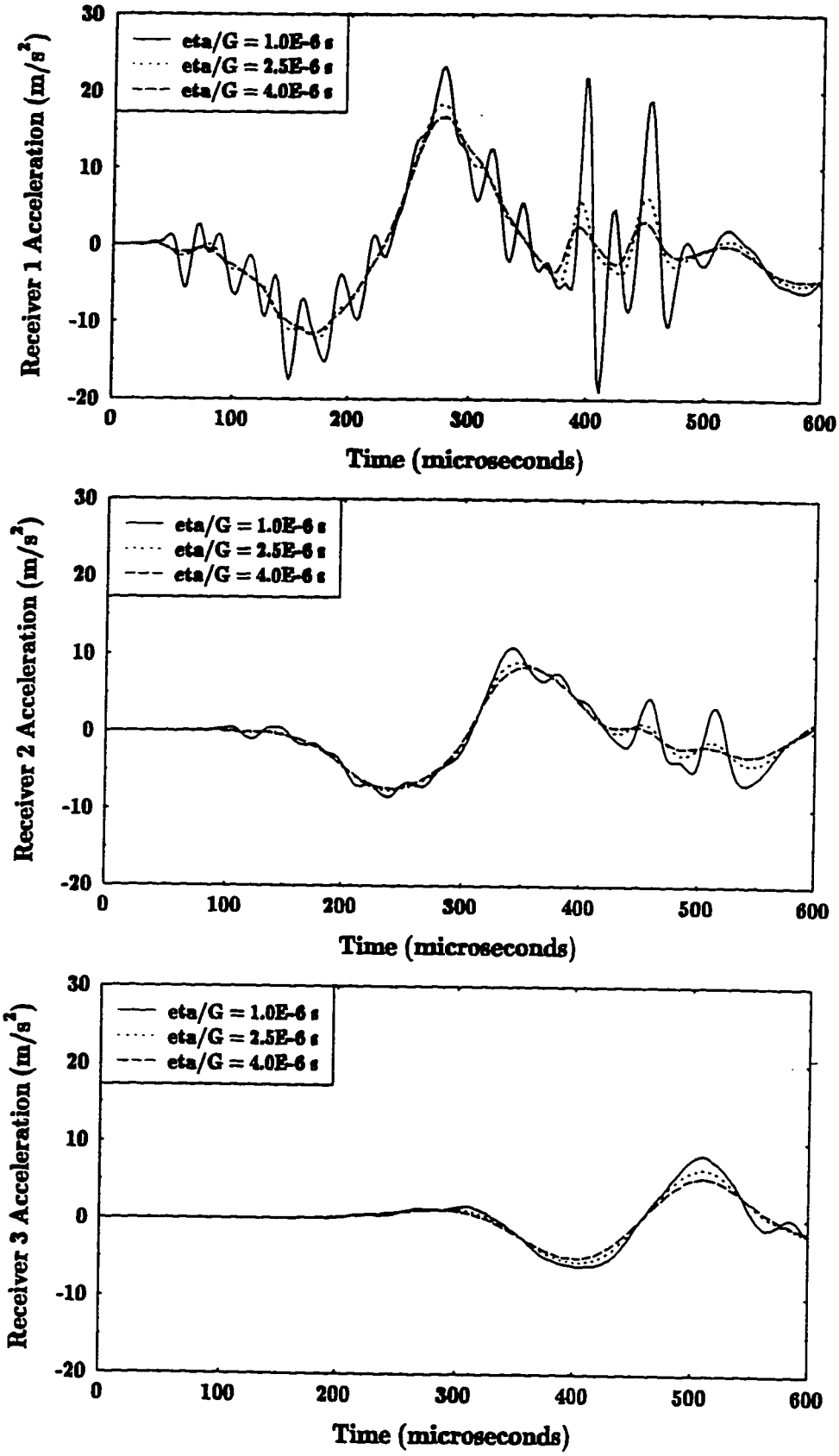

Figure 8.9. Effects of varying the damping to shear modulus ratio.

Table 8.1. Summary of results from parametric study.

Parameter	Input Value	Change in Input Value (%)	Occurance of Max. Pos. Accel. Rec. 1 (μs)	Change in Max. Pos. Accel. Rec. 1 (%)	Occurance of Max. Pos. Accel. Rec. 2 (μs)	Change in Max. Pos. Accel. Rec. 2 (%)	Occurance of Max. Pos. Accel. Rec. 3 (μs)	Change in Max. Pos. Accel. Rec. 3 (%)
E_1	50 MPa	+25	272	-17	338	-13	480	-14
	40 MPa	--	278	--	348	--	510	--
	30 MPa	-25	288	28	366	22	552	14
d_1	250 mm	+25	278	-17	342	-6	500	-47
	200 mm	--	278	--	348	--	510	--
	150 mm	-25	284	34	374	38	534	22
ρ_1	2400 kg/m^3	+3.4	280	-1	350	-1	516	-1
	2320 kg/m^3	--	278	--	348	--	510	--
	2240 kg/m^3	-3.4	278	1	346	1	506	1
ν_1	0.25	+25	280	-1	348	-3	512	-2
	0.20	--	278	--	348	--	510	--
	0.15	-25	276	0	346	1	508	-1
E_2	600 MPa	+900	278	0	346	-2	508	-25
	60 MPa	--	278	--	348	--	510	--
	6 MPa	-90	278	-1	348	-1	512	8
E_3	600 MPa	+900	278	0	348	0	510	0
	60 MPa	--	278	--	348	--	510	--
	6 MPa	-90	278	0	348	0	510	0
η/G	4.0x10^{-6} s	+60	280	-9	344	-7	510	-17
	2.5x10^{-6} s	--	278	--	348	--	510	--
	1.0x10^{-6} s	-60	280	27	354	21	510	28

layer caused the maximum positive acceleration at the second and third receivers to occur earlier, it had a less substantial effect on the occurrence time of the maximum positive acceleration at the first receiver.

The other variables had little or no effect on the magnitudes and occurrence times of the maximum positive accelerations. Density and Poisson's ratio of the top layer had a small effect on the occurrence times of the maximum positive accelerations. However, these variables had even less effect on the magnitudes of the maximum positive accelerations. Values of Young's modulus for the lower layers had little effect on either the magnitudes or the occurrence times for maximum positive accelerations. The small effects of varying Young's modulus of the second layer are only apparent because the variable was allowed to vary by orders of magnitude.

Increasing the ratio of damping to shear modulus reduced the magnitudes of the maximum positive accelerations but had no effect on the occurrence times. The influence on magnitude of the maximum positive accelerations was small compared to the effects of varying the stiffness and thickness of the top layer.

CRACK DEPTH AND LOCATION

To investigate the effects of geometric complexities, the finite-difference model was modified to simulate the presence of a partial depth, open, surface crack in the concrete slab. To make this modification it was necessary to model the concrete slab with two layers: one layer modeling the region from the surface to the tip of the crack and a second layer modeling the region from the crack tip to the bottom of the slab. Incorporation of the boundary conditions for this new configuration also required that

each layer be divided into two areas joined at the horizontal location of the crack. This configuration is shown schematically in Figure 8.10.

As with the simple layered system model (Chapter 7), continuity of displacements was enforced at the interface between layers. Equilibrium was also enforced at the interface between layers by equating σ_{zz} and τ_{rz} at the bottom of the upper layer and at the top of the lower layer. The interface of the two areas that comprise the top layer models the faces of the open crack. Along these faces, the horizontal normal stress and the shear stress were set equal to zero. Vertical interfaces between the two regions comprising other layers were subject to continuity of displacements and equilibrium requirements similar to the horizontal interfaces between layers. Four nodes were located at the bottom of the crack. Continuity of displacements and equilibrium were satisfied for these nodes.

Crack Depth

To investigate the influence of crack depth, the finite-difference program simulated the dynamic response of a system where the slab contained a crack midway between the second and third receivers. This configuration is shown in Figure 8.11. In various analyses the crack was assigned depths of 20 mm, 50 mm, 100 mm, 150 mm, and 180 mm. These crack depths correspond to 10, 25, 50, 75, and 90 percent of the slab depth.

The acceleration response histories from these models are presented in Figure 8.12. As expected, the presence of a crack located between the second and third receivers does not significantly influence the first receiver until late in the response history. Changes in the response history are limited to minor magnitude changes until a time of approximately 470 μs. Then, significant differences occur in the responses of the various models. This change in the responses roughly coincides with the expected arrival of a

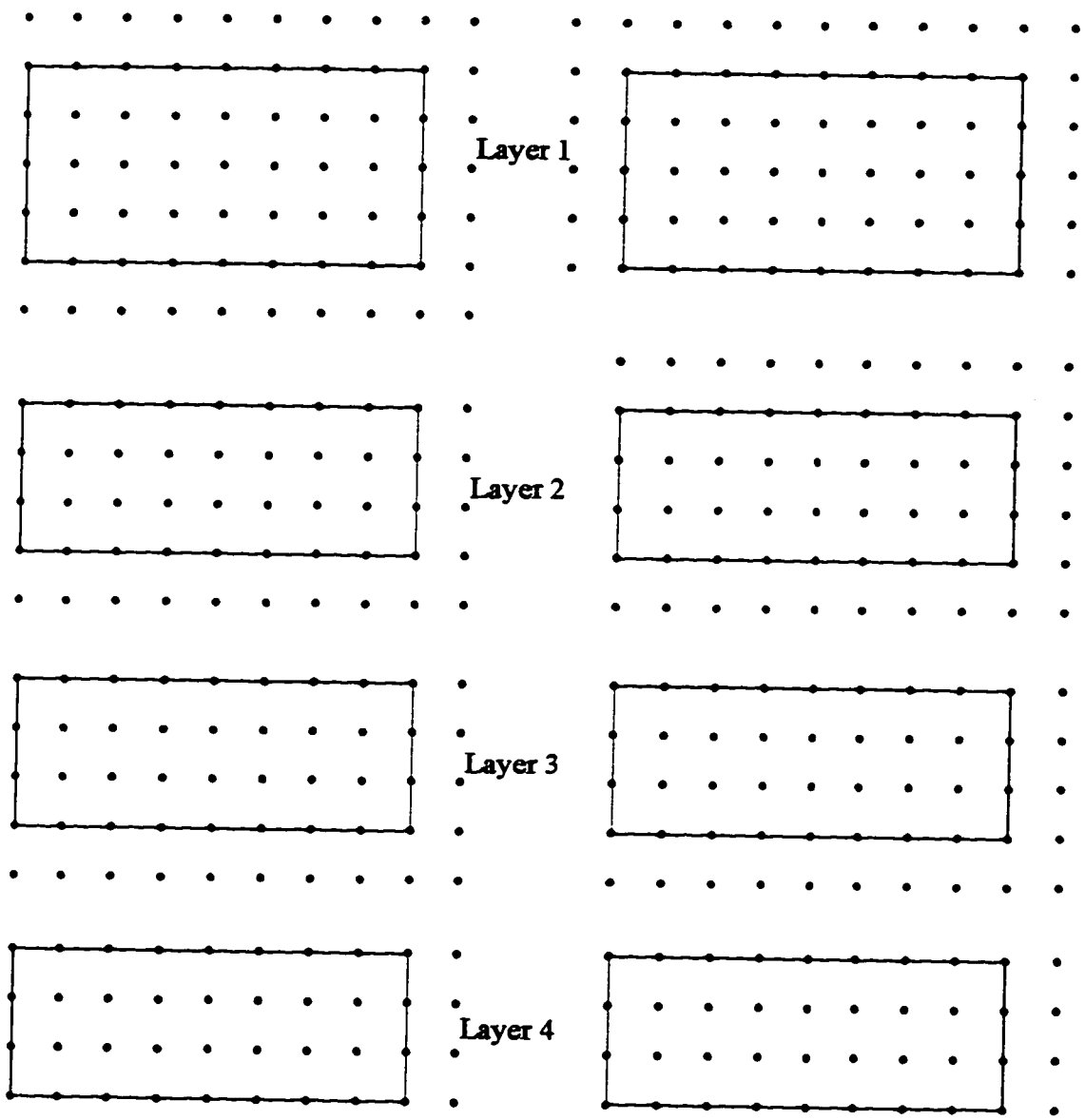

Figure 8.10. Finite-difference mesh for crack models.

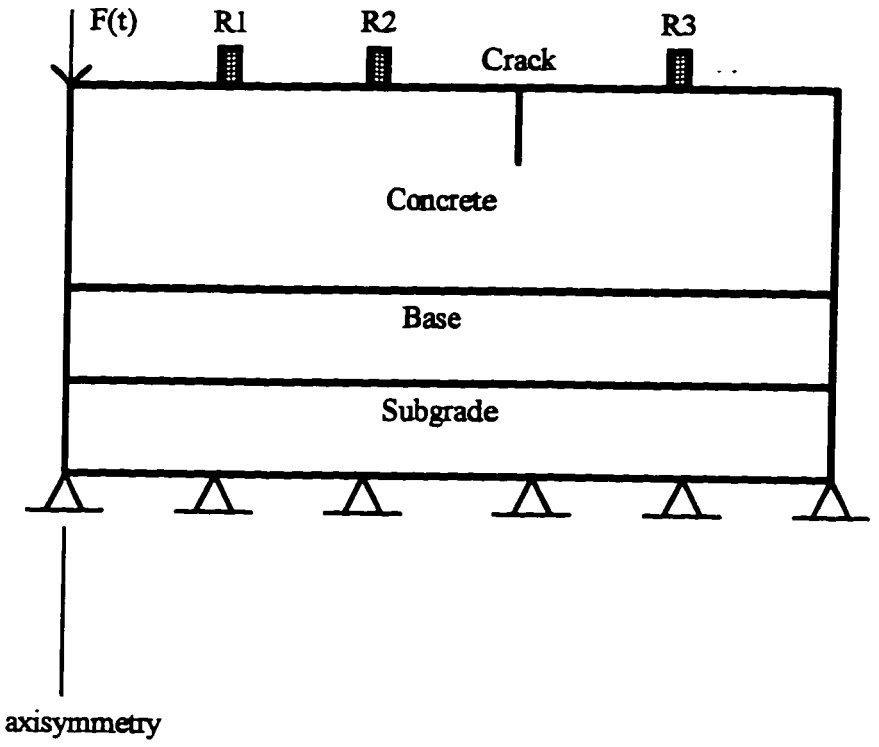

Figure 8.11. Geometry for crack parametric study.

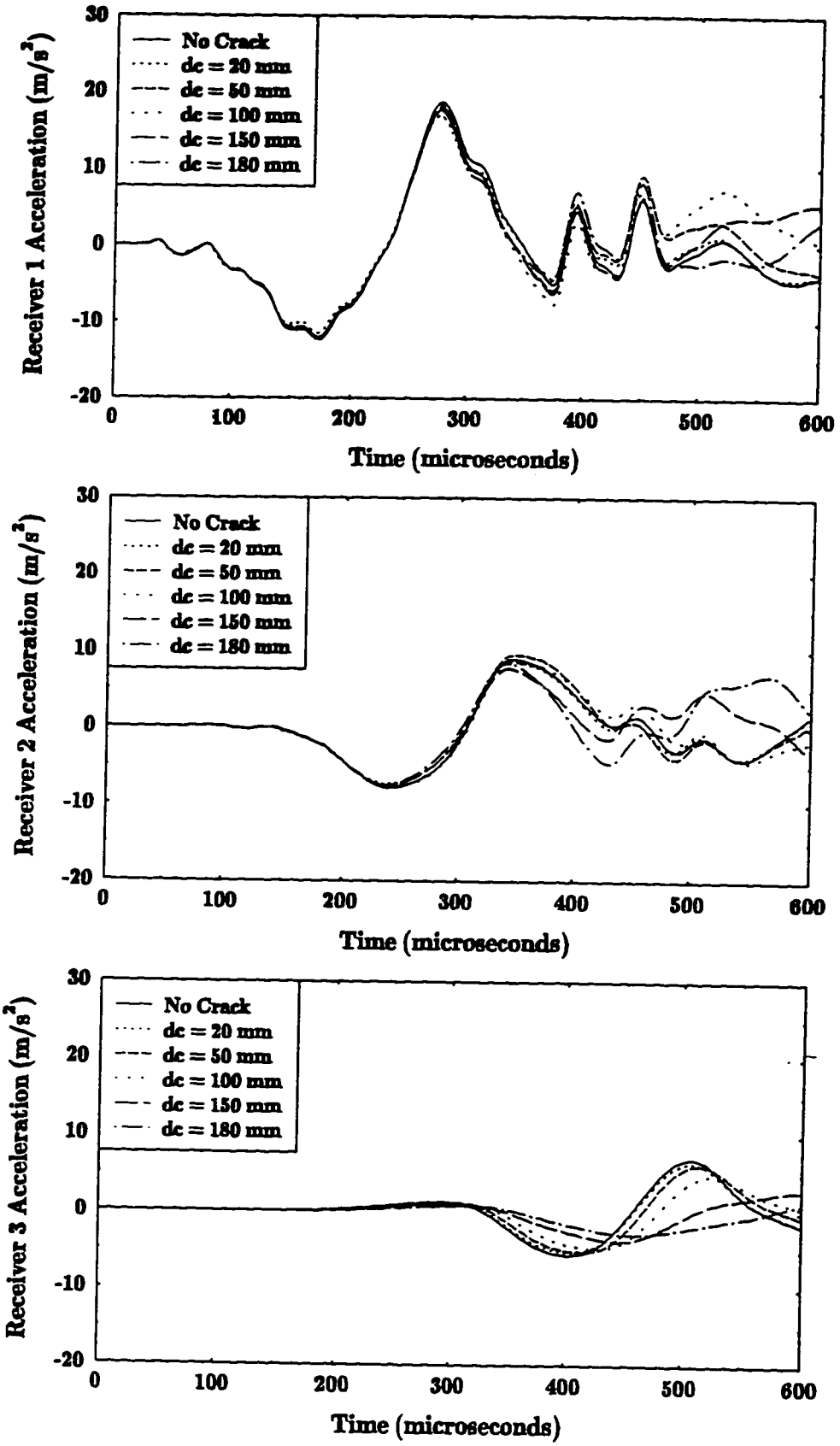

Figure 8.12. Effects of varying crack depth.

surface wave reflected by the crack, which is expected to occur between the times of 310 μs and 480 μs. A time of 480 μs is the projected arrival of the major negative peak.

Response histories at the second receiver show similar characteristics. At this receiver, the responses diverge earlier (slightly before a time of 350 μs) because the energy reflected by the crack does not need to travel as far. A surface wave reflected by the crack would be expected to arrive at the second receiver between times of 250 μs and 400 μs. The arrival of the reflected wave occurs earlier in the expected range than it did for the first receiver. However, the difference is small, and attributable to the crude approximations used to estimate the arrival times.

As expected, the third receiver, located across the crack from the impact, shows differences throughout the response histories for the models. These response histories show that increasing the crack depth causes the peaks in the response histories to have lower magnitudes, occur later, and appear to be caused by lower frequency components of the surface waves. High frequency components of the surface waves were not expected to appear at receivers beyond the crack. Since the high frequency components propagate in shallow material, they should be reflected by the crack. In this sense, the crack was expected to filter the high frequency content from responses at the third receiver.

The widely varying results at the third receiver indicate that crack depth may be a variable that can be identified by the dynamic response algorithm. Responses on the same side of the crack as the impact will only be useful in identifying the crack depth if the model can simulate the experimental result for sufficient duration.

Crack Location

Effects of crack location were studied by changing the location of the crack in the finite-difference model. One simulation was conducted without a crack in the model.

Then, five models were analyzed with a crack with a depth of 100 mm located 75 mm, 225 mm, 375 mm, 450 mm, and 525 mm from the impact. The first location corresponds to the midway point between the impact and the first receiver. The second location is the midway point between the first and second receivers. The other three crack locations are between the second and third receivers.

Figure 8.13 shows the response histories generated by the models with varying crack location. The largest deviation in response histories from the model with no crack occurs for the model with the crack closest to the impact. A crack at this location appears to have a filtering effect on high frequency components of the surface wave. This crack also causes the peaks in the response histories to have greater magnitudes and occur later.

Cracks located between a receiver and the impact cause the peaks in the response histories to occur later. This effect is demonstrated at the second receiver, where the peaks in responses from the two models with cracks located between the receiver and the impact occur later in the responses than the peaks in the other responses. For receivers beyond the crack, peaks in the responses occurred later as the crack moved toward the receiver. This is seen with close examination of the responses at the third receiver. Apparently, a crack far from the impact filters out more high frequency components of the surface wave than a crack near the impact. This filtering would cause a crack far from the impact to allow only frequencies more dependent on the lower layers to reach the third receiver.

Effects of crack location on response histories indicate that the algorithm should be able to determine at least the receiver or impact locations between which the crack lies.

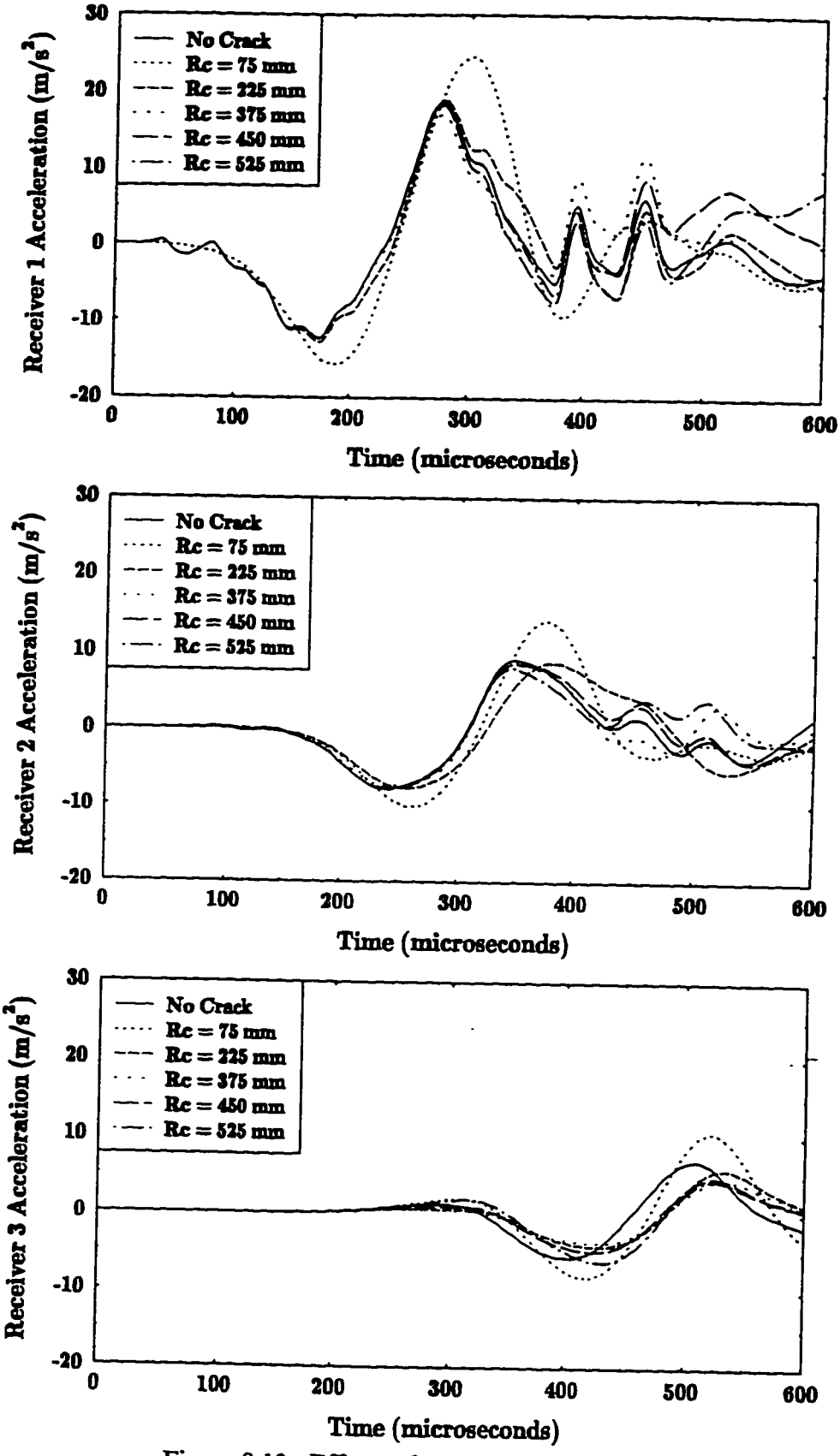

Figure 8.13. Effects of varying crack location.

SUMMARY

A parametric study was conducted to determine the effects of input variables used in the finite difference models. Varying the stiffness of the top layer significantly changed the phase and magnitude of the acceleration response histories. Thickness of the top layer was found to have a greater influence in the magnitude of the response histories and a less predictable effect on the phase of the responses. The other variables in a layered system had little effect on magnitude of the peaks in the responses or the occurrence times of the peaks.

The parametric study also investigated the influence of crack depth and location on response histories. Cracks were found to most influence the responses at receivers located on the side of the crack opposite the impact.

Chapter 9

APPLICATION OF THE DYNAMIC RESPONSE ALGORITHM

This chapter presents the application of the dynamic response algorithm to impacts and acceleration response histories obtained experimentally. The experimental results were obtained for a simple layered system. The algorithm was also applied to simulated results obtained from a model containing a partial depth, open, surface crack. These reconstructions were performed to assess the algorithm's potential for determining the depth and location of a crack.

TEST SPECIMENS AND TESTING

Test specimens consisted of a concrete slab with nominal dimensions of 1.2x2.4x0.2 m, three 152 by 305 mm cylinders, and three 75x102x406 mm prisms. The slab was placed on top of approximately 100 mm of uniformly graded aggregate in forms that were 300 mm deep. This underlying layer of aggregate was intended to simulate the

presence of a base course under the slab. The forms, slab, and aggregate layer were located on top of 150 mm of foam insulation boards.

Experimental test specimens were produced from concrete delivered to the University of Washington on September 23, 1994. The slab was placed in one lift compacted with a vibrator. Cylinders were prepared in three lifts, and compacted by rodding in compliance with ASTM C 192. Prisms were prepared with two lifts compacted on a vibrating table.

Dynamic Response Testing

The slab was allowed to cure outdoors until it reached an age of 27 months. Then, tests were conducted to record the response of the slab to an impact. The impact was generated by an instrumented hammer produced by PCB Piezotronics, Inc. Acceleration response histories were measured with three accelerometers that were also produced by PCB Piezotronics, Inc. These accelerometers were located 150 mm, 300 mm, and 600 mm from the point of impact. These locations are the locations used for the receivers in the parametric study (Chapter 8). The impact and the response histories were recorded with a Tektronics TDS 754 A digitizing oscilloscope at a sampling rate of 2.0 μs. Data recorded from these tests were used as target values for the dynamic response algorithm applied to a layered system.

Figure 9.1 shows the impact and responses measured during three tests. The recorded impacts, normalized with respect to their maximum force, are shown in the first plot. The recorded acceleration responses at the three receivers are shown in the subsequent three graphs. These responses were normalized with respect to the maximum force in the impact that generated them.

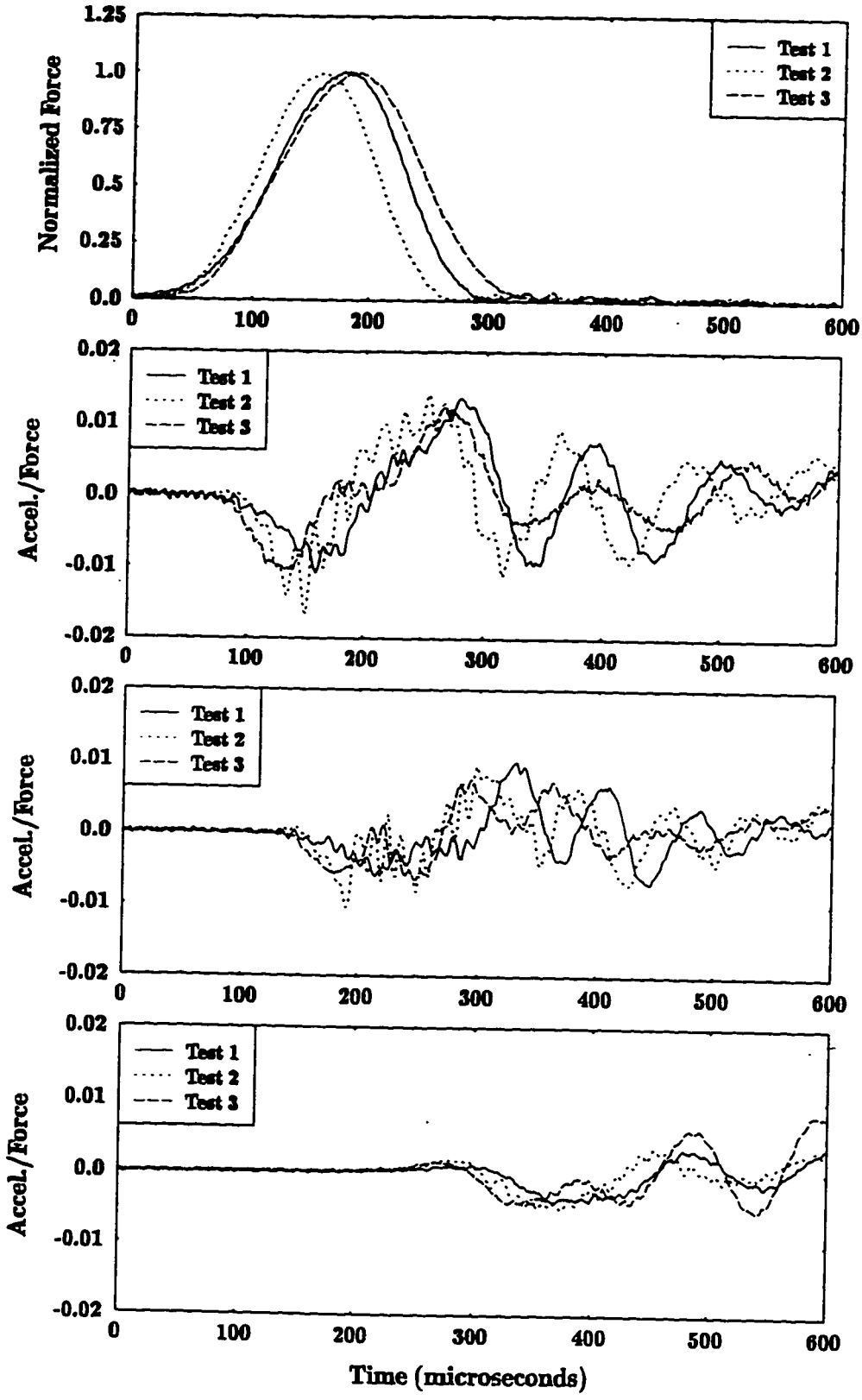

Figure 9.1. Normalized force and acceleration histories for three tests.

Variations in impact duration and occurrence times for the maximum force can be seen in the first graph. The resulting variations in the responses is apparent in the other graphs. It is interesting to note that the maximum forces in the impacts occur after the first negative peaks in the responses at the first receiver. This occurs because the impact has a duration much longer than the time required for the surface wave to travel to the first receiver.

Laboratory Testing

Cylinders were covered with plastic after placing for a period of 24 hours. Then, the cylinders were moved to a fog room for moist curing. After 27 months, the cylinders were tested for static Young's modulus according to ASTM C 469. One of the cylinders was poorly compacted during placement and provided a static modulus approximately 32 percent lower than the other two cylinders. The poorly compacted cylinder is shown at the left of the photograph in Figure 9.2. A region of poor compaction in the lower half of the cylinder is apparent when this region is compared to the other cylinders. The mean static Young's modulus obtained from the other two cylinders is presented in Table 9.1.

Prism specimens were also covered with plastic for 24 hours after placing. After that, they were submerged in water for wet curing to an age of 27 months. Then, they were tested for fundamental transverse and fundamental torsional frequencies according to ASTM C 215. The fundamental transverse frequency was used to calculate the dynamic Young's modulus for each prism. The fundamental torsional frequency was used to obtain the dynamic shear modulus for each prism. These values of Young's modulus and shear modulus were then used to compute the dynamic Poisson's ratio for each prism. Mean values for dynamic Young's modulus and dynamic Poisson's ratio are also presented in Table 9.1.

Figure 9.2. Cylinder specimens for static Young's modulus measurements.

Table 9.1. Experimental results from laboratory specimens.

Variable	Specimens		
	Cylinders	Prisms	Cores
Static Young's Modulus	41.1 GPa	--	--
Dynamic Young's Modulus	--	48.9 GPa	36.5 GPa
Dynamic Poisson's Ratio	--	0.219	--
Slab Depth	--	--	205 mm

After the dynamic response testing was completed, three 100-mm diameter cores were cut from the slab. These cores were used to measure the actual thickness of the slab in the region where testing was conducted. Then, the cores were sawn so that both ends were flat. The cores were tested for fundamental longitudinal frequency according to ASTM C 215. Dynamic Young's modulus for the cores was calculated from the measured fundamental longitudinal frequencies. Mean values for depth and dynamic Young's modulus obtained from these measurements are shown in Table 9.1.

The values of dynamic Young's modulus measured from prisms was 19 percent greater than the static Young's modulus measured with cylinders. These results are consistent with observations of other researchers who have observed dynamic Young's modulus to be 20 to 30 percent higher than static Young's modulus (Mindess and Young 1981). The dynamic Young's modulus determined for cores was much lower than the values determined for the laboratory specimens. Dynamic Young's modulus was expected to be lower for the cores than for the prisms because the prisms were provided with more favorable curing conditions. Another reason that the cores may exhibit a low dynamic Young's modulus value is that cores may be damaged by vibration of the core saw (Mindess and Young 1981).

APPLICATION OF ALGORITHM

The dynamic response algorithm (Steps 2-4 in Chapter 7) was implemented with MATLAB (Sigmon 1992) in a manner similar to that used for the magnetic algorithm. The user provides a recorded impact, dynamic response measurements obtained with an array of receivers, and initial trial values for depth and material properties of the concrete slab. Then, the algorithm computes the dynamic response of the assumed system and the

difference between the computed and measured responses. The algorithm's output is the slab depth and material properties that minimize the sum of squared differences (SSD) defined in Equation 7.1.

Unlike the magnetic algorithm, the dynamic response algorithm used only one minimization function. The fmins() command (Grace 1990), that uses a simplex solution method (Nelder and Mead 1964), was used to minimize SSD. SSD was calculated by summing the squared differences between data points from the time of impact to 125 data points (250 μs) after a given receiver recorded an acceleration greater than 5 percent of the maximum acceleration recorded in the response of that receiver. For the tests conducted in this study, these data describe the regions of maximum negative acceleration and maximum positive acceleration.

Comparison of Measured and Simulated Responses

A comparison of measured and simulated responses was conducted to determine how well the finite-difference model was able to simulate the experimental responses. Properties of the finite-difference model were selected from a minimization performed by the dynamic response algorithm. Young's modulus and depth of the slab were the only model variables included in the algorithm for this minimization, and all three receivers were used. Response histories from Test 1 (Figure 9.1) were used as the measured responses.

Figure 9.3 presents the comparison of the algorithm's minimized results and the experimental measurements. The recorded impact, used as input for the model, is shown in the first graph. Experimental and simulated results for the first, second, and third receivers are presented in the subsequent three graphs. The vertical, solid lines in the

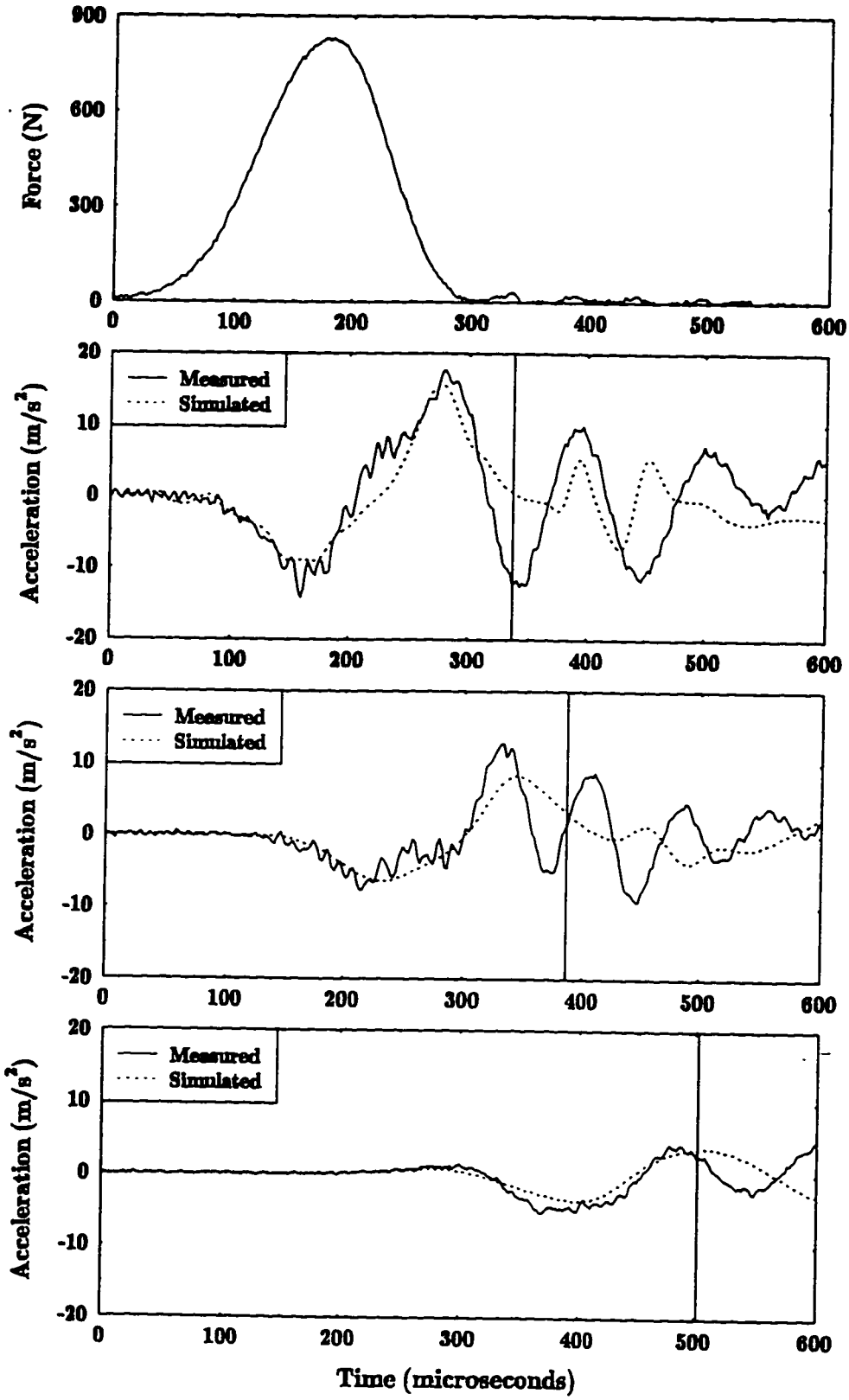

Figure 9.3. Comparison of measured and simulated responses.

graphs of the responses indicate the end of the data used in the dynamic response algorithm.

Finite-difference results for the model with the material properties selected by the algorithm agree, in general, with the experimental results. The occurrence times of the maximum negative accelerations in the experimental and simulated response histories are well matched. However, the magnitude of the maximum negative acceleration is underestimated by the finite-difference model at the third receiver.

Magnitudes of the maximum positive accelerations in the experimental and simulated responses agree for the first and third receivers. The maximum positive acceleration at the second receiver is underestimated by the finite-difference model. Occurrence times for the maximum positive accelerations in the responses generated by the finite-difference model are slightly earlier than the peaks in the experimental responses for the second and third receivers. The simulated maximum positive acceleration at the first receiver occurs slightly before the maximum positive acceleration in the measured response.

Peaks in the measured acceleration responses that occur after the maximum positive accelerations are not targeted by the algorithm. The data describing these peaks were omitted because the finite-difference model was not able to simulate them. Apparently, the later peaks are caused by differences between the model and the actual slab. Some differences between the model and the slab that may contribute to the later peaks are: 1) the roughness of the bottom of the slab, which will have a scattering effect on wave fronts that are reflected by the bottom of the slab, 2) the slab is actually rectangular and would be expected to respond differently than the cylindrical model, and 3) lack of homogeneity of the concrete may cause reflections and scattering of wave fronts that cannot be simulated by the model.

Behavioral differences between the rectangular test specimen and the cylindrical model include arrival times and geometries of reflected wave fronts. Arrival times of reflected wave fronts will differ between the model and the slab because the distance to the vertical free edge of the model cannot represent the locations of the slab boundaries in both horizontal directions. Geometries of the reflected wave fronts will also differ between the model and slab. In the axisymmetric model, surface wave fronts reflected by the vertical free edge will propagate toward the impact location with diminishing circumference of the wave front. Surface wave fronts reflected by the vertical boundaries of the slab, which are linear, will propagate with increasing radius of curvature.

It is unlikely that either of these differences is the sole cause of the late peaks. Reflected waves would not be expected to cause accelerations as large as the peaks that occur late in the recorded responses. Reflected surface waves in the slab would not be expected to arrive at the receiver until after a time of 480 μs. The late peaks begin to occur before this time.

Echoing of the compression wave is also not the cause of the late peaks since this would produce peaks at the same frequency at each receiver. The frequency of the peaks in the response of the second receiver occur at a noticeably higher frequency than the late peaks at the first receiver.

Receiver and Variable Combinations

The dynamic response algorithm was applied to the experimental results from the testing program described earlier in this chapter. Various combinations of receivers were targeted by the algorithm, and different combinations of variables in the finite-difference model were allowed to be changed by the algorithm. These combinations of receivers and

model variables were used to determine which combinations provided the most useful and meaningful results.

Five combinations of receivers were used by the algorithm: 1) only the first receiver, 2) only the second receiver, 3) only the third receiver, 4) all three receivers, and 5) the second and third receivers.

The following eight combinations of variables were used with the algorithm:

1) E_1 and d_1.
2) E_1, d_1, and η/G.
3) E_1, d_1, and ν_1.
4) E_1, d_1, and ρ_1.
5) E_1, d_1, η/G, and ν_1.
6) E_1, d_1, η/G, and ρ_1.
7) E_1, d_1, ν_1, and ρ_1.
8) E_1, d_1, η/G, ν_1, and ρ_1.

where E_1, d_1, ν_1, and ρ_1 are Young's modulus, depth, Poisson's ratio, and density of the slab, respectively, and η/G is the damping to shear modulus ratio for all three layers in the finite-difference model. Initial trial values for the variables, when they were included, were: $E_1 = 33$ GPa, $d_1 = 250$ mm, $\eta/G = 2.5 \times 10^{-6}$ s, $\nu_1 = 0.20$, and $\rho_1 = 2320$ kg/m^3. When η/G, ν_1, and ρ_1 were excluded from the algorithm, they were assigned values of 3.0×10^{-6} s, 0.20, and 2400 kg/m^3, respectively. The algorithm was not sensitive to the initial trial values as long as reasonable values were used. Unrealistic values of E_1 (>80 GPa) and ρ_1 (> 9000 kg/m^3) did cause the algorithm to converge to erroneous local minimums.

Minimization Results

Minimizations were performed on response histories from Test 1 (Figure 9.1) using all combinations of receivers and variables. Optimal results for minimizations performed using all of the receiver combinations and the first three variable combinations are presented in Table 9.2.

The most promising results were obtained when only the third receiver was used, and when the second and third receivers were used. For these cases, estimates of Young's modulus were within 5 percent of the static Young's modulus measured from companion cylinders (Table 9.1). Slab depths were also identified accurately, within 11 percent of the actual depth.

The algorithm's convergence to values near the static Young's modulus was not predicted but is reasonable. The algorithm was expected to converge to values near the dynamic Young's modulus determined from the core specimens since both tests are dynamic evaluations of the same material. However, overestimating dynamic Young's modulus of the cores is reasonable since the cores may be damaged by vibration of the core saw (Mindess and Young 1981). Any damage to the cores would cause a decrease in the observed Young's modulus values.

Using the first receiver by itself causes the algorithm to converge to values of Young's modulus (Table 9.2) significantly lower than the dynamic Young's modulus determined for cores cut from the slab (Table 9.1). Slab depths selected by the algorithm were greater than the actual depth by approximately 50 percent when only the first receiver was used. These large errors in the two variables that should be easiest to identify indicate that errors at the first receiver are large. Large errors at receivers close to the impact are probably due to variability in the location of impact. Errors in the location

Table 9.2. Reconstruction for an experimental test result.

Variables Included In Minimization	Receivers Used In Minimization				
	1	2	3	1,2,3	2,3
E	27.2 GPa	45.0 GPa	42.2 GPa	38.5 GPa	41.2 GPa
d	309 mm	296 mm	199 mm	242 mm	217 mm
E	37.0 GPa	43.7 GPa	42.7 GPa	38.7 GPa	41.1 GPa
d	314 mm	289 mm	194 mm	244 mm	221 mm
η/G	3.52×10^{-6} s	9.75×10^{-7} s	3.98×10^{-6} s	2.05×10^{-6} s	1.13×10^{-6} s
E	28.8 GPa	44.9 GPa	42.9 GPa	37.3 GPa	39.5 GPa
d	308 mm	289 mm	203 mm	251 mm	228 mm
ν	0.250	0.145	0.234	0.174	0.175

of the impact may be significant in comparison to the distance from the impact to the receiver. For a halfspace with unknown Young's modulus, an error of 5 percent in the location of the impact corresponds to a 5 percent error in wave velocity, but results in a 10 percent error in Young's modulus. This occurs because Young's modulus is proportional to the square of wave velocity. For receivers further from the impact, an error in impact location would be expected to be a smaller percentage of the distance from the impact to the receiver.

Minimizations performed using only the second receiver provided estimates of Young's modulus within 10 percent of the static Young's modulus measured from the cylinder specimens (Table 9.1). However, slab depths obtained using only the second receiver were consistently overestimated by more than 40 percent.

Using multiple receivers reduces the influence of errors associated with any given receiver on the results of the algorithm. This is seen in minimizations where all three receivers were used (Receiver combination 1,2,3 in Table 9.2). For this case, Young's modulus results were between the dynamic Young's modulus determined from the cores and the static Young's modulus determined from moist cured cylinders. Slab depths were consistently overestimated by approximately 20 percent, reflecting the influence of the first receiver.

Including the damping to shear modulus ratio (Variable combination 2) in the algorithm had little effect on the values of Young's modulus and slab depth selected by the algorithm. Values of Poisson's ratio identified by the algorithm differed from the Poisson's ratio measured by frequency testing by as much as 34 percent. However, all of the values determined with the third combination of variables were realistic values for concrete.

Results for minimizations using all of the receiver and variable combinations are summarized in Appendix B. In general, the algorithm was unable to identify density of the

slab. Reasonable values for density would be between 2240 kg/m^3 and 2400 kg/m^3, and few of the results were in this range. The algorithm was also unable to consistently identify reasonable values of Poisson's ratio when both Poisson's ratio and the damping to shear modulus ratio were included in the minimization.

Extended Response Histories

The duration of the response histories used to compute the sum of squared differences (SSD) between the measured and simulated responses was increased to try to extend the region of the response that was reproduced by the finite-difference model. For this portion of the investigation, SSD was computed by summing the squared differences from the time of impact to 175 data points (350 μs) after each receiver recorded an acceleration greater than 5 percent of the receiver's maximum acceleration.

Optimal results for minimizations performed on responses from Test 1 using all five combinations of receivers and the first three combinations of variables are presented in Table 9.3. Using only the first receiver, only the third receiver, the second and third receivers, or all three receivers did provide consistent results. Young's modulus identified from these receiver combinations were all between 30.9 GPa and 33.1 GPa, and slab depths were between 298 mm and 307 mm. These estimates of Young's modulus are significantly lower than would be expected from the laboratory tests and the slab depths are in error by approximately 50 percent. Using only the second receiver to perform the reconstruction yielded slab depths with 13 percent of the actual depth. However, estimates of Young's Modulus and Poisson's ratio were much higher than would be expected for concrete.

Table 9.3. Reconstruction results from extended response histories.

Variables Included In Minimization	Receivers Used In Minimization				
	1	2	3	1,2,3	2,3
E	31.0 GPa	56.8 GPa	31.1 GPa	32.1 GPa	32.1 GPa
d	293 mm	230 mm	304 mm	301 mm	304 mm
E	31.0 GPa	73.3 GPa	32.0 GPa	32.0 GPa	31.7 GPa
d	293 mm	191 mm	296 mm	302 mm	307 mm
η/G	3.23×10^{-6} s	1.44×10^{-6} s	1.45×10^{-6} s	3.22×10^{-6} s	3.34×10^{-6} s
E	32.9 GPa	58.5 GPa	32.1 GPa	32.5 GPa	33.1 GPa
d	298 mm	217 mm	304 mm	300 mm	304 mm
ν	0.259	0.351	0.143	0.146	0.132

Multiple Slab Layers

To determine if varying Young's modulus of the slab through its depth could explain the variation in results seen for the various receiver combinations in Table 9.2, the slab was modeled with three layers in the finite difference model. The top layer in the concrete slab was assigned a depth on 25 mm. This was done because it is believed that the properties of the concrete near the surface may differ from the properties of the deeper concrete due to greater moisture loss, higher paste content, and greater compaction during finishing. The second layer of the slab was assigned a thickness of 100 mm. This value provides a combined depth of the first two layers that is expected to be approximately half of the total depth of the slab.

Three values of Young's modulus, one for each layer in the slab, and the depth of the third layer, were varied in the optimization routine and estimated by the algorithm. Selecting the thickness of the third layer with the algorithm allows the algorithm to estimate the total depth of the slab. The geometric model for the multi-layered slab model is shown schematically in Figure 9.3.

Again, the responses recorded in Test 1 (Figure 9.1) were targeted by the algorithm. Optimal results for a reconstruction performed using all three receivers are presented in Table 9.4. The estimated value for Young's modulus of the material near the surface is comparable to the value identified for a slab represented by a single layer using only the first receiver (Table 9.2). This result was expected because the response at the first receiver should be influenced primarily by shallow material (Nazarian 1984). The estimate for Young's modulus of the second layer was lower than would be expected from the laboratory tests. This occurs, again, because the shallow material has more influence on the nearest receiver. Young's modulus of the third layer was estimated to be higher than is reasonable for concrete. This high value causes the simulated responses at the

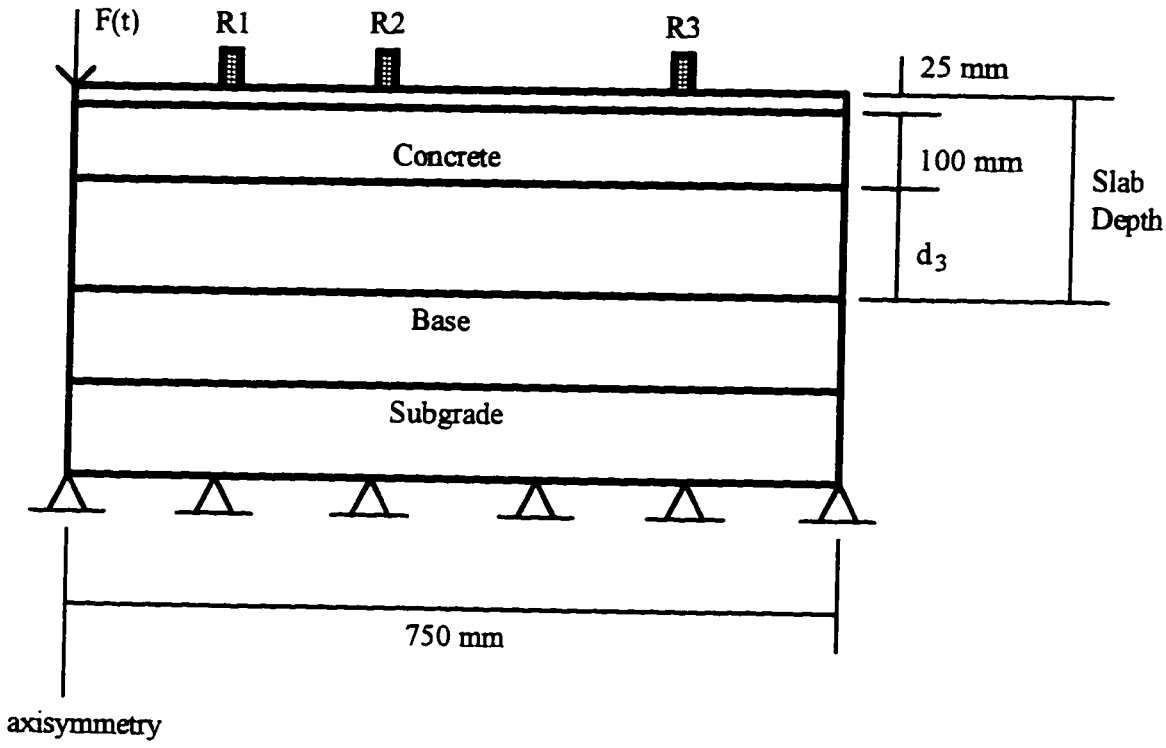

Figure 9.4. Concrete slab modeled with three layers.

Table 9.4. Reconstruction results for a slab represented with three layers.

Variable	Reconstruction Estimate
E_1	23.4 GPa
E_2	35.2 GPa
E_3	60.8 GPa
d_3 (Slab Depth)	101 mm (226 mm)

second and third receivers to better match the measured responses. Summing the products of depth and Young's modulus for the three layers (10.2 GN/m) demonstrates the similarity of the three-layer results with the one-layer slab results in Table 9.2 (9.32 GN/m).

Repeatability

Variability of the dynamic response algorithm, when applied to similar experimental responses, was investigated by applying the algorithm to two more sets of data recording an impact and the response of the slab. The minimizations used to study repeatability used the second and third receivers. Omitting the first receiver removed large errors expected to occur at the receiver nearest the impact.

Results from these minimizations are provided in Table 9.5. Values of Young's modulus were within 6 percent of the static Young's modulus for all of the minimizations. Slab depths erred by as much as 19.5 percent. Results for Test 2 were consistently worse at identifying slab depth than results for the other tests. Including the damping to shear modulus ratio added 10 percent error to the identification of slab depth in the results for Test 2. Otherwise, including the damping to shear modulus ratio had only minor effects on the other variables. Poisson's ratio again differed from the value measured in the laboratory by as much as 34 percent. However, all values of Poisson's ratio obtained were reasonable for concrete.

CRACK DEPTH AND LOCATION

No experiments were conducted on slabs with cracks. Therefore, application of the algorithm to geometries that contained a partial depth, open, surface crack in the slab

Table 9.5. Repeatability of dynamic response algorithm.

Variables Included In Minimization	Initial Trial Values	Test Number		
		1	2	3
E d	33 GPa 250 mm	41.2 GPa 217 mm	41.8 GPa 224 mm	42.3 GPa 215 mm
E d η/G	33 GPa 250 mm 2.0×10^{-6} s	41.1 GPa 221 mm 1.13×10^{-6} s	39.7 GPa 244 mm 1.37×10^{-6} s	41.9 GPa 213 mm 8.69×10^{-7} s
E d ν	33 GPa 250 mm 0.20	39.5 GPa 229 mm 0.175	41.1 GPa 229 mm 0.196	43.4 GPa 214 mm 0.274

required that measured time histories be obtained from a simulation. The simulation modeled the geometry shown in Figure 8.1 with a 100 mm crack located 375 mm from the impact. Properties of the model were assigned the values used in the parametric study (Chapter 8) to determine the influence of stiffness of the top layer. Young's modulus of the top layer was 40 GPa. The dynamic response algorithm was used to reconstruct the geometry used to simulated the measured time histories assuming that the crack location was one of the six possibilities used in the parametric study.

Table 9.6 shows the initial trial values, reconstruction results, and actual properties. The algorithm was able to accurately identify the stiffness and thickness of the top layer as well as the location and depth of the crack. Figure 9.5 shows the agreement in responses of the receiver locations for the model with properties selected by the algorithm and the model used to simulated the measured responses. These results indicate that the algorithm has the potential to identify crack depths and determine at least which receivers the crack is between.

SUMMARY

The dynamic response algorithm was applied to experimental data obtained by recording the impacts on a slab and its resulting responses. Young's modulus values (E_1) and slab depths (d_1) identified by the algorithm agreed well with static Young's modulus values obtained from laboratory tests and the actual depth of the slab. The algorithm was also able to identify reasonable values of Poisson's ratio consistently. However, the algorithm was not able to identify Poisson's ratio consistently when the damping to shear modulus ratio was also included in the minimization. The algorithm was also unable to identify density of the slab accurately. Another observation from applying the algorithm to

Table 9.6. Reconstruction results for cracked slab.

Parameter	Initial Trial Value	Reconstructed Value	Actual Value
Layer 1 Stiffness	33 GPa	40.0 GPa	40 GPa
Layer 1 Thickness	250 mm	200 mm	200 mm
Crack Depth	20 mm	100 mm	100 mm
Crack Location	5 Locations	375 mm	375 mm

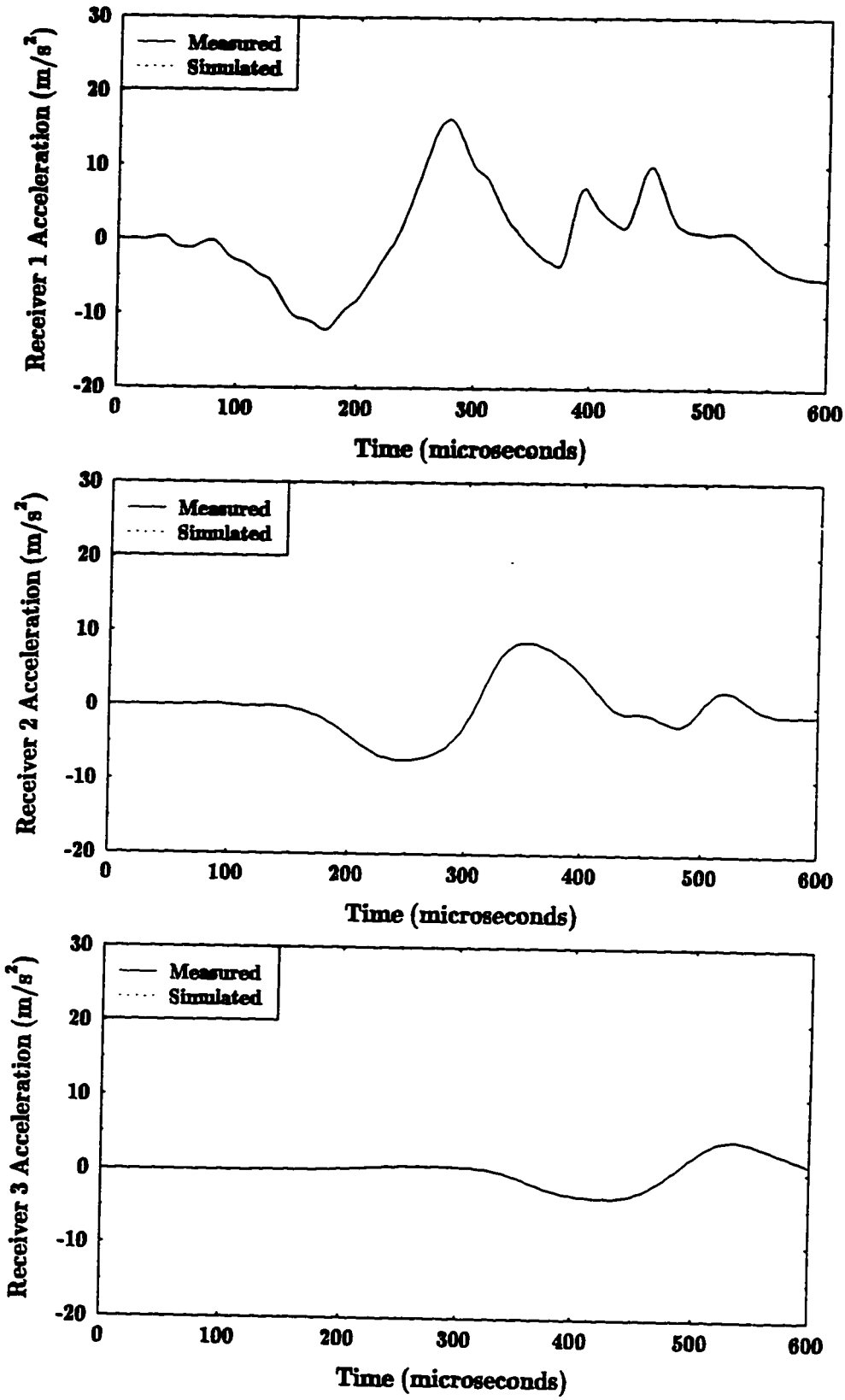

Figure 9.5. Minimization results for a cracked slab.

experimental responses was that receivers farthest from the impact provided the most accurate results. The large distance between impact and receiver reduces the influence of errors in impact location.

Applying the algorithm to a simulated response of a slab with a crack indicated that the algorithm may have the potential to estimate crack depth and location.

Chapter 10

SUMMARY AND RECOMMENDATIONS

This chapter provides a summary of the work presented in this thesis. Recommendations for further research are also presented.

SUMMARY OF COMPLETED WORK

Two algorithms were developed to improve nondestructive evaluation of civil engineering structures. Both algorithms take advantage of increasing availability of computational power that can be used to solve more complex problems. The first algorithm is a two-dimensional magnetic algorithm to decipher complex reinforcement configurations. The other algorithm is a dynamic response algorithm to determine the material properties and configuration of concrete members.

Two-Dimensional Magnetic Algorithm

A two-dimensional magnetic algorithm has been developed to determine the locations and sizes of steel bars in reinforced concrete members. To implement this algorithm, a magnetic field ($\mathbf{B}_o$) is applied to a reinforced concrete member, and the

distortion in the field (**B"**), caused by steel within the member, is measured with several receivers. The algorithm uses an optimization routine to compute the reinforcement configuration whose corresponding magnetic distortion most resembles the measured distortions.

Finite-element analyses were conducted to simulate the interaction between steel bars and an imposed magnetic field. These analyses computed the magnetic field generated by the coil and the total magnetic field caused by the coil and the steel reinforcement.

Using the results of the finite-element analyses as input to the optimization algorithm, the proposed detection algorithm accurately determined the location and size of a single bar. The algorithm's ability to identify a single bar was not highly sensitive to errors induced in the measurements of magnetic distortion.

The algorithm was also able to identify two bars spaced horizontally or vertically. However, if one bar was much closer to the receivers than the other bar, only the closest bar was identified accurately. When 10% error was induced in the simulated magnetic distortions, the algorithm accurately located two bars only when the bar areas were already known.

To investigate the influence of the concrete's magnetic properties on the measured magnetic distortion, the magnetic susceptibilities of various concrete mixtures were measured. The concrete mixtures used two coarse aggregate types, two coarse aggregate contents, and two fly ash contents to provide a broad range of magnetic susceptibility values for concrete. Finite-element analyses were performed to simulate measurements of magnetic distortion in the presence of concretes with a range of magnetic susceptibility values greater than the range observed experimentally. These simulated measurements of magnetic distortion in the presence of concrete demonstrated that a concrete with a high

magnetic susceptibility can produce magnetic distortions comparable to the distortions caused by a steel bar.

A method of compensating for the distortion caused by the concrete was identified as being computationally inexpensive, effective, and practical. This method applied magnetostatic relationships between magnetization of volume elements in the concrete and magnetic distortion at the receivers to estimate the distortion caused by the concrete. The compensation method neglected interaction of magnetization and magnetic field between volume elements in the concrete.

Discussion of the Magnetic Algorithm

The two-dimensional magnetic algorithm is similar to the three-dimensional algorithm presented by Pla, Eberhard, and Eberhard (1994). Both rely on fundamental magnetostatic relationships that describe the interaction between steel reinforcement and an imposed magnetic field.

In the previous algorithm, a three-dimensional space was discretized into small volume elements, and the unknowns were the volumes of steel in the volume elements. This discretization approach is attractive because the steel in each volume element can be determined by solving a set of linear equations. No iteration is required. A disadvantage of this approach is that it is necessary to measure the magnetic field at a number of locations at least equal to the number of volume elements. Many measurements would be required to obtain reasonable resolution in three dimensions.

An important advantage of the new algorithm is the great reduction in the number of measurements it requires. In the new formulation, only two components of **B** must be measured, and the number of unknowns is equal to three times the number of bars. The disadvantage of the new algorithm is the potential increase in computational effort.

Whereas the previous formulation made it necessary to solve a set of linear equations, the problem has been recast as an optimization problem. Nevertheless, the problem can be implemented on a personal computer.

Another consideration is the difference in error sensitivity between the algorithms. Errors in the finite-element simulation greatly affected the results of the three-dimensional reconstruction (Pla et al 1994). The proposed two-dimensional algorithm is much less sensitive to errors. This decreased sensitivity results from the fact that the distortion caused by a unit volume of steel is small compared with the distortion caused by a unit area of steel that extends to infinity in the third dimension.

The two-dimensional magnetic algorithm also has the ability to compensate for the magnetic properties of the concrete. This compensation would probably not be possible with Pla, Eberhard, and Eberhard's (1994) algorithm because the steel causes such small distortions in the magnetic field.

Limitations of the Magnetic Algorithm

Although the algorithm is able to determine the sizes and locations of multiple bars simultaneously in simulated problems, this ability is not expected to extend to an indefinite number of bars. Some limit on the configuration complexity that the algorithm will be able to decipher was indicated by the decreased stability when solving two-bar problems. Using measurements from additional receivers can provide a larger system of equations to aid in the identification of additional bar properties. However, because of limitations on receiver locations, vectors between the various receiver and bar locations will be nearly parallel. Consequently, the information provided by additional receivers will be largely redundant.

Practical aspects of reinforced concrete construction may limit the complexity of problems that will be addressed by the algorithm. Limitations on bar spacings and maximum reinforcement ratios ensure that large numbers of bars are not located in small areas that would be evaluated by the method. Because of the algorithm's limitations, nondestructive evaluation of severely complex configurations of reinforcing steel would still require more expensive methods.

Dynamic Response Algorithm

A dynamic response algorithm has been developed to estimate the engineering properties for geometrically complex systems by comparing experimental and simulated responses to a surface impact. To implement the dynamic response algorithm, a structure is excited with a surface impact and the response of the structure is recorded with multiple receivers. The algorithm estimates the engineering properties of the system being evaluated by producing a simulation model with the most similar dynamic response.

For preliminary assessment of the algorithm, a geometry representing a layered pavement system was studied. A finite-difference formulation was used to simulate the dynamic response of the layered system. The finite-difference model was used to conduct a parametric study to determine the influences of input variables in the model. Stiffness and thickness of the top layer were found to have the greatest influences on response histories recorded at the surface.

The parametric study also investigated the influence of crack depth and location on the response of the pavement system. Cracks were found to have the greatest effect on receivers located across the crack from the impact.

Responses of a concrete slab to an impact were recorded experimentally. Application of the dynamic response algorithm to the experimental results demonstrated

the algorithm's ability to identify the stiffness and thickness of the slab. The algorithm also identified realistic values of Poisson's ratio. Applying the algorithm to experimental responses also showed that receivers farthest from the impact provide the most accurate results. This phenomena occurs because errors in impact location are a smaller percentage of the distance from the impact to the receiver for the far receivers than the near receivers.

The dynamic response algorithm was also applied to a simulated response of a slab with a partial depth, open, surface crack. This application demonstrated that the algorithm may have the potential to estimate crack depth and location.

Discussion of the Dynamic Response Algorithm

The dynamic response algorithm uses information similar to that used in impact-echo testing and SASW testing. However, the algorithm is based on a less restrictive, more computationally intense, inverse problem that provides the algorithm with the potential to investigate geometries more complex than either impact-echo or SASW can interpret.

The dynamic response algorithm provides an improvement over impact-echo testing because both depth and stiffness of the concrete may be determined from a single test. Additionally, the dynamic response algorithm offers the potential to investigate geometric complexities, such as cracks.

The dynamic response algorithm also has the potential to investigate geometries more complex than SASW is able to interpret. In particular, obtaining Young's modulus for a concrete member does not depend on assuming that the member extends to infinity normal to the impact. Also, the dynamic response algorithm appears to be sensitive to horizontal changes in the member, such as crack location.

Limitations of the Dynamic Response Algorithm

The dynamic response algorithm is also expected to encounter limitations as the number of minimization variables is increased. In particular, identification of both stiffness and thickness for multiple layers is expected to be difficult because variations in these variables produce similar changes in dynamic response.

The strength of the algorithm lies in its ability to evaluate geometric features, such as cracks, in combination with depth and stiffness of a slab. This is because discontinuities influence dynamic response much differently than slab depth and stiffness.

RECOMMENDATIONS FOR FURTHER RESEARCH

Both algorithms possess the ability to improve nondestructive evaluation of concrete structures. The following research is recommended for continuing the development and improvement of the algorithms.

Two-Dimensional Magnetic Algorithm

Development of the two-dimensional magnetic algorithm should continue. The next step in the development of this algorithm is to develop experimental instrumentation, so that magnetic distortions caused by concrete and reinforcing steel can be measured in the field or in the laboratory. The ability to conduct experimental work would allow verification of the algorithm's potential. Effects of using a dynamic driving field, $\mathbf{B}_o$, should be investigated after test equipment is available.

Dynamic Response Algorithm

The success of the dynamic response algorithm in this study provides incentive to continue development of this algorithm. Several issues are important in adapting the algorithm for general use. The issues requiring further research include:

1) Development of a three-dimensional finite-difference model to simulate the response of the structural member. The current axisymmetric model is probably only appropriate for slabs. Because most concrete members are rectangular shaped and have finite dimensions, the three-dimensional representation appears to be the logical basis for the model. Using a three-dimensional model will be even more computationally demanding than using the axisymmetric model.

2) Experimental control measures need to be developed to ensure the minimization of errors in impact location. The presence of such errors had detrimental effects on the results for the receiver nearest the impact in this study. An automated impact device would reduce this type of error.

3) Alternative test equipment should also be explored. Duration of impact is expected to have a significant effect on the response of concrete structures. Therefore, experimental results should be provided for a wide range of impact durations. Various accelerometers and displacement transducers should also be studied to determine their influence on the results.

4) Experimental work needs to be conducted to verify the algorithm's ability to identify the depth and location of a crack. This research should be conducted using the three-dimensional finite-difference model so that the length of the crack can be modeled as linear instead of circular.

5) The algorithm should also be applied to experimental results for other geometric complexities, such as voids in the concrete and cracks on the opposite face of the member.

6) Minimizing the differences between variables other than the time domain responses should be investigated. Two variables that could be used in the implementation of the algorithm are the transfer functions of the receiver responses with respect to the impact and the dispersion curve used in SASW testing. Either of these variables would facilitate filtering of unwanted frequencies from the analysis.

7) Attempts should be made to identify the cause of the large peaks occurring late in the responses of the receivers. It may be possible to simulate these peaks with a more sophisticated model.

8) Finally, it may be possible to correlate the viscous damping parameter, η, with other measures of damping such as the modal damping ratio, ζ, or quality factor, Q (ASTM C 215). A comparison of these variables should be possible by simulating the fundamental transverse frequency test with the three-dimensional model.

REFERENCES

Alterman, Z. and Karal, F. C., Jr., (1968). "Propagation of Elastic Waves in Layered Media by Finite Difference Methods," *Bulletin of the Seismological Society of America*, Vol. 58, No. 1, p. 367.

Alterman, Z. S. and Lowenthal, D., (1970). "Seismic Waves in a Quarter and Three-Quarter Plane," *The Geophysical Journal of the Royal Astronomical Society*, Vol. 20, p. 101.

"ANSYS User's Manual." (1992). Swanson Analysis Systems, Houston, PA.

Bleaney, B. I. and Bleaney, B., (1965). *Electricity and Magnetism*. Oxford University Press, London.

Bolt, Bruce A, (1976). *Nuclear Explosions and Earthquakes: The Parted Veil*, W. H. Freeman and Company, San Francisco.

Boresi, A. B., and Chong, K. P. (1987). *Elasticity in Engineering Mechanics*, Elsevier, New York.

"Building Code Requirements for Reinforced Concrete." (1995). ACI 318-95, American Concrete Institute, Detroit.

Carino, N. J., Sansalone, M., and Hsu, N. N., (1986). "Flaw Detection in Concrete by Frequency Spectrum Analysis of Impact-Echo Waveforms," *International Advances in Nondestructive Testing*, 12th ed., McGonnagle, W. J., Ed., Gordon and Breach, New York, p. 117.

Clemena, G. G., (1991). "Short-Pulse Radar Methods," Ch. 11 in *Handbook on Nondestructive Testing of Concrete*, Editors: Malhotra, V. M. and Carino, N. J., CRC Press.

"CRC Handbook of Chemistry and Physics." (1992). CRC Press, Boca Raton. 73rd. ed.

"Design and Control of Concrete Mixtures." (1990). Portland Cement Association, 13th. ed., Skokie.

Grace, A., (1990). "Optimization Toolbox: For use with MATLAB." The MathWorks, Inc., Natick, MA.

Haskell, N. A., (1953). "The Dispersion of Surface Waves in Multilayered Media," *Bulletin of the Seismological Society of America*, Vol. 43, No. 1, p.17.

HILTI, Corp., (1994). *Ferroscan*. HILTI, Inc., Tulsa.

Imran, I., Nazarian, S., and Picornell, M., (1995). "Crack Detection Using Time-Domain Wave Propagation Technique," *Journal of Geotechnical Engineering*, Vol. 121, No. 2, p. 198.

Kalinski, M. E., Stokoe, K. H., Jirsa, J. O., and Roesset, J. M., (1994). "Nondestructive Identification of Internally Damaged Areas of a Concrete Beam Using the Spectral Analysis of Surface Waves Method," *Transportation Research Record*, 1458, p. 14.

Kelly, K. R., Ward, R. W., Treitel, S., and Alford, R. M., (1976). "Synthetic Seismograms: A Finite Difference Approach," *Geophysics*, Vol. 41, No. 1, p. 2.

Lamb, H., (1904). "On the Propagation of Tremors Over the Surface of an Elastic Solid," *Philosophical Transactions of the Royal Society of London*, Vol. A203, p. 1.

Lauer, K. R., (1991). "Magnetic/Electrical Methods," Ch. 9 in *Handbook on Nondestructive Testing of Concrete*, Editors: Malhotra, V. M. and Carino, N. J., CRC Press.

Levenberg, K., (1944). "A Method for the Solution of Certain Problems in Least Squares," *Quart. Appl. Math.*, Vol. 2, p. 164.

Lin, J., and Sansalone, M., (1993). "The Transverse Elastic Impact Response of Thick Hollow Cylinders," *Journal of Nondestructive Evaluation*, Vol. 12, No. 2, p. 139.

Lin, J., and Sansalone, M., (1995). "A Procedure for Determining P-Wave Speed in Concrete for Use in Impact-Echo Testing Using a Direct P-Wave Speed Measurement Technique," submitted to *American Concrete Institute Materials Journal.*

Lin, Y., and Sansalone, M., (1992). "Transient Response of Thick Circular and Square Bars Subjected to Transverse Elastic Impact," *Journal of the Acoustical Society of America*, Vol. 91, No. 2, p. 885.

Lin, Y., and Sansalone, M., (1992a). "Transient Response of Thick Rectangular Bars Subjected to Transverse Elastic Impact," *Journal of the Acoustical Society of America*, Vol. 91, No. 5, p. 2674.

Love, A. E. H., (1911). *Some Problems of Geodynamics.* Cambridge University Press, London.

Malhotra, V. M. and Carino, N. J., (1991). *CRC Handbook on Nondestructive Testing of Concrete*, CRC Press, Boca Raton.

Malvern, L. E., (1969). *Introduction to the Mechanics of a Continuous Media*, Prentice Hall, Englewood Cliffs.

Marquardt, D., (1963). "An Algorithm for Least-squares Estimation of Nonlinear Parameters," *SIAM J. Appl. Math.*, Vol. 11, p. 431.

"Maxwell 2D Field Simulator Users Guide." (1991). Ansoft Corporation, Pittsburgh.

Mindess, S., and Young, J. F., (1981). *Concrete*, Prentice-Hall Inc., Englewood Cliffs.

Mitchell, T. M., (1991). "Radioactive/Nuclear Methods," Ch. 10 in *Handbook on Nondestructive Testing of Concrete*, Editors: Malhotra, V. M. and Carino, N. J., CRC Press.

More, J. J., (1977). "The Levenberg-Marquardt Algorithm: Implementation and Theory," *Numerical Analysis*, ed. G. A. Watson, Lecture Notes in Mathematics 630, Springer-Varleg, p. 105.

Nayfeh, M. H. and Brussel, M. K., (1985). *Electricity and Magnetism*. Wiley, New York.

Nazarian, S., (1984). *In Situ Determination of Elastic Moduli of Soil Deposits and Pavement Systems by Spectral-Analysis-of-Surface-Waves Method*. The University of Texas at Austin, Ph. D. Dissertation.

Nazarian, S., Stokoe, K. H., II, and Hudson, W. R., (1983). "Use of Spectral-Analsysis-of-Surface-Waves Method for Determination of Moduli and Thickness of Pavement Systems," *Transportation Research Record*, 930, p. 38.

Nelder, J. A. and Mead R., (1964). "A Simplex Method for Function Minimization," *Computer Journal*, Vol. 7, p. 308.

Nogueira, A. C., (1986). Effect of Cavities on the Propagation of Surface Waves. The University of Texas, M. S. Thesis.

Pla, G., Eberhard, M. and Eberhard P., (1994). "Magnetic Imaging of Reinforcing Steel," *Journal of Nondestructive Evaluation*, Vol. 13, No. 1, p. 23.

Popovics, S., and Popovics, J. S., (1991). "Improved Determination of the Locations and Sizes of Steel Rebars in Concrete," Proceedings ACI International Conference: Evaluation and Rehabilitation of Concrete Structures and Innovations in Design, Ed. V. M. Malhotra, Hong Kong, SP-128, Vol. 1, p. 485.

Rayleigh, L., (1887). "On Waves Propagated along the Plane Surface of an Elastic Solid," Proceedings, London Mathematical Society, Vol. 17, p. 4.

Richart, F.E., Jr., Hall, J.R., Jr., and Woods, R.D., (1970). *Vibrations of Soils and Foundations*, Prentice Hall, Inc., Englewood Cliffs, New Jersey, p. 414.

Sansalone, M., and Carino, N. J., (1987). "Transient Impact Response of Thick Circular Plates," *Journal of Research for the National Bureau of Standards*, Vol. 92, No. 6, p. 369.

Sansalone, M., and Carino, N. J., (1988). "Impact-Echo Method: Detecting Honeycombing, the Depth of Surface Opening Cracks, and Ungrouted Ducts," *Concrete International*, Vol. 10, No. 4, p. 38.

Sansalone, M., and Carino, N. J., (1989). "Laboratory and Field Study of the Impact-Echo Method for Flaw Detection in Concrete," *Nondestructive Testing of Concrete*, Lew, H. S., Ed., SP-112, American Concrete Institute, p. 1.

Sansalone, M., and Carino, N. J., (1989a). "Detecting Delaminations in Concrete Slabs with and without Overlays Using the Impact-Echo Method," *American Concrete Institute Materials Journal*, Vol. 86, No. 2, p. 175.

Sansalone, M. and Carino, N. J., (1991). "Stress Wave Propagation Methods," Ch. 12 in *Handbook on Nondestructive Testing of Concrete*, Editors: Malhotra, V. M. and Carino, N. J., CRC Press.

Sigmon, K., (1992). "MATLAB Primer." Department of Mathematics, University of Florida, 2nd ed.

Weil, G. J., (1991). "Infrared Thermographic Techniques," Ch. 13 in *Handbook on Nondestructive Testing of Concrete*, Editors: Malhotra, V. M. and Carino, N. J., CRC Press.

Appendix A

DISCRETIZED FORM OF THE EQUATIONS OF MOTION

Equations to calculate displacements u and v for the l+1 time step were obtained by discretizing Equations 7.13 and 7.14. The equations were discretized by approximating the partial derivatives with finite-differences. Two sided differences were used to estimate the time derivatives on the left hand side of Equations 7.13 and 7.14. However, one sided differences were used to represent the time derivatives on the right hand side of the equations because displacements at time step l+1 were not known for all of the grid points. Two sided differences were used to estimate all of the spatial derivatives.

Discretizing Equation 7.13 and solving for u at time step l+1 for a grid point located $m\Delta x$ in the horizontal direction and $n\Delta y$ in the vertical direction, one obtains:

$$
\begin{aligned}
&u(m,n,l+1) = 2u(m,n,l) - u(m,n,l-1) \\
&+\frac{(\lambda+2G)(\Delta t)^2}{\rho(\Delta r)^2}\left[u(m+1,n,l) - 2u(m,n,l) + u(m-1,n,l)\right] \\
&+\frac{(\lambda+2G)(\Delta t)^2}{2\rho r\Delta r}\left[u(m+1,n,l) - u(m-1,n,l)\right] - \frac{2G(\Delta t)^2}{\rho r^2}\left[u(m,n,l)\right] \\
&+\frac{G(\Delta t)^2}{\rho(\Delta z)^2}\left[u(m,n+1,l) - 2u(m,n,l) + u(m,n-1,l)\right] \\
&+\frac{(\lambda+G)(\Delta t)^2}{4\rho\Delta r\Delta z}\left[w(m+1,n+1,l) - w(m+1,n-1,l)\right] \\
&-\frac{(\lambda+G)(\Delta t)^2}{4\rho\Delta r\Delta z}\left[w(m-1,n+1,l) - w(m-1,n-1,l)\right] \\
&+\frac{4\eta\Delta t}{3\rho(\Delta r)^2}\left[u(m+1,n,l) - 2u(m,n,l) + u(m-1,n,l)\right] \\
&-\frac{4\eta\Delta t}{3\rho(\Delta r)^2}\left[u(m+1,n,l-1) - 2u(m,n,l-1) + u(m-1,n,l-1)\right] \\
&+\frac{2\eta\Delta t}{3\rho r\Delta r}\left[u(m+1,n,l) - u(m-1,n,l) - u(m+1,n,l-1) + u(m-1,n,l-1)\right] \\
&+\frac{\eta\Delta t}{12\rho\Delta r\Delta z}\left[w(m+1,n+1,l) - w(m+1,n-1,l) - w(m-1,n+1,l) + w(m-1,n-1,l)\right] \\
&-\frac{\eta\Delta t}{12\rho\Delta r\Delta z}\left[w(m+1,n+1,l-1) - w(m+1,n-1,l-1)\right] \\
&+\frac{\eta\Delta t}{12\rho\Delta r\Delta z}\left[w(m-1,n+1,l-1) - w(m-1,n-1,l-1)\right] \\
&+\frac{\eta\Delta t}{\rho(\Delta z)^2}\left[u(m,n+1,l) - 2u(m,n,l) + u(m,n-1,l)\right] \\
&-\frac{\eta\Delta t}{\rho(\Delta z)^2}\left[u(m,n+1,l-1) - 2u(m,n,l-1) + u(m,n-1,l-1)\right] \\
&+\frac{2\eta\Delta t}{\rho r^2}\left[u(m,n,l) - u(m,n,l-1)\right]
\end{aligned}
\tag{A.1}
$$

Similarly, discretizing Equation 7.14 and solving for v at the same grid point yields the following relationship:

$$
\begin{aligned}
&w(m,n,l+1) = 2w(m,n,l) - w(m,n,l-1) \\
&+\frac{(\lambda+2G)(\Delta t)^2}{\rho(\Delta z)^2}\left[w(m,n+1,l) - 2w(m,n,l) + w(m,n-1,l)\right] \\
&+\frac{(\lambda+G)(\Delta t)^2}{4\rho\Delta r\Delta z}\left[u(m+1,n+1,l) - u(m+1,n-1,l)\right] \\
&-\frac{(\lambda+G)(\Delta t)^2}{4\rho\Delta r\Delta z}\left[u(m-1,n+1,l) - u(m-1,n-1,l)\right] \\
&+\frac{G(\Delta t)^2}{\rho(\Delta r)^2}\left[w(m+1,n,l) - 2w(m,n,l) + w(m-1,n,l)\right] \\
&+\frac{(\lambda+G)(\Delta t)^2}{2\rho r\Delta z}\left[u(m,n+1,l) - u(m,n-1,l)\right] + \frac{G(\Delta t)^2}{2\rho r\Delta r}\left[w(m+1,n,l) - w(m-1,n,l)\right] \\
&+\frac{4\eta\Delta t}{3\rho(\Delta z)^2}\left[w(m,n+1,l) - 2w(m,n,l) + w(m,n-1,l)\right] \\
&-\frac{4\eta\Delta t}{3\rho(\Delta z)^2}\left[w(m,n+1,l-1) - 2w(m,n,l-1) + w(m,n-1,l-1)\right] \\
&+\frac{\eta\Delta t}{12\rho\Delta r\Delta z}\left[u(m+1,n+1,l) - u(m+1,n-1,l) - u(m-1,n+1,l) + u(m-1,n-1,l)\right] \\
&-\frac{\eta\Delta t}{12\rho\Delta r\Delta z}\left[u(m+1,n+1,l-1) - u(m+1,n-1,l-1)\right] \\
&+\frac{\eta\Delta t}{12\rho\Delta r\Delta z}\left[u(m-1,n+1,l-1) - u(m-1,n-1,l-1)\right] \\
&+\frac{\eta\Delta t}{6\rho r\Delta z}\left[u(m,n+1,l) - u(m,n-1,l) - u(m,n+1,l-1) + u(m,n-1,l-1)\right] \\
&+\frac{\eta\Delta t}{\rho(\Delta r)^2}\left[w(m+1,n,l) - 2w(m,n,l) + w(m-1,n,l)\right] \\
&-\frac{\eta\Delta t}{\rho(\Delta r)^2}\left[w(m+1,n,l-1) - 2w(m,n,l-1) + w(m-1,n,l-1)\right] \\
&+\frac{\eta\Delta t}{2\rho r\Delta r}\left[w(m+1,n,l) - w(m-1,n,l) - w(m+1,n,l-1) + w(m-1,n,l-1)\right]
\end{aligned}
\tag{A.2}
$$

Appendix B

MINIMIZATION RESULTS FROM THE DYNAMIC RESPONSE ALGORITHM

Table B.1. Summary of reconstruction results.

Variables Included In Minimization	Receivers Used In Minimization				
	1	2	3	1,2,3	2,3
E	27.2 GPa	45.0 GPa	42.2 GPa	38.5 GPa	41.2 GPa
d	309 mm	296 mm	199 mm	242 mm	217 mm
E	37.0 GPa	43.7 GPa	42.7 GPa	38.7 GPa	41.1 GPa
d	314 mm	289 mm	194 mm	244 mm	221 mm
η/G	3.52×10^{-6} s	9.75×10^{-7} s	3.98×10^{-6} s	2.05×10^{-6} s	1.13×10^{-6} s
E	28.8 GPa	44.9 GPa	42.9 GPa	37.3 GPa	39.5 GPa
d	308 mm	289 mm	203 mm	251 mm	228 mm
ν	0.250	0.145	0.234	0.174	0.175
E	28.4 GPa	37.1 GPa	47.8 GPa	32.5 GPa	47.8 GPa
d	304 mm	303 mm	197 mm	259 mm	211 mm
ρ	2440 kg/m^3	1860 kg/m^3	2590 kg/m^3	2030 kg/m^3	2640 kg/m^3
E	26.9 GPa	43.3 GPa	30.8 GPa	43.8 GPa	39.7 GPa
d	311 mm	269 mm	214 mm	221 mm	229 mm
η/G	3.57×10^{-6} s	7.87×10^{-7} s	6.09×10^{-6} s	1.51×10^{-6} s	2.24×10^{-6} s
ν	0.190	0.282	-0.280	0.290	0.182
E	25.4 GPa	38.8 GPa	38.6 GPa	33.0 GPa	50.9 GPa
d	304 mm	294 mm	195 mm	259 mm	211 mm
η/G	3.05×10^{-6} s	1.16×10^{-6} s	5.07×10^{-6} s	1.79×10^{-6} s	8.54×10^{-7} s
ρ	2080 kg/m^3	2000 kg/m^3	2120 kg/m^3	2060 kg/m^3	2820 kg/m^3
E	30.4 GPa	38.1 GPa	32.9 GPa	33.7 GPa	42.9 GPa
d	317 mm	300 mm	217 mm	251 mm	215 mm
ν	0.262	0.274	0.265	0.235	0.269
ρ	2480 kg/m^3	1930 kg/m^3	1810 kg/m^3	2010 kg/m^3	2290 kg/m^3
E	26.2 GPa	40.0 GPa	16.7 GPa	34.2 GPa	45.8 GPa
d	314 mm	301 mm	276 mm	251 mm	215 mm
η/G	3.66×10^{-6} s	8.08×10^{-7} s	2.47×10^{-6} s	1.66×10^{-6} s	8.61×10^{-7} s
ν	0.221	0.284	0.221	0.243	0.269
ρ	2160 kg/m^3	2020 kg/m^3	1170 kg/m^3	2030 kg/m^3	2430 kg/m^3

VITA

Mr. Craig Newtson received a B.S. in Civil Engineering from the University of Wyoming (1989), a M.S. in Civil Engineering (Structural) from the University of Wyoming (1992), and a Ph.D. in Civil Engineering (Structural) from the University of Washington (1997). Mr. Newtson is registered as an Engineer in Training in the state of Wyoming and is a member of the American Society of Civil Engineers (ASCE).

At the University of Wyoming, Mr. Newtson studied the influence of aggregate top size on the mixture design, resilient modulus, and resistance to permanent deformation of bituminous concrete. Results from this research were published in a paper appearing in the ASCE *Journal of Materials in Civil Engineering* (1993) and a paper appearing in the American Society for Testing and Materials *Journal of Testing and Evaluation* (1993).

At the University of Washington, Mr. Newtson conducted research on the effects of latex-modifier content and type in Portland cement concrete on the resistance to damage due to freezing and thawing. Results from this research were presented at the Fourth CANMET/ACI International Conference on Superplasticizers and Other Chemical Admixtures (1994).

Mr. Newtson's research for the Ph.D. degree at the University of Washington included the development of a reconstruction algorithm to determine the locations and sizes of reinforcing bars in concrete and a reconstruction algorithm to determine the geometry and material properties of a concrete member. Portions of this research were published in the ASCE *Journal of Materials in Civil Engineering* (1995) and at the Third Conference on Nondestructive Evaluation of Civil Structures and Materials (1996).